Growth of lattice-matched hybrid semiconductor-ferromagnetic trilayers using solid-phase epitaxy

Towards a spin-selective Schottky barrier tunnel transistor

D I S S E R T A T I O N

zur Erlangung des akademischen Grades

d o c t o r r e r u m n a t u r a l i u m
(Dr. rer. nat.)
im Fach Physik
eingereicht an der
Mathematisch-Naturwissenschaftlichen Fakultät
Humboldt-Universität zu Berlin

von
M.Sc. Samuel Gaucher

Präsidentin der Humboldt-Universität zu Berlin:
Prof. Dr.-Ing. Dr. Sabine Kunst

Dekan der Mathematisch-Naturwissenschaftlichen Fakultät:
Prof. Dr. Elmar Kulke

Gutachter:
(i) Prof. Dr. Henning Riechert
(ii) Prof. Dr. Saskia F. Fischer
(iii) Dr. Matthieu Jamet

Tag der mündlichen Prüfung: 10.03.2021

'I call our world Flatland, not because we call it so, but to make its nature clearer to you, my happy readers, who are privileged to live in Space.'

Edwin A. Abbott
Flatland: A Romance of Many Dimensions

'Yes. In the end, it's only a trick.'

Jep Gambardella
La Grande Bellezza

Abstract

The search for technologies beyond the CMOS scaling limits has accelerated developments in the field of spintronics, whose central idea is to use the electronic spin degree of freedom to encode and manipulate information. With this goal in mind, this thesis presents our attempt to grow the structures necessary to fabricate a Spin-Selective Schottky Barrier Tunnel transistor (SS-SBTT). Such a transistor would offer the possibility to modulate spin-polarized currents, hence providing the industry with a component on which new computing paradigms could be built. The device, which is a hybrid between a Schottky transistor and a magnetic tunnel junction (MTJ), relies on charge carriers being transported through a thin semiconducting (SC) layer separating two ferromagnetic (FM) contacts. Realizing this feature is experimentally tedious, since it requires to obtain high quality and lattice-matched FM/SC/FM vertical trilayers. The growth of a SC over a metallic substrate is complicated by incompatible crystallization energies, i.e. SCs grow at temperatures too high to preserve the integrity of the FM interface, which is critical to preserve high spin injection efficiency.

To solve this problem, we developed a solid-phase epitaxy (SPE) approach, whereby a thin amorphous layer of Ge (4-15 nm) is crystallized by annealing over Heusler alloy Fe_3Si on GaAs(001) substrates. We found that slow annealing rates (5°C/min) in a temperature range between the crystallization temperature of Fe_3Si (200°C) and Ge (300°C) could produce a lattice-matched Ge-rich compound, over which a second Fe_3Si could then be grown my molecular-beam epitaxy (MBE). The approach was extended to trilayer stacks with different thicknesses and involving both Fe_3Si and Co_2FeSi. Surprisingly, the Ge-rich compound obtained by annealing Ge over Fe_3Si is a new layered polymorph of $FeGe_2$. SQUID magnetometry measurements performed on various trilayer stacks indicate that the $FeGe_2$ layers obtained by SPE can effectively decouple the two FM films, and place the samples in states of antiparallel magnetization, as expected in conventional MTJs. Vertical spin valve devices created using $Fe_3Si/FeGe_2/Fe_3Si$ and $Fe_3Si/FeGe_2/Co_2FeSi$ trilayers with thickness of 36/4-8/12 nm were used to demonstrate that charge transport is spin-selective across the heterojunctions, albeit showing a magnetoresistance (MR) percentage of at most 0.30% at room temperature. The MR decreases with temperature in these devices, which correlates with a ferromagnetic transition taking place in the $FeGe_2$ buffer layer.

The structure and electrical properties of the new $FeGe_2$ polymorph were also investigated. TEM coupled with XRD experiments and simulations were used to determine that the compound has space group *P4mm*, which still contains up to 17% Si atoms substituting Ge sites. An isolation of the $FeGe_2$ films from the underlying Fe_3Si was realized by tuning the proportion Fe, Si and Ge atoms required to obtain the right stoichiometry once all films are annealed and intermixed. Hall bars fabricated on $FeGe_2$ thin films displayed increasing resistivity at low temperature, following a curve typically observed in extrinsic semiconductors. Overall, the growth and transport experiments performed in this thesis confirmed that the SPE approach can successfully produce the vertical trilayer stacks required for the eventual fabrication of a SS-SBTT.

Keywords: Spintronics, Heusler alloys, molecular beam epitaxy, solid-phase epitaxy, magnetic tunnel junction, Schottky transistor, magnetic semiconductors, Fe_3Si, Co_2FeSi, $FeGe_2$.

Zusammenfassung

Die Suche nach Technologien jenseits der CMOS-Skalierungsgrenzen hat die Entwicklungen auf dem Gebiet der Spintronik beschleunigt, deren zentrale Idee darin besteht, den Freiheitsgrad des elektronischen Spins zur Kodierung und Manipulation von Informationen zu nutzen. Mit diesem Ziel vor Augen stellt diese Arbeit unseren Versuch vor, die zur Herstellung eines Spin-selektiven Schottky-Barriere-Tunnel-Transistors (SS-SBTT) notwendigen Strukturen wachsen zu lassen. Ein solcher Transistor würde die Möglichkeit bieten, spinpolarisierte Ströme zu modulieren und damit der Industrie ein Bauelement zur Verfügung stellen, auf dem neue Rechenparadigmen aufgebaut werden könnten. Das Bauelement, bei dem es sich um einen Hybrid zwischen einem Schottky-Transistor und einem magnetischen Tunnelübergang (MTJ) handelt, beruht darauf, dass Ladungsträger durch eine dünne halbleitende (SC) Schicht transportiert werden, die zwei ferromagnetische (FM) Kontakte trennt. Die Realisierung dieses Merkmals ist experimentell langwierig, da sie qualitativ hochwertige und gitterangepasste vertikale FM/SC/FM-Trilayer erfordert. Das Wachstum eines SC über einem metallischen Substrat wird durch inkompatible Kristallisationsenergien erschwert, d.h. SCs wachsen bei Temperaturen, die zu hoch sind, um die Integrität der FM-Grenzfläche zu erhalten, was für die Erhaltung einer hohen Spininjektionseffizienz entscheidend ist.

Um dieses Problem zu lösen, haben wir einen Ansatz der Festphasenepitaxie (SPE) entwickelt, bei dem eine dünne amorphe Schicht aus Ge (4-15 nm) durch Glühen über Heusler-Legierung Fe_3Si auf GaAs(001)-Substraten kristallisiert wird. Wir fanden heraus, dass langsame Glühgeschwindigkeiten (5°C/min) in einem Temperaturbereich zwischen der Kristallisationstemperatur von Fe_3Si (200°C) und Ge (300°C) eine gitterangepasste Ge-reiche Verbindung erzeugen können, über die dann ein zweites Fe_3Si in meiner Molekularstrahlepitaxie (MBE) gezüchtet werden kann. Der Ansatz wurde auf Dreischichtstapel mit unterschiedlichen Dicken ausgeweitet, die sowohl Fe_3Si als auch Co_2FeSi enthielten. Überraschenderweise ist die Ge-reiche Verbindung, die durch Glühen von Ge über Fe_3Si erhalten wurde, ein neues Schichtpolymorph von $FeGe_2$. SQUID-Magnetometriemessungen, die an verschiedenen Dreischichtstapeln durchgeführt wurden, weisen darauf hin, dass die durch SPE erhaltenen $FeGe_2$-Schichten die beiden FM-Filme effektiv entkoppeln und die Proben in Zustände antiparalleler Magnetisierung versetzen können, wie bei herkömmlichen MTJs erwartet. Vertikale Spinventilvorrichtungen, die mit $Fe_3Si/FeGe_2/Fe_3Si$ und $Fe_3Si/FeGe_2/Co_2FeSi$-Dreischichten mit einer Dicke von 36/4-8/12 nm hergestellt wurden, wurden verwendet, um zu demonstrieren, dass der Ladungstransport über die Heteroübergänge spin-selektiv ist, obwohl sie bei Raumtemperatur einen Magnetwiderstands-(MR-)Prozentsatz von höchstens 0,30% aufweisen. Der MR nimmt in diesen Bauelementen mit der Temperatur ab, was mit einem ferromagnetischen Übergang korreliert, der in der $FeGe_2$-Pufferschicht stattfindet.

Die Struktur und die elektrischen Eigenschaften des neuen $FeGe_2$-Polymorphs wurden ebenfalls untersucht. TEM gekoppelt mit XRD-Experimenten und Simulationen wurden verwendet, um festzustellen, dass die Verbindung die Raumgruppe P4mm aufweist, die noch bis zu 17% Si-Atome enthält, die Ge-Stellen ersetzen. Eine Isolierung der $FeGe_2$-Filme von dem darunter liegenden Fe_3Si wurde durch Abstimmung des Verhältnisses zwischen

Fe, Si und Ge-Atomen erreicht, das erforderlich ist, um die richtige Stöchiometrie zu erhalten, nachdem alle Filme geglüht und vermischt wurden. Auf $FeGe_2$-Dünnschichten hergestellte Hallstäbe zeigten bei niedriger Temperatur einen zunehmenden spezifischen Widerstand, der einer Kurve folgte, die typischerweise bei extrinsischen Halbleitern beobachtet wird. Insgesamt bestätigten die in dieser Arbeit durchgeführten Wachstums- und Transportexperimente, dass der SPE-Ansatz erfolgreich die vertikalen Dreischichtstapel herstellen kann, die für die spätere Herstellung eines SS-SBTT erforderlich sind.

Stichwörter: Spintronik, Heusler-Legierungen, Molekularstrahlepitaxie, Festphasen-Epitaxie, magnetischer Tunnelübergang, Schottky-Transistor, magnetische Halbleiter, Fe_3Si, Co_2FeSi, $FeGe_2$.

List of publications

Authored publications featuring parts of this work

S. Gaucher, B. Jenichen, and J. Herfort, *Ferromagnet/semiconductor/ferromagnet hybrid trilayers grown using solid-phase epitaxy*, Semicond. Sci. Technol. **33** 104005 (2018)

S. Gaucher, B. Jenichen, J. Kalt, U. Jahn, A. Trampert, and J. Herfort, *Growth of $Fe_3Si/Ge/Fe_3Si$ trilayers on GaAs(001) using solid-phase epitaxy*, Appl. Phys. Lett. **110** 102103 (2017)

Further publications

M. Terker, L. Nicolai, S. Gaucher, J. Herfort, and A. Trampert, *In Situ Transmission Electron Microscopy of Disorder-Order Transition in Epitaxially Stabilized $FeGe_2$*, J. Phys. Chem. C **125**, 2779-2784 (2021)

D. Czubak, S. Gaucher, J. Herfort, K. Zollner, J. Fabian, and M. Ramsteiner, *Electronic and magnetic properties of α-$FeGe_2$ films embedded in vertical spin valve devices*, Phys. Rev. Mater. **4**, 104415 (2020)

B. Jenichen, M. Hanke, S. Gaucher, A. Trampert, J. Herfort, H. Kirmse, B. Haas, E. Willinger, X. Huang, and S. C. Erwin, *Ordered structure of $FeGe_2$ formed during solid-phase epitaxy*, Phys. Rev. Mater. **2** 051402 (2018)

Conference presentations

S. Gaucher, B. Jenichen, and J. Herfort, *Structural and electrical properties of layered $FeGe_2$ thin films* **(Poster)**, Annual meeting of the German Physical Society, Regensburg (Germany), March 2019

D. Czubak, S. Gaucher, J. Herfort, H. T. Grahn, and M. Ramsteiner, *Vertical spin valves using the novel two-dimensional material $FeGe_2$* **(Poster)**, Annual meeting of the German Physical Society, Regensburg (Germany), March 2019

List of publications

S. Gaucher, B. Jenichen, M. Hanke, A. Tampert, H. Kirmse, and J. Herfort, *Magnetotransport in $FeGe_2$ thin films* **(Poster)**, 10^{th} international School and Conference on Physics and Applications of Spin Phenomena in Solids, Linz (Austria), August 2018

S. Gaucher, B. Jenichen, U. Jahn, A. Trampert, and J. Herfort, *Ferromagnetic thin film heterostructures grown by solid-phase epitaxy* **(Talk)**, Institute Seminar at the Paul-Drude-Institut für Festkörperelektronik, Berlin (Germany), January 2018

S. Gaucher, B. Jenichen, U. Jahn, A. Trampert, and J. Herfort, *$FeGe_2$ thin films grown by solid-phase epitaxy* **(Poster)**, Annual meeting of the German Physical Society, Berlin (Germany), November 2017

S. Gaucher, B. Jenichen, U. Jahn, A. Trampert, and J. Herfort, *Magnetic properties of ferromagnet/semiconductor/ferromagnet hybrid trilayers grown by solid-phase epitaxy* **(Talk)**, Austrian MBE Workshop 2017, Vienna (Austria), September 2017

S. Gaucher, B. Jenichen, J. Kalt, U. Jahn, A. Trampert, and J. Herfort, *$Fe_3Si/Ge/Fe_3Si$ trilayers on GaAs(001)* **(Poster)**, German Physical Society Summer School on Magnetism, Bad Honnef (Germany), September 2017

List of abbreviations

AFM	atomic force microscopy
AHE	anomalous Hall effect
AMR	anisotropic magnetoresistance
EBSD	electron backscattered diffraction
FLP	Fermi level pinning
FM	ferromagnet
FWHM	full width at half maximum
HRTEM	high-resolution transmission electron microscopy
IRDS	International Roadmap for Devices and Systems
ITRS	International Technology Roadmap for Semiconductors
MBE	molecular beam epitaxy
MTJ	magnetic tunnel junction
PHE	planar Hall effect
RHEED	reflection high-energy election diffraction
SAD	selected area diffraction
SBH	Schottky barrier height
SC	semiconductor
SEM	scanning electron microscopy
SPE	solid-phase epitaxy
SQUID	superconducting quantum interference device
SS-SBTT	spin-selective Schottky barrier tunnel transistor
STEM	scanning transmission electron microscopy
TEM	transmission electron microscopy
TMR	tunnel magnetoresistance
UHV	ultra high vacuum
VEC	valence electron per formula unit
WL	weak localization
XRD	x-ray diffractometry
XRR	x-ray reflectivity

List of constants and symbols

Symbol	Description	Unit
a_{hkl}	lattice spacing of a given (hkl) plane	Å
A_G	Richardson constant ($0.5 \times 1.20173 \times 10^6$)	A/m^2K^2
e	electron charge (1.602×10^{-19})	C
E_g	band gap energy	eV
$\hbar$	reduced Planck constant (1.054×10^{-34})	Js
H_C	coercivity	Oe
I	current	A
k_B	Boltzmann constant (1.381×10^{-23})	$J\,K^{-1}$
m_0	electron rest mass (9.109×10^{-31})	kg
$m^*_{e,h}$	electron/hole effective mass	kg
M_R	magnetic remanence	emu
M_S	saturation magnetization	emu
μ_0	permeability of vacuum ($4\pi \cdot 10^{-7}$)	Vs/Am
μ_B	Bohr magneton	J/T
R	resistance	Ω
R_{rms}	root mean square roughness	nm
R_s	sheet resistance	Ω/□
ρ	resistivity	μΩ cm
σ	conductivity	S/m
t_{growth}	growth time	min
T	temperature	K
T_A	annealing temperature	K
R_A	annealing rate	K/min
V	voltage	V

Contents

1 Introduction

1.1 Moore no more

The rate at which semiconductor technology progressed in the second half of the 20th century is generally described in terms of Moore's Law. In 1965, Gordon E. Moore was asked by *Electronics Magazine* to comment on the future of the semiconductor industry. Three years before founding NM Electronics (which then became Intel), Moore already wrote with considerable enthusiasm about incoming "home computers", "automatic controls for automobiles", and "electronic wristwatches."[1] Based on his observation of trends among the latest advances in the manufacture of semiconductors, he projected that the number of electronic components on integrated circuits would double every year, at least for the next ten years. He later revised his initial prediction, in light of developments that occurred in the 1970's, this time adjusting the growth to the number of components doubling approximately every two years.[2] Moore's second forecast effectively set the pace at which the digital revolution persisted throughout the subsequent forty years[3] — before eventually slowing down in the early 2010's.

Throughout the decades-long success of the miniaturization endeavor, it was known that limitations would prevent the industry from maintaining the trend forever. The metal-oxide-semiconductor field-effect transistor (MOSFET), which is the key component of modern electronics, has shrank to dimensions that are today below 10 nanometers. Let aside the technical difficulty behind the mass fabrication of these small components, important physical limitations altering the functioning of the MOSFET arise at the nanoscale. Leakage currents become significant due to the smaller voltage thresholds being employed, and due to quantum mechanical tunneling through the transistor's gate-oxide. Joule heat coming from the higher power density is also increasingly difficult to evacuate, which can lead to hardware damage through overheating. The limits of miniaturization became manifest in the early 2010's, as seen from performance of newly released processors deviating from the curve predicted by Moore's Law.[4] The former CEO of Intel, Brian Krzanich, confirmed in 2015 that their progress had decelerated,[5] although new techniques could keep the hyper scaling of MOSFET feasible for a few more generations (further down below 10 nm).[6] Nonetheless, new technological solutions are needed to keep improving contemporary electronics beyond the CMOS scaling limits.

Fundamental research has always been active in order to improve the technologies in place, and to provide replacement solutions when possible. And as much as Schockley, Brattain and Bardeen were awarded the 1956 Nobel Prize in Physics for their discovery of the "transistor effect", paradigm-changing solutions are expected to arise from fundamental re-

search in solid-state physics. Between 1998 and 2016, the International Technology Roadmap for Semiconductors (ITRS) provided guidance to the semiconductor industry through a series of documents published by a group of semiconductor experts. But with the decline of Moore's Law, the ITRS ceased to be updated in 2017, and was replaced by the more general International Roadmap for Devices and Systems (IRDS). Within this new roadmap were defined a series of focus groups, among which one named *Beyond CMOS* is in charge of investigating and promoting alternative digital logic technologies. The *Beyond CMOS* focus group covers a wide range of topics, among which the most mature and sizeable research field is arguably spintronics.[7] Spintronics, a contraction for "spin electronics", is a field of physics which is investigating new scaling solutions by encoding and manipulating information via the electronic spin degree of freedom.

1.2 Aims of thesis

In this thesis, we report on developments towards the realization of a new useful spintronic device: the Spin-Selective Schottky Barrier Tunnel Transistor, or SS-SBTT. Alike conventional transistors, the SS-SBTT is a semiconductor device with amplifying and switching capabilities. However, its design is meant to allow preserving spin-polarized currents. The possibility to operate a transistor in which the electronic spin polarization is protected would offer a way to harness an extra degree of freedom for information processing, hence providing the industry with a technology performing beyond the limits imposed by today's miniaturization approach.

The basic principle of SS-SBTT is to achieve spin injection between two metallic ferromagnetic (FM) electrodes through a nanoscopic semiconductor (SC) tunnel barrier. The realization of this device requires overcoming several technical obstacles, primarily concerning the growth of high quality vertical FM/SC/FM heterojunctions. The methods and results presented in this thesis are primarily focused on this task, for which molecular-beam epitaxy (MBE) plays a central role. However, the heart of the problem lies in growing epitaxial semiconductors over metals while preventing intermixing at the interface, a step that is essential in order to maintain efficient tunneling across the trilayer stacks. The incompatible crystallization energies between metals and semiconductors forces us to venture outside the realm of conventional MBE growth techniques. The driving experimental aim of this thesis is to develop a new solid-phase epitaxy (SPE) approach, whereby an amorphous semiconductor is crystallized slowly by annealing over an epitaxial metallic surface, with hopes to realize atomically flat and lattice-matched FM/SC/FM heterostructures.

To guide our progress towards the implementation of a SS-SBTT, the samples created throughout this project are investigated in a number of ways. First, the structural quality of the films should be monitored in order to optimize and validate our novel SPE approach. Then, the growth experiments are accompanied by SQUID magnetometry measurements, since understanding the magnetic properties of the films and heterojunctions is crucial to assess the possibility to operate the SS-SBTT as intended. Importantly, using the FM/SC/FM

trilayers obtained, spin valve measurements should be conducted in order to demonstrate the spin selective nature of the devices fabricated and offer a convincing proof of concept for the SS-SBTT.

1.3 Outline

In Chapter 2, a theoretical and historical background is first given in order to clarify the basic principles of spintronics, followed by essential notions required to understand the operation of the SS-SBTT proposed in this thesis. The chapter then introduces Heusler alloys, a family of materials which plays an important role in this research. Some Heusler alloys, such as Fe_3Si and Co_2FeSi, feature appealing structural and magnetic properties, which make them ideal candidates for integration in semiconductor spintronics. A review of magnetism is also provided, with emphasis on anisotropic ferromagnetic single-crystalline thin films. Building on these theoretical notions, the SS-SBTT device concept is then explained in details, with arguments supporting each aspects of the design and operation. The past progress concerning the epitaxial growth of semiconductors over ferromagnetic metals for spintronics applications is then reviewed, detailing the scientific developments that led to the SPE approach.

Chapter 3 outlines the apparatus and measurement techniques used to fabricate and characterize the thin films stacks which are central to this study. The MBE cluster used to grow GaAs, Ge, Fe_3Si and Co_2FeSi is described. The main methods used to perform structural analysis and magnetization measurements are as well explained, namely X-ray diffraction (XRD), transmission electron microscopy (TEM), atomic force microscopy (AFM), and the superconducting quantum interference device (SQUID) magnetometer. The preparation of samples for magnetotransport and spin valve measurements is presented, as well as the experiments conducted using standard DC and AC (lock-in) techniques in two different cryostats.

The principal results of this research are presented in Chapter 4, starting with the optimization of the SPE parameters. The various layer stack combinations realized are presented and discussed in terms of their structural and magnetic properties. The accidental synthesis of a new polymorph of $FeGe_2$ is reported and explained, and turns out to be a necessary step to obtain the lattice-matched trilayers originally intended. Spin-valve measurements are also shown here, assessing the feasibility of the SS-SBTT device concept.

Chapter 5 is dedicated to an in-depth investigation of the structural and electrical properties of the new $FeGe_2$ compound obtained through the previously described growth experiments. A new challenge here is to isolate the material in order to perform transport and magnetization measurements without any contribution from the adjacent metallic Fe_3Si. The methods used to obtain 'pure' $FeGe_2$ thin film are presented, along with the results allowing to characterized the material as a metastable semiconducting ferromagnet.

The final chapter summarizes the main findings. Suggestions are given regarding further studies and device concepts based on the results of our investigations.

2 Theory and Historical Context

2.1 Spintronics

2.1.1 Basics

Spintronics focuses on the idea to use the electronic spin degree of freedom to encode and manipulate information. This field has roots reaching towards diverse areas of physics (optics, magnetism, semiconductor physics, superconductivity), its goal remaining to achieve active control of the quantum mechanical electronic spin in solid-state systems. In this context, spin can refer to the spin angular momentum of a single electron $\boldsymbol{S}$, with measurable magnetic moment

$$\mathbf{m} = -g_s \mu_B \frac{\mathbf{S}}{\hbar} \tag{2.1}$$

where μ_B is the Bohr magneton and g_s the electron g-factor ≈ 2, or to the average spin polarization of an ensemble of electrons, detectable via magnetization. Generally speaking, research in spintronics aims to understand the most effective ways to polarize an ensemble of spins, to detect such spin polarization, and to evaluate how long a system can remain spin polarized.[8]

Spin injection, detection and manipulation are essential mechanisms for device applications. Although electrons can also be polarized by transfer of angular momentum from polarized photons, purely electrical spin injection is more relevant for implementations in microelectronics. Electrical spin injection usually implies driving a current from a magnetic electrode to a substrate. The spin-polarized electrons injected create a nonequilibrium spin accumulation, which survives time scales (typically nanoseconds) determined by various spin relaxation and scattering effects. Spin detection, on the other hand, requires sensing a nonequilibrium spin population via changes in an electrical signal. This can as well be achieved by probing a sample though magnetic electrodes and taking advantage of magnetoresistive effects, as will be detailed later.

Spintronics can be traced back to seminal work by N. F. Mott in 1936, who first provided the foundations to understand spin transport in ferromagnets. He explained that the total current can be expressed as a sum of two non-mixing majority and minority spin projections.[9,10] In other words, the current within a ferromagnet is itself spin-polarized. Later investigations revealed that ferromagnetic barriers can be used to create a spin-filter: an initially unpolarized electrical current can become polarized when passed through a ferromagnetic material. When injected via ballistic transport (tunneling), the current can remain polarized outside of the ferromagnetic electrode. Extensive studies of this effect in FM/insulator heterostructures

established that tunneling contributes greatly to maintain high spin injection efficiency.[11,12] It is therefore important to review how spin injection proceeds via tunneling from a metallic contact.

2.1.2 Tunnel junctions

The tunneling current between two metallic contacts (not necessarily ferromagnetic) separated by an insulating tunnel barrier was studied theoretically by Simmons back in 1963.[13] He derived the characteristic exponential relationship of the current with respect to the barrier thickness, as expressed in this current-voltage ($I-V$) equation:

$$I(V) = f(t_b)\left[\left(\phi - \frac{V}{2}\right)\cdot e^{-(1.025\sqrt{\phi-\frac{V}{2}})t_b} - \left(\phi + \frac{V}{2}\right)\cdot e^{-(1.025\sqrt{\phi+\frac{V}{2}})t_b}\right] \tag{2.2}$$

where I is the tunneling current, ϕ the average barrier height, V the bias voltage applied across the junction, and t_b the barrier thickness in angstroms.[14] $f(t_b)$ is a correction factor depending on the barrier thickness.[13] Fig. 2.1 illustrates the tunneling of electrons through a thin insulating barrier and identifies the parameters involved in Eq. 2.2. In (a), an electronic wave function is traveling towards the barrier. If the barrier height is greater than the energy of the electron, the wave function becomes evanescent inside the barrier and decreases exponentially. However, for barriers thin enough (a few nanometers), the wave function does not completely vanish and a transmitted wave emerges on the other side with decreased amplitude. The probability of a tunneling event depends on the relative amplitudes of the incident and transmitted waves, hence on the barrier thickness t_b. A bias voltage applied on the junction, shown in (b), drives a current through the barrier depending exponentially on the potential eV.

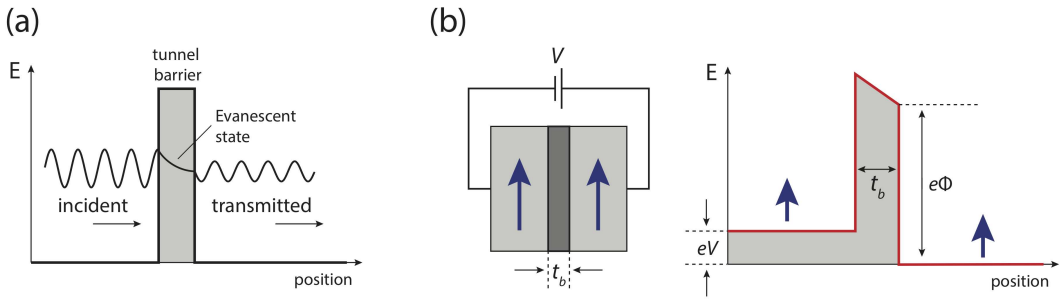

Figure 2.1: (a) Electron tunneling through a thin insulating barrier and (b) bias voltage applied across the junction as described in Simmons' I-V relation (Eq. 2.2).

2.1.3 Schottky barriers

An important aspect of FM/SC heterostructures is the formation of a Schottky barriers (SB) at the interface, which under some circumstances can act a tunnel barrier through which spins

can effectively be injected. This is a condition we are trying to exploit for the SS-SBTT (the spin-selective *Schottky barrier tunnel* transistor), on which more details will be given later in this chapter.

Schottky barriers arise at the interface between metals and semiconductors as a result of a mechanism known as Fermi Level Pinning (FLP), which describes a bending of the SC bands to accommodate surface and/or metal-induced gap states resulting in an alignment relative to the same Fermi level.[15] Depending on the strength of the FLP, the effective Schottky barrier height can vary. In weak cases, the barrier is easily overcome and the contact can be described as 'ohmic'. However, in most commercially used semiconductors (such as Ge), the FLP is considerable and leads to a Schottky barrier with rectifying signature. In particular, metallic contacts with *p*-type Ge are known to be ohmic, while contacts with *n*-type Ge are Schottky-like.[16,17] Fig. 2.2 (a) illustrates a single SB barrier arising at a metal-SC interface. This diagram shows how Schottky diodes are made possible, with the Fermi levels of the metal and SC being aligned.

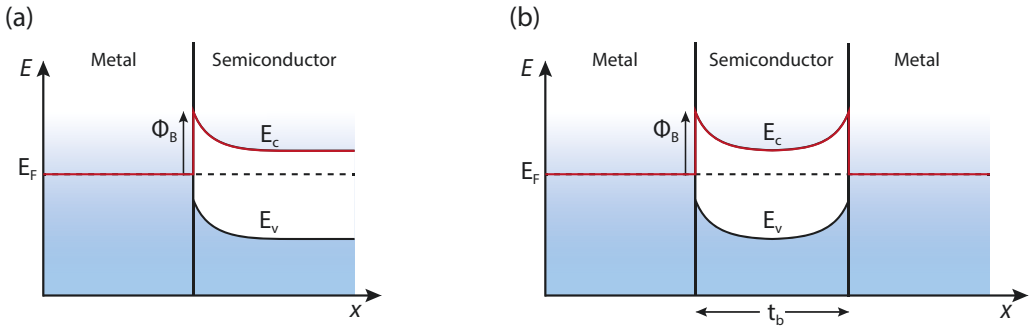

Figure 2.2: (a) Metal/semiconductor junction band diagram illustrating the formation of a Schottky barrier. (b) Metal/semiconductor/metal trilayer with double Schottky barrier, representing the ideal condition for a Schottky Barrier Tunnel Transistor (SBTT). The higher conduction band in the SC assumes *n*-type doping.

A Schottky barrier is not necessarily a tunnel barrier. Normally, transport over a SB is dominated by thermionic emission, with some contribution from tunneling.[18] Thermionic emission is the flow of charges *over* a potential barrier due to thermal energy. The velocity of electrons (the sea of electrons) follows a statistical distribution, and some electrons always have enough energy to overcome the barrier. Electrical conduction through normal Schottky diodes can be understood in terms of the thermal emission theory with

$$I(V) = I_s \left[exp\left(\frac{qV}{nk_BT}\right) - 1 \right] \tag{2.3}$$

with saturation current I_s

$$I_s = A_G A T^2 exp\left(-\frac{q\Phi_B}{k_BT}\right) \tag{2.4}$$

where T is temperature, k_B is the Boltzmann constant, q is the electron charge, A_G is the Richardson constant (about $0.5 \times 1.20173 \times 10^6$ A/m^{2}K^2), A is the surface area of the bar-

rier.[19] Φ_B is usually interpreted as the Schottky barrier height (SBH), although is in fact represents the average SBH. The parameter n is called the ideality factor and is usually between 1 and 2. However, for more complex barriers and junctions, it can regarded as a fitting parameter.[20] Alike tunneling, equation 2.3 shows that charge carriers overcoming the SBH when a bias voltage is applied translates into a rectifying behavior with exponential *I-V* relationship.

Fig. 2.2 (b) illustrates what happens in a metal-SC-metal trilayer: the band bending is symmetric. Provided that the metallic contacts are identical and made with the same material, an equivalent barrier emerges at the second interface. The idea to separate two metallic contacts by a thin SC was the basis for the original Schottky barrier tunnel transistor (SBTT) suggested by K. Wu.[21] In general, this configuration is also more realistic than the simple Schottky diode shown in (a), since probing the junction implies contacting the semiconductor with another metal, which in turn results in an additional barrier. It is still possible to extract the Schottky parameters of these trilayers from a single *I-V* curve, thanks to an approach develop by R. Nouchi.[18]

In the context of our application for the SS-SBTT, the SC buffer layer (t_b) between two FM contacts should be thin enough such that tunneling events dominate through the double SB created. In this way, the FM/SC/FM trilayer can be thought of as a conventional magnetic tunnel junction (MTJ), which supports spin-selective tunneling. Importantly, even if the dominating transport mechanism across the junction is thermionic emission, it was shown that spin selectivity can in this case also be preserved[22], which would not hinder the functioning of the SS-SBTT.

2.1.4 Magnetic tunnel junctions

In 1975, M. Jullière studied the tunneling conductance in Fe/Ge-O/Co trilayers at low temperature.[23] In his set-up, the two metallic electrodes are made of ferromagnetic materials (FM1, FM2) having different coercivities, which allowed to switch the magnetization of the two layers independently when applying an external magnetic field. He noticed that the system could be swapped into two states of electrical resistance, depending on the relative orientation of the magnetization of FM1 and FM2. If the layers are in parallel configuration ($\uparrow\uparrow$), the probability of an electron tunneling from one FM layer to the other is higher, resulting in a low resistance state. In the antiparallel configuration ($\uparrow\downarrow$), the effect is reversed and the system enters a high resistance state. Jullière formulated a model to understand this tunnel magnetoresistance (TMR) in a magnetic tunnel junctions (MTJ). The TMR ratio, interpreted as a percentage of resistance change, is expressed

$$\text{TMR} := \frac{\Delta R}{R_{\uparrow\uparrow}} = \frac{R_{\uparrow\downarrow} - R_{\uparrow\uparrow}}{R_{\uparrow\uparrow}} = \frac{G_{\uparrow\uparrow} - G_{\uparrow\downarrow}}{G_{\uparrow\downarrow}} \tag{2.5}$$

where the resistance R and conductance $G = 1/R$ are labeled according to the respective magnetization of the FM1 and FM2 films. Fig. 2.3 illustrates schematically the parallel and antiparallel spin-conserved tunneling mechanisms in such a MTJ. In the parallel magnetization configuration, the spins from the majority $\uparrow$ subband tunnel to a comparably large bath of

available ↑ states below the Fermi energy. This corresponds to a maximum tunneling amplitude and low resistance state. In the antiparallel configuration, the same spins can only reach the minority spin subband of the second ferromagnetic layer. The lower number of available spin states reduces tunneling events, thus increasing the system's resistance.

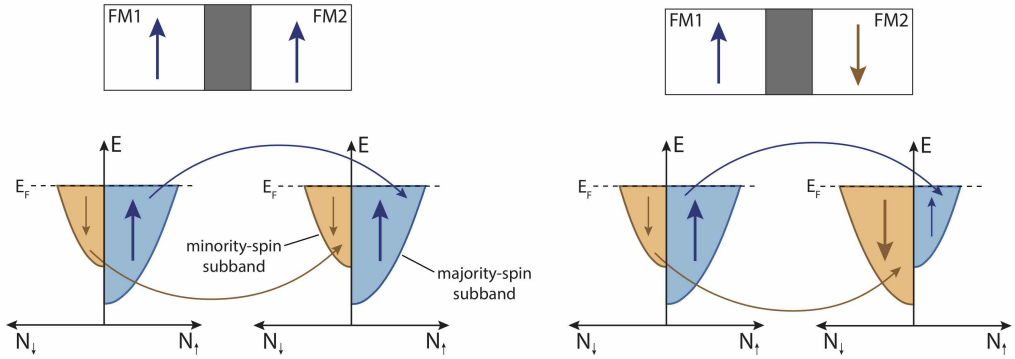

Figure 2.3: Schematic diagram showing electrons tunneling in a MTJ in the low resistance (left) and high resistance (right) states. Both minority and majority spins contribute to the total tunneling current (two-current model).

Jullière's model assumes that spin is conserved upon tunneling from one layer to another. Within this assumption, the total current can be described by a two-current model (as originally proposed by Mott), whereby the spin up and down electrons split into two partial unmixed currents. Since both majority and minority spins take part in the total conductance, it is convenient to express the TMR in terms of the polarization P of each layer. P is related to the spin-dependent density of states (DOS) $\mathcal{D}$ at the Fermi energy[14], and can be expressed in the following way:

$$P = \frac{\mathcal{D}_\uparrow(E_F) - \mathcal{D}_\downarrow(E_F)}{\mathcal{D}_\uparrow(E_F) + \mathcal{D}_\downarrow(E_F)}. \tag{2.6}$$

Equation 2.5 then becomes

$$\text{TMR} = \frac{P_1 P_2}{1 - P_1 P_2}. \tag{2.7}$$

2.1.5 The spin valve effect

A typical measurement of the TMR in a MTJ reveals the *spin valve effect*, illustrated schematically in Fig. 2.4. Current is applied across the barrier through the FM electrodes, and voltage is recorded as the external magnetic field is swept. At high positive field (blue curve), the layers are in the ↑↑ configuration and the resistance sits at its lowest. As the field is decreased and eventually reversed, the magnetization of a first layer flips. The ↑↓ system is then in a high resistance state. The magnetization of the second layer eventually switches, leading back to a ↓↓ low resistance state. The same is observed on the opposite direction of the hysteresis loop (orange curve). The TMR ratio is extracted from such measurements, taking spin-valve signal amplitude and applying Eq. 2.5.

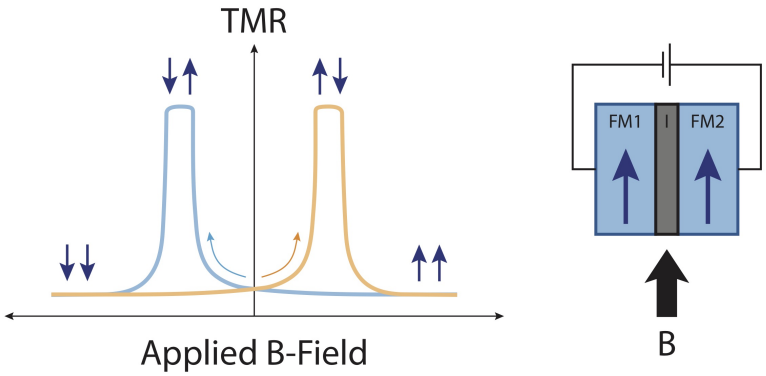

Figure 2.4: Schematic diagram showing a typical spin valve signal. Electrons tunneling in a MTJ with ↑↑ configuration shows small tunnel magnetoresistance (TMR). As an external field (B) is swept, the magnetization of one layer is flipped, which bring the MTJ in the high ↑↓ TMR state. Further increasing the magnetic field amplitude brings both layers in the ↓↓ state, with low TMR. The effect is observed while reversing the direction of the hysteresis loop.

State of the art MTJs are realized using crystalline magnesium oxide (MgO) as tunnel barrier. Fe/MgO/Fe heterojunctions were studied experimentally and theoretically in the early 2000's, the most optimistic calculations predicting a TMR ratio in excess of 1000%.[24] Experimental investigations, however, could only produce room temperature TMR up to ∼220%.[25] A record high room temperature TMR of 604% was realized in 2008 in CoFeB/MgO/CoFeB junctions.[26] A giant TMR ratio of 2610% at 4.2 K was reported more recently by Liu *et al.* in Co_2(Mn,Fe)Si/MgO-based MTJs.[27] MgO is used as an insulating tunnel barrier since it was shown to offer additional spin filtering[28,29], which exacerbates the spin valve effect resulting from FM layers being made with materials having a high magnetic polarization.

2.2 The Spin-Selective Schottky Barrier Tunnel Transistor

2.2.1 General idea

With the necessary building blocks discussed above, we can now detail the functioning of the SS-SBTT, which is the technological motivation behind the experimental work presented in this thesis. The purpose of the SS-SBTT is to serve as a transistor which can operate within the paradigm of spintronics. This approach intends to build on conventional *bivalent* logic systems (Boolean logic outputting 'True' of 'False'), and to use the information contained in spin-polarized currents to implement a *many-valued* logic. It is then essential to have a transistor which can modulate spin-polarized currents while preserving the extra information being encoded. The central idea is to modify a MTJ such as to turn it into a Schottky barrier tunnel transistor.[21] As explained in the previous section, MTJs are inherently spin-selective, or at least *spin-sensitive* so far as the ferromagnetic electrodes are spin polarized and the TMR is measurable. By replacing the usual insulating tunnel barrier of a MTJ by a semiconducting material, one would combine the Schottky barrier transistor idea of Wu

and obtain a way to modulate the spin-polarized tunnel current by modifying the average barrier height via the application of an electrostatic bias voltage. The requirements to create a functional SS-SBTT are similar to those of a conventional MTJ. However, to ensure high spin injection efficiency, one should ideally grow fully crystalline, lattice-matched ferromagnet/semiconductor/ferromagnet heterojunctions. The creation of such structures is usually attempted by MBE. However, the growth of the semiconductor interlayer over the first ferromagnetic metal is experimentally challenging due to possible intermixing.

2.2.2 Operation

Fig. 2.5 illustrates the SS-SBTT with superimposed electron energy band diagram. The device resembles a conventional MTJ, where layer 1 and 3 are the emitter and collector, made of FM metals. The base is layer 2, made of a semiconductor. The juxtaposition of a metal with a semiconductor creates a Schottky barrier which can support spin injection.[30,31] A first Schottky barrier arises at the interface between layer 1 and layer 2, and a second Schottky barrier arises between layer 2 and layer 3. If layer 2 is itself thin enough (a few nanometers), those two Schottky barriers will likely merge and appear as only one potential 'wall'. By engineering this potential wall thin and high, the electrical conduction between layer 1 and 3 should ideally be dominated by tunneling events. The height of the Schottky barrier (noted ϕ_B), as well that the barrier thickness, influence the likelihood of a tunneling event (as described by Simmons in Eq. 2.2). The higher the barrier is, the lower the probability of a tunneling event. By doping the semiconductor layer 2, applying an electrostatic voltage via contact B can modify the barrier height ϕ_B. When a voltage is applied between contact A and contact C, the base voltage V_B can therefore control the tunneling current level, thereby switching the device 'ON' and 'OFF'.

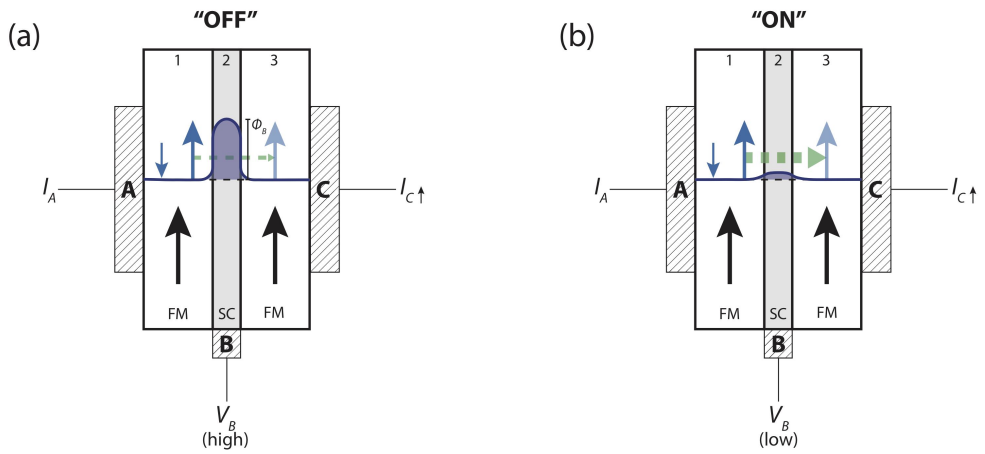

Figure 2.5: (a) The high voltage V_B applied on SC contact B raises the Schottky barrier height Φ_B, making tunneling events less likely and the spin polarized current I_C smaller. (b) A smaller V_B decreases Φ_B, which results in a higher output current I_C.

In Fig. 2.5, both ferromagnetic layers are upward polarized, so mainly upward polarized electrons from layer 1 will reach layer 3, as described by the TMR effect. In (a), a high voltage V_B applied on contact B raises the Schottky barrier height ϕ_B. Tunneling events are less likely, and the spin polarized current I_C is smaller. In (b), a smaller V_B decreases ϕ_B, which results in a higher output current I_C. One should note that the SS-SBTT device concept does not necessarily take advantage of the 'high' magnetoresistance state that arises from the $\uparrow\downarrow$ configuration of the FM layers (although this possibility could also be exploited in the future). Only the $\uparrow\uparrow$ configuration is utilized here to preserve the information encoded in a spin-polarized current. The SS-SBTT can then be used as a "conventional" transistor, however offering the advantage of operating on a polarized base current, and outputting a comparably polarized collector current.

As implied in the descriptions provided above, the SS-SBTT is a *vertical* transistor. The parts corresponding to the collector, base, and emitter are the sequentially grown FM/SC/FM layers. To operate the SS-SBTT, each layer should then be independently contacted via a series of etching and patterning steps. This geometry is contrasted with transistors in which the collector, base and emitter are placed in a *lateral* configuration. Although it is possible to imagine a lateral transistor made of FM contacts as described above, our vertical approach offers important advantages. Indeed, the thickness of the SC tunnel barrier can be controlled precisely when grown vertically by MBE, as opposed to being deposited in laterally etched space. Another crucial aspect of the vertical geometry is that the thin film stacks can be grown fully lattice-matched with atomically flat interfaces, which as will be explained below, is beneficial to preserve higher spin-injection efficiency.

2.2.3 Growth challenges

The fabrication of the SS-SBTT described above requires solving a series of technical challenges related to the growth of semiconductors over metals by MBE. Studies of spin injection from ferromagnets to semiconductors are usually done in bilayer systems, where a metal is grown lattice-matched *over* a semiconducting substrate. This approach is easier since the semiconductor surface will remain stable at temperatures where most metals are grown, which prevents intermixing and the formation of undesirable byproducts at the interface. In the specific context of this research, Ge can be grown crystalline by MBE in the 300°C range, while the ferromagnetic quasi-Heusler metal Fe_3Si requires temperatures that are closer to 200°C.[32] The latter can be safely grown on top of Ge (or GaAs) while preserving impeccable interface quality. Prior investigations (to be discussed later) showed that it is however not directly possible to grow crystalline Ge on a Fe_3Si surface without degradation of the interface and chemical reactions yielding secondary compounds. Generally speaking, semiconductors require higher growth temperatures at which the chemical stability of metals (and ferromagnetic Heusler alloys) is threatened.

The incompatible crystallization energies of semiconductors and metals is the main limiting factor to realize the FM/SC/FM trilayers required for the SS-SBTT, as it prevents to realization of high-quality and sharp FM/SC interfaces. Indeed, it is known that the details of

the atomic ordering should be carefully controlled, as they can influence the magnitude and sign of the injected spin carriers.[33] Schmidt *et al.* first shed light on the so-called conductivity mismatch problem in FM/SC microstructures, which is the basic obstacle to spin injection in the diffusive regime.[34] E. I. Rashba then suggested that the problem can be solved by inserting a tunnel contact between the FM and SC layers.[12] This result implies that a high and well-behaved Schottky barrier can act as an interstitial tunnel contact to support spin injection in FM/SC junctions. Still, the potential barrier profile is itself critical to preserve spin coherence.[35–37] Efforts to obtain ordered and coherent FM/SC interfaces consisting of monoatomic planes has shown drastic increase in spin-injection efficiency (up to 44%).[38] It therefore appears critical to find a way to obtain lattice-matched SC over a FM substrate in order to obtain FM/SC/FM trilayers. This growth challenge is especially suited for MBE, given the possibility it offers to engineer crystals with sub-nanometer precision, and overall importance in the realization of lattice-matched heterostructures.

2.3 Heusler Alloys

As seen form the type of devices described above, applications in spintronics have motivated a search for highly spin-polarized materials which could readily be integrated within the semiconductor industry. As explained in Jullière's model for magnetic tunnel junctions, a large polarization P would yield a larger tunnel magnetoresistance, and thus improve spin detection sensitivity. In the extreme –or ideal– case, a fully polarized material ($P = 100\%$) would show no minority spin subband at the Fermi level, as illustrated in Fig. 2.6. Such materials, called *half-metals*, have been predicted theoretically in an number of contenders belonging to the Heusler alloys.[39–42]

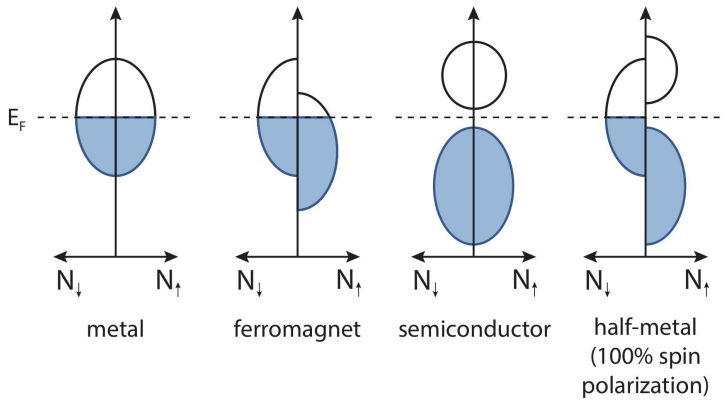

Figure 2.6: Density of states for the spin up and down subbands in different materials. The rightmost case corresponds to so-called half-metals, where only one spin subband remains non-zero at the Fermi level E_F.

2.3.1 Structure and tunability

The Heusler alloys, originally discovered by F. Heusler[43], form a large group of intermetallic compounds (∼1500 members).[44] They consist in two interpenetrating face-centered cubic (fcc) lattices, with formula X_2YZ ("full-Heusler") or XYZ ("half-Heusler'), where X and Y are usually transition metals and Z a main group element.[45] The Heusler structures relevant to our study, shown in Fig. 2.7 (a) and (b), are subdivided according to the ordering of the Y and Z atoms: the $L2_1$ phase represents to the fully ordered structure in (a), while the B2 is disordered. Some Heusler compounds can also follow a X_2XZ formula, in which case their structure corresponds to a $D0_3$ ordering.[44] The possibility to tune the composition and stoichiometry of Heusler alloys gives access to materials with a wide range of electrical, magnetic, and optical properties, which can conveniently be predicted based on the number of valence electrons per formula unit (VEC).[44] A large subset of Heusler alloys are ferromagnetic (corresponding to 17 or 19 VEC) while being lattice-matched with III-V semiconductors, which makes them especially well suited to realize semiconductor spintronics devices and applications.[46]

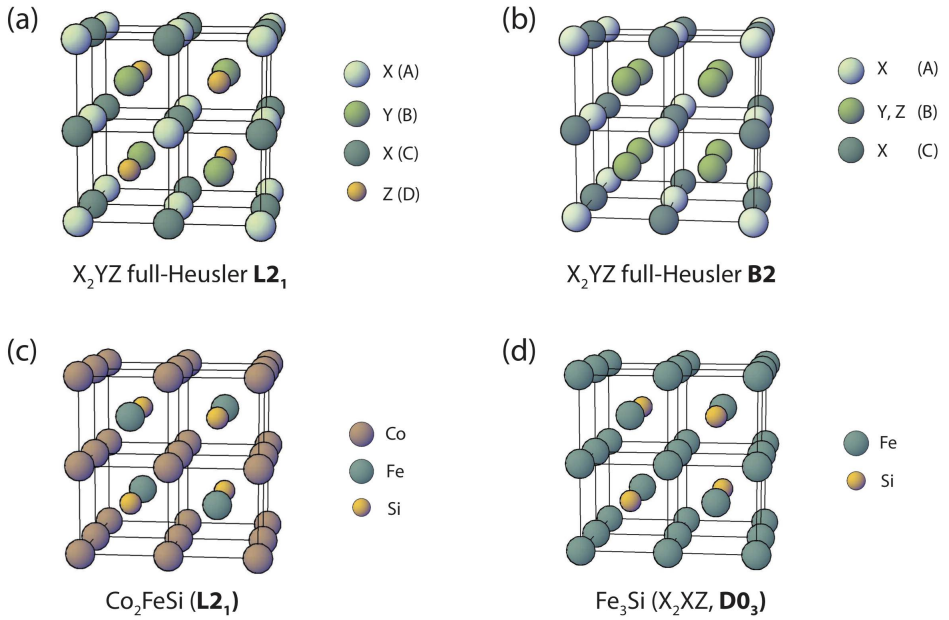

Figure 2.7: (a) X_2YZ full-Heusler alloy structure in the $L2_1$ phase (b) X_2YZ full-Heusler alloy structure in the B2 phase, with disordered Y and Z atoms. (c) The fully ordered $L2_1$ structure of Co_2FeSi. (d) The $D0_3$ structure of Fe_3Si.

The ferromagnetic Heusler alloys used in this research are pictured in Fig. 2.7 (c) and (d), namely Co_2FeSi (in the fully ordered $L2_1$ phase) and Fe_3Si ($D0_3$ phase). Co_2FeSi, when in the $L2_1$ phase, is of particular interest since it is suspected to be a half-metal[39–41]. This property is still disputed among the community, and other studies show that the compound can be expected to offer a minimal degree of spin polarization in the 40- 60% range.[47] Co_2FeSi has a lattice constant matched to GaAs (and Ge) within ∼0.08%.[48] Furthermore, Co_2FeSi has a

magnetic moment per unit formula of $5\mu_B$, the highest among all Heusler alloys, as well as a Curie temperature of 1100 K, also the highest value reported.[49] The growth of $L2_1$ Co_2FeSi is however notoriously delicate[48], and preserving the integrity of the ordering is problematic in our attempt to develop a SPE approach. Fe_3Si is a more stable candidate to attempt annealing experiments, while offering advantages comparable to those of Co_2FeSi. It has identical lattice constant, meaning that it can be grown lattice-matched on GaAs and Ge.[32,50] Fe_3Si also has one of the highest Curie temperature among Heusler alloys, and shows magnetic polarization up to 45%.[51]

2.3.2 Growth of Fe_3Si and Co_2FeSi layer stacks for spintronics

The growth of Heusler alloys on semiconductor substrates has been studied extensively in the past. Research done in this direction has been strongly connected to the field of semiconductor spintronics[52], in which the integration of ferromagnetic electrodes plays an essential role. More specifically, the growth of Fe_3Si and Co_2FeSi on GaAs, Si and Ge has shown promising results, given the lattice compatibility of the materials allowing to create heterostructures with sharp interfaces, ideal for spin injection and detection.[53] The growth of fully ordered crystalline Fe_3Si and Co_2FeSi on GaAs(001) is now routinely achieved, thanks to developments made since the last 20 years.[32,48,54] Those advances led to the growth procedures that will be described in the subsequent chapters. The growth of these compounds was successful on different surfaces and orientations, notably Co_2FeSi on GaAs(110)[55,56], GaAs(111)[57], Ge(111)[58] and Si(111)[59]. Fe_3Si was also grown on Si(111)[60] and Ge(111).[61–63] The realization of high quality thin films enabled extensive study of these materials' magnetic properties, showing characteristic magnetocrystalline anisotropy, small coercivity and weak temperature dependence of the magnetization with elevated Curie temperature.[64] Nonetheless, the diffusion of Ge atoms into Fe_3Si during epitaxy is known to degrade the magnetic properties of the film.[65]

The spin injection from various ferromagnetic Heusler alloys to GaAs, Ge and Si was the subject of past and ongoing investigations. The Schottky barrier arising at the interface between Fe_3Si and Ge(111) was determined to be 0.52 eV.[66] The rectifying *I-V* characteristics of the barrier was observed in Fe_3Si/n-Ge junctions at low temperatures, although an Ohmic contact formed at the Fe_3Si/p-Ge interface due to dominating Fermi level pinning (FLP) mechanisms.[17,67] Spin injection from Fe_3Si to p-Ge could be realized with spin diffusion length of $\sim$50 nm at 10 K,[68] and was also demonstrated in n-Ge.[69] These results indicate that MBE-grown Fe_3Si/Ge heterojunctions are suitable for spintronics applications. Furthermore, the realization of lattice-matched vertical trilayers, with two FM contact are separated by a metallic or semiconducting buffer layer, was attempted using different strategies. Notably, $Fe_3Si/Al/Fe_3Si$ trilayers were realized by MBE on GaAs(001) substrates. In this case, the growth orientation is not preserved as the Al crystallizes mostly in the (111) orientation, and the capping Fe_3Si layer is polycrystalline, as illustrated in the TEM images and EBSD map shown in Fig. 2.8.[70] The growth of Ge over metallic substrate was investigated by other

groups using low-temperature MBE[71–73] and surfactant-mediated MBE,[74,75] providing alternative avenues to eventually realize comparable lattice-matched FM/SC/FM trilayers.

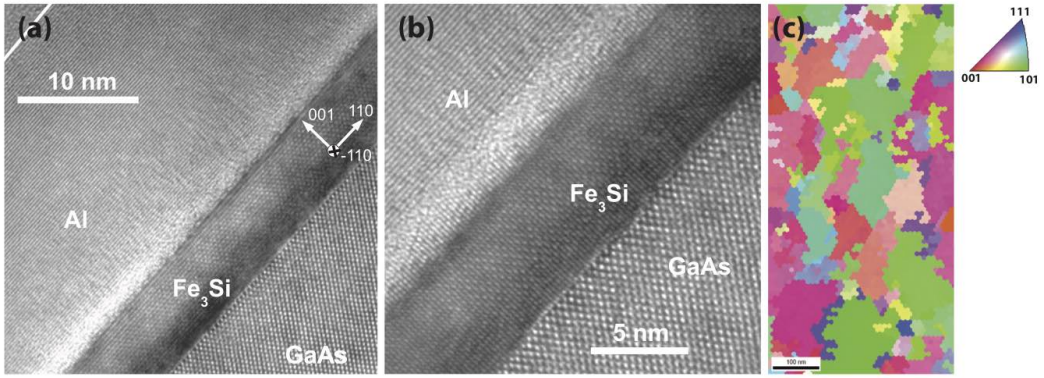

Figure 2.8: (a) and (b) Cross-sectional HRTEM images of a Fe_3Si/Al/Fe_3Si thin film stack showing the high quality of the first layers. However, in (c) the EBSD map of the capping Fe_3Si shows that it is mostly polycrystalline.[70]

The realization of Fe_3Si/Ge/Fe_3Si trilayers has been attempted in the recent years by conventional low-temperature MBE techniques, providing insights that are of great importance for the work presented in the thesis.[76,77] In these experiments, Ge was directly grown over Fe_3Si at different temperatures in order to assess the possibility to obtain crystalline films while preserving good interface quality. A capping Fe_3Si was then deposited on the Ge film, irregardless of the crystallinity of the underlying layers. It was found that this approach could only produce layer stacks with limited quality. Indeed, stacking faults were observed by TEM in earlier investigations made along the GaAs(111) substrate orientation, especially within the Ge layer (that was grown at 200-250°C).[76] The top Fe_3Si obtained was polycrystalline, including some Fe_3Si(110)regions within the otherwise (111)-oriented film. More recently, such investigation were carried along the GaAs(001) orientation. The TEM images of the resulting stacks are shown in Fig. 2.9.[77] A first sample, shown in (a), is a Fe_3Si/Ge/Fe_3Si trilayer for which the Ge interlayer was deposited at 150°C. It is possible to see that the Ge film is completely amorphous, while preserving a sharp interface with the underlying crystalline Fe_3Si layer. The top Fe_3Si deposited over the amorphous Ge is seemingly amorphous, as illustrated by the the EBSD image shown in (b) which contains essentially randomly oriented domains. As the growth temperature of Ge was increased to 225°C, the film evolved from amorphous to polycrystalline. The interface remained smooth, although with some thickness inhomogeneity visible in (c). The capping Fe_3Si layer grown in this sample had a high degree of polycrystallinity, confirmed by the EBSD image in (d). Lastly, a sample in which the Ge layer was grown at 325°C is shown in (f). In this case, the interface remained relatively rough over approximately 20% of the sample. The quality of the Ge film was improved by the higher growth temperature, although with sub-optimal crystallinity. Once again, the capping Fe_3Si layer studied by EBSD (f) was found to be polycrystalline. The overall quality of the film is however improved, with up to 80% of the domains correctly oriented in the (001) direction.[77]

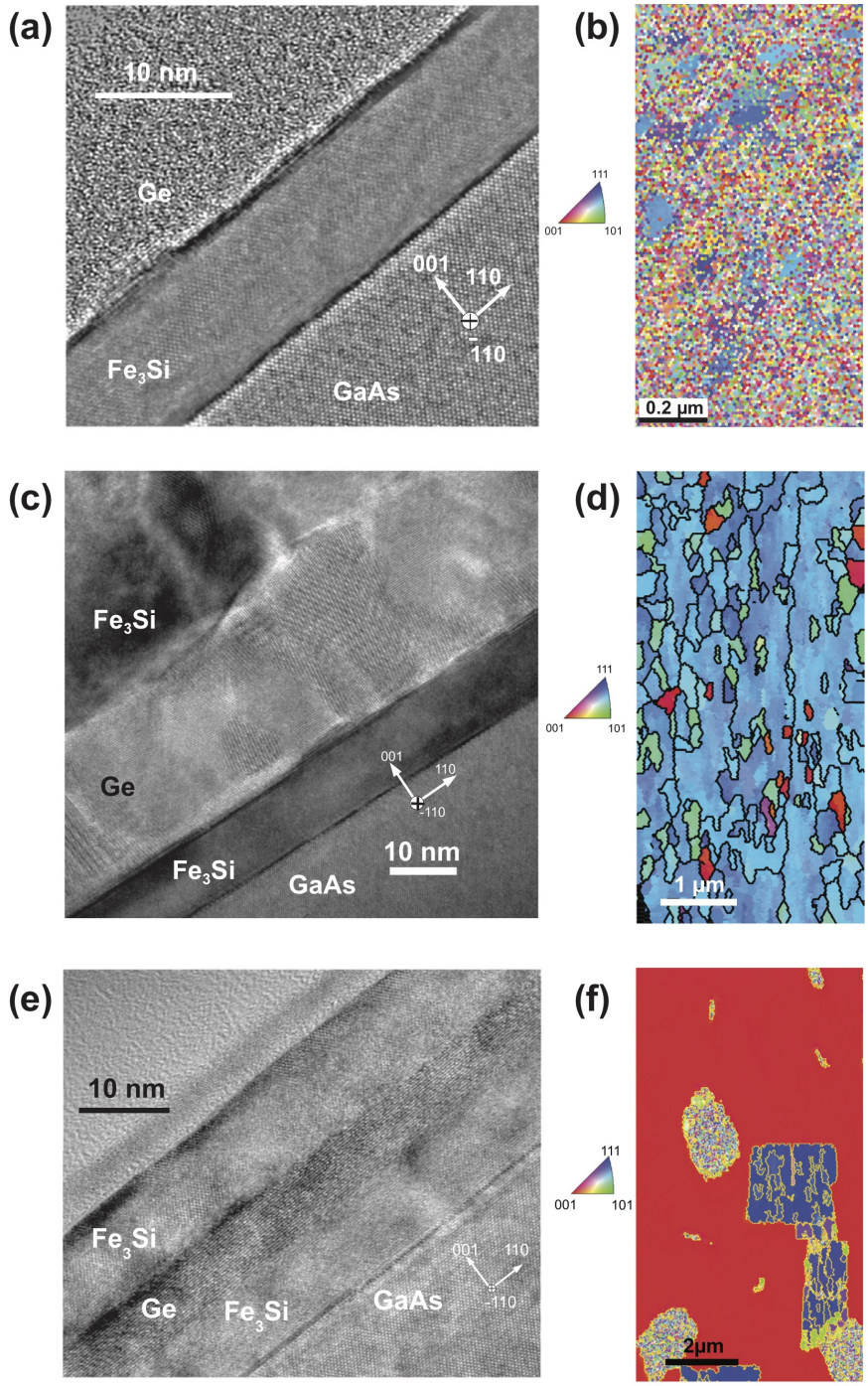

Figure 2.9: Cross-sectional HRTEM images of three $Fe_3Si/Ge/Fe_3Si$ thin film stacks in which the Ge layer is deposited at 150°C (a), 225°C (c), and 325°C (e), showing the progression of the Fe_3Si/Ge interface and crystallinity of the Ge layer. (b), (d) and (f) show EBSD images performed on the top Fe_3Si layer for the three previous samples, all cases illustrating the polycrystalline nature of the capping films.[77]

Those results indicate that the direct growth of Ge over Fe_3Si by MBE is not a successful approach to obtain fully crystalline, lattice-matched trilayer stacks. Indeed, low growth

temperatures can preserve sharp interfaces, but the Ge and capping Fe_3Si films remain amorphous. Higher growth temperatures can, in the best case, produce crystalline Ge and Fe_3Si layers that are 80% correctly oriented, while significantly damaging the Fe_3Si/Ge interface. The technical difficulty to grow crystalline Ge over the Fe_3Si surface is the motivation behind the solid-phase epitaxy approach which is central to this thesis.

2.4 Magnetism

The field of spintronics is based on the control of electron spins, which is tightly connected to the notion of magnetization. It is therefore important to review some fundaments of magnetism in order to better appreciate the results which will be discussed in this thesis, both quantitatively and qualitatively. Indeed, the magnetization of the thin films used as electrodes for spin injection in the heterojunctions we aim to create will help determine the best approach to successfully implement a SS-SBTT. This section will first review some essential aspects of magnetism, with a focus on single-crystalline ferromagnetic thin films, and describe the phenomena useful for the interpretation of our experimental findings.

As mentioned previously, each electrons has an intrinsic magnetic dipole moment related to its spin $\boldsymbol{S}$ expressed $\mathbf{m} = -g_s\mu_B\frac{\mathbf{S}}{\hbar}$. Electrons therefore already behave like small magnets, with quantum mechanical spin being either "up" or "down". Macroscopic effects such as ferromagnetism come from an alignment of the dipole moments contained in a material. However, such effect is only possible in elements with unpaired spins. For all filled electrons shells, the paired electrons have opposite spins which cancel each other, resulting is a dipole moment of zero. If unpaired electrons are found, they tend to align with external magnetic fields, an effect called paramagnetism. Ferromagnetism is the *spontaneous* alignment of unpaired electrons, even without the application of an external magnetic field. The conditions for ferromagnetism are realized in some transition metals, notoriously Fe, Ni and Co, due to the exchange interaction between the unpaired electrons in their *3d* shell. Importantly, ferromagnetism is also realized in many Heusler alloys involving these compounds, such as Fe_3Si and Co_2FeSi.

2.4.1 Magnetization

The magnetization of a material can be understood as a density of (many) magnetic dipole moments **m**:

$$\mathbf{M} = \mathbf{m}\frac{N}{V} \tag{2.8}$$

where N/V represent a number per volume component. The **M** field represents the "degree" to which the electron spins are aligned in a given material. Those spins are susceptible to external magnetic fields, hence it it possible to control a material's magnetization. In vacuum, the relationship between magnetic field strength **H** and magnetic induction **B** is $\mathbf{B} = \mu_0\mathbf{H}$, where μ_0 is the permeability of vacuum. However, the magnetization *inside* a material must

involve the material's magnetization, and the relationship between **B** and **H** becomes:

$$\mathbf{B} = \mu_0(\mathbf{H} + \mathbf{M}). \tag{2.9}$$

The relation which is more relevant for our measurements is the direct dependence between **M** and **H** taken together. The magnetization observed in a material is related to the applied magnetic field strength by a factor χ called the magnetic susceptibility[78], and can be expressed

$$\mathbf{M} = \chi\mathbf{H}. \tag{2.10}$$

The magnetic susceptibility χ can be either positive for a paramagnetic material, or negative, in which case the material is called 'diamagnetic'. The GaAs substrates used in this thesis are diamagnetic. As will be explained later, this negative contribution to the magnetization has to be removed in order to reveal the magnetization of the thin ferromagnetic films stacks.

2.4.2 Thin-film ferromagnets

In ferromagnetic materials, χ is not well defined. Instead, a magnetization measurement will exhibit a so-called hysteresis loop: the $M(H)$ curve is not linear and does not pass through the origin. The recognizable shape of the hysteresis loop is caused by the fact that ferromagnets have non-zero *coercivity*, meaning that they can resist the effect of an external magnetic field up to a certain point before becoming demagnetized. 'Hard' magnetic materials have high coercivity, while 'soft' magnetic material have a low coercivity. This property is also related to *remanence*, which quantifies the magnetization of a ferromagnet left after removing the external magnetizing field.

A typical magnetic hysteresis loop is shown in Fig. 2.10. Assuming that the field sweep begins at high positive H, the system is in the magnetization saturation state (M_s), meaning that all possible available electron dipoles are aligned along H (blue curve). The field strength is decreased and ultimately passes the origin, at which point the remaining magnetization is the remanence M_R. As the field is further decreases, the magnetization remains positive as the system resists being demagnetized. The coercive field H_C corresponds to the field strength required to effectively switch the sign of M. The system then aligns along the reversed applied magnetic field. The same effect is observed along the other direction of the loop (purple curve).

The actual 'sharpness' of the magnetic switching is related to the *magnetic anisotropy* of the material, which generally describes the fact that it can be easier to magnetize a material along specific orientations. There are different types of magnetic anisotropy. The primary one is magnetocrystalline anisotropy, which comes from spin-orbit interactions coupling the spins orientation with the orientation of the electronic orbitals. In crystalline ferromagnets, the consequence is that the magnetic energy depends on the direction of the external magnetic field with respect to the crystal axes.[78] The orientation which yields the lowest energy is called the *easy axis*. The hysteresis loop taken along an easy axis will exhibit very sharp magnetization reversal, while the hard axis will usually switch more gradually. Depending on the details

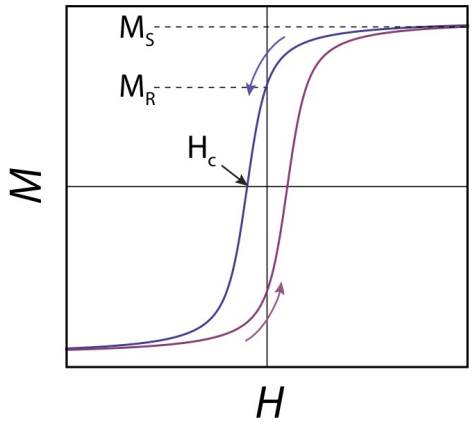

Figure 2.10: A typical hysteresis loop in a ferromagnetic material, identifying the coercive field H_C, remanence M_R and saturation magnetization M_S.

of the atomic ordering of its crystal lattice, a ferromagnet can have cubic magnetocrystalline anisotropy where the easy axes are 90°apart, or *uniaxial* magnetocrystalline anisotropy where the easy and hard axes are 90°apart. The Heusler alloys used in this thesis, Fe_3Si and Co_2FeSi, have cubic magnetocrystalline anisotropy.[64,79]

Another important type of anisotropy is *surface/interface* anisotropy, which becomes relevant in thin films samples. Intuitively, as the film thickness is reduced, the 'bulk' of the material becomes less and less significant compared to the atoms situated at the surface. In this case, the interruption of the crystal lattice will generate 'missing' binding partners and interfere with the behavior of spins involved in these orbitals (actually increasing the magnetic ordering[80]). For thin film heterostructures, the presence of different interatomic bonds can also significantly modify the measured magnetization. The anisotropy energy associated to the surface and interface in a thin layer can be written

$$E_i = \frac{2K_s}{t}\sin^2\theta \tag{2.11}$$

where t is the film thickness, the factor 2 comes from the two interfaces, K_s is introduced as the 'surface anisotropy constant', and θ is the angle between the magnetization and the surface direction.[80] The energy is minimal for $\theta = 0$, so when M is out of plane. This is usually not the case when studying the magnetic properties of thin films: the magnetization is kept *in*-plane, meaning that this anisotropy is maximized.

A third source of anisotropy is attributed to the *shape* of the crystalline samples. Its energy is in the form

$$E_s = \frac{1}{2}\mu_0 M^2\cos^2\theta \tag{2.12}$$

where θ is also the angle between the surface plane normal vector and M.[80] The energy is minimal when the magnetization is in-plane ($\theta = \pi/2$). Furthermore, the effect would also become noticeable for thin film samples that are very asymmetric (extremely long and nar-

row), in which case the magnetization would also be favored along the length. This situation is not optimal to study thin film magnetism, and the samples should be kept relatively square in order to avoid obstructing the more insightful magnetocrystalline anisotropy.

3 Apparatus and Measurement Techniques

This chapter covers the technical aspects related to the fabrication and measurement of the samples, as well as the theory behind the functioning of the measurement devices. The first section of the chapter describes the growth-related methods, covering MBE, SPE and RHEED. The second section explains the characterization techniques and apparatus. For the thin films grown by MBE and SPE, those techniques are mainly XRD, TEM, AFM and SQUID magnetometry. The preparation of samples for magnetotransport is described afterwards, along with details regarding the the electrical probing methods and the cryostats in which the samples are inserted for the experiments.

3.1 Sample growth

3.1.1 Molecular beam epitaxy

The idea of MBE is to direct a beam of molecules or atoms on a heated substrate, on which they will settle into a given crystalline phase. The rates at which the atoms are deposited on the substrate can be finely tuned in order to achieve single-crystalline thin-films with sub-nm thickness precision, as well as sharp doping density profiles. Alike other deposition techniques, such as atomic layer deposition (ALD) and chemical vapor deposition (CVD), MBE features slow deposition rates which enables the films to grow epitaxially[1], i.e. with new atomic sheets being deposited and effectively continuing the crystalline lattice. However, MBE does not employ carrier gases or precursors, and operates in ultra-high vacuum (UHV) environments (typically $p < 10^{-8}$ mbar), and is therefore the technique through which samples can be created with the highest purity. For those reasons, MBE has played — and continues to play— an important role in our understanding of semiconductors and for the development of new technologies.

The molecular beams are created by evaporation from Knudsen effusion cells containing ultra-pure elements. The crucibles are electrically heated until the atoms they contain sublimate. The evaporated atoms are released in the growth chamber through a mechanical shutter. The PID-controlled temperature of the crucible regulates the flux generated from the cells, and ensures stable deposition rates. Precisely, the evaporation rates are adjusted by measuring the beam-equivalent pressure using a Bayard–Alpert ionization gauge. In UHV,

[1] Term coined by Tuomo Suntola in the 1970's, from Greek *epi* 'upon' and *taxis* 'arrangement'.[81]

the mean free path between the atoms is large, meaning that the elements forming the beams will not interact until they reach the substrate. The temperature of the substrate is also critical to control the formation of crystalline compounds, whose stoichiometry can be determined by thermally activated reactions.

Once reaching the substrate, the atoms can crystallize into thin films following different growth modes which depend strongly on the diffusion of the adatoms towards the surface on which they are deposited. In the Volmer-Weber mode, the growth dynamics proceeds via nucleation of adatoms into 'islands' which then extend to cover the surface. This occurs when the interactions between the adatoms are stronger than their affinity for the surface, and usually produces relatively 'rough' surfaces. On the other hand, when the diffusion of the adatoms on the surface is favored, the crystallization will proceed in a 'layer-by-layer' fashion, called Frank-van der Merwe growth mode. This ideal mode is suitable to achieve atomically flat layer with lattice-matched films, and depicts the formation of a complete monolayer before the next one starts to form. Growth can also occur in a hybrid 'layer-plus-island' mode, called Stranski-Krastanov. In the specific case of Fe_3Si and Co_2FeSi grown over GaAs(001), the lattice mismatch is negligible and the films are known to grow in a pseudo-Frank-van der Merwe mode.[82]

3.1.2 The MBE5 cluster

All samples studied in this thesis were grown in the MBE cluster depicted in Fig. 3.1. The main elements of the system are the load-lock, III-V and metal growth chambers, separated by intermediary 'middle chambers' (MC1, MC2). The system comprises another growth chamber dedicated to oxide compounds, also shown in the diagram. Each of those maintain a base pressure $< 10^{-10}$ mbar, thanks to a system of cryopumps and liquid nitrogen cooling within the walls of the growth chambers, which thereby act as a sink for remaining impurities. The III-V semiconductor growth chamber is dedicated to the growth of GaAs, but also includes effusion cells for Si, Al, In and Be. The metal growth chamber is an Arsenic-free environment in which the Heusler alloys Fe_3Si and Co_2FeSi, as well as Ge, are grown. After water desorption, the wafers are taken through the the middle chamber to the III-V chamber using the long manipulator arms, in order to grow a high purity and atomically flat GaAs buffer layer on which the subsequent films will grow.

3.1.3 Preparation of the GaAs wafer substrates

The substrates used for the growth experiments are 350 µm-thick 4" wafers of epi-ready semi-insulating, undoped, GaAs(001). The wafers are cut in 4 pieces, as illustrated in Fig. 3.2 (a), in order to fit in the holder designed for the MBE manipulators and stages. When mounting a sample, it is important to keep track of the crystallographic directions of the GaAs piece, which are normally designated by a large ([110]) and a small ([$\bar{1}$10]) "cut" on the sides of the wafer. The quarter circles are placed on a molybdenum wafer holder, shown in Fig. 3.2 (b). The wafer holders are carved with a shape to receive the wafers pieces. A smaller similar

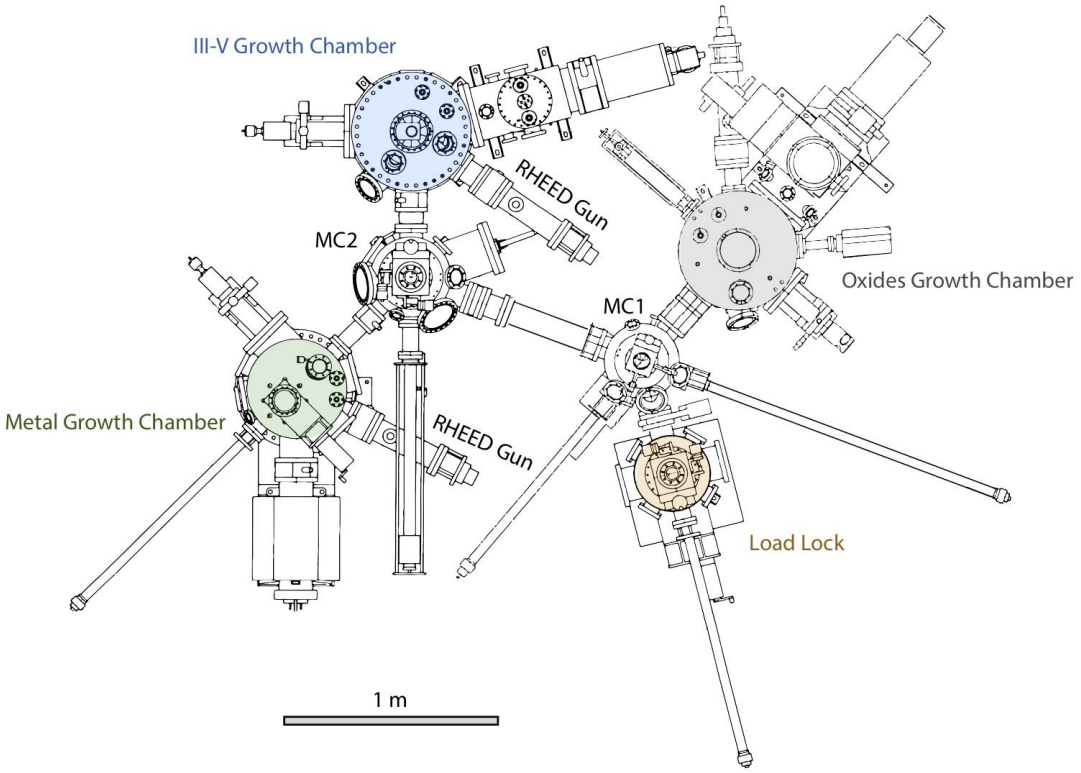

Figure 3.1: Schematic diagram (top view) of the MBE cluster used to grow all samples, including a III-V semiconductor growth chamber (blue) and arsenic-free metal growth chamber (green). The system also contains a third growth chamber dedicated to oxide compounds (grey), not used for this thesis work. The samples are taken in and out of the cluster trough the load lock (orange), and transported to the growth chamber via the middle chamber (MC1 and MC2). The original image was provided by the manufacturer, *CreaTech Fischer & Co. GmbH*.

shape is completely cut out to exposed the back of the wafers to the heat source in the MBE load-lock and growth chambers. The wafer pieces are held in place by a thin tantalum foil (dark grey in the figure), itself fixed by tungsten wires passed through holes and twisted. Mounted samples are inserted in the MBE load-lock and manually affixed to a carousel made to receive the three small pins on the side of the wafer holders. The load-lock is then pumped down, after which the samples are heated up to 300°C for 45 minutes in order to desorb any water molecules from the surface of the wafers and holders.

3.1.4 Reflected high-energy electron diffraction (RHEED)

Samples grown in MBE chamber are monitored *in situ* by reflected high-energy electron diffraction (RHEED). RHEED is an important characterization technique as it gives real time information about the growth mode and surface reconstruction of the samples. An electron gun attached to the growth chamber produces a beam which is focused on the surface of the sample with a small incident angle $\theta \approx 2^\circ$, shown in Fig. 3.3. Some of the electrons diffract on the uppermost atoms of the lattice, interfering constructively and producing a characteristic pat-

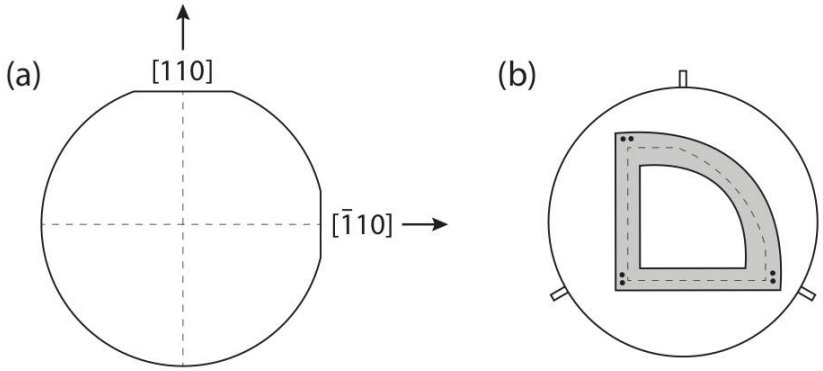

Figure 3.2: (a) Drawing of a GaAs(001) wafer with identified crystallographic directions [110] and [$\bar{1}$10]. (b) Drawing of a wafer holder on which the samples are manipulated inside the MBE system.

tern on a photoluminescent screen detector. Alike diffraction from 3D crystals, the patterns created can be understood as an Ewald's sphere construction. However due to the 2D nature of the RHEED process, the reciprocal lattice of the surface translates into a series of infinite 'rods' instead of points. These patterns can be use to extract quantitative information about the morphological structure of the surface during growth. Oscillations in the intensity of the diffracted electrons hitting the detection screen can also be used to monitor growth dynamics and 'count' the monolayers deposited. Importantly, the alignment of the RHEED patterns of heteroepitaxial films can indicate the relationship between the lattice grown sequentially, i.e. whether the different materials grow pseudomorphically, or if a rotation of the overgrown lattice is required for the structures to be compatible. The electrons used for RHEED characterization in this thesis are submitted to an accelerating voltage of 20 kV, and are produced by emission from a filament sustaining a current of 2 A.

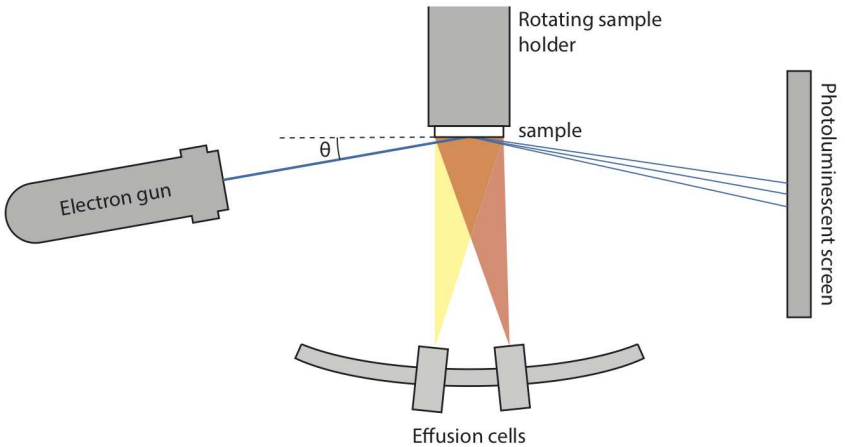

Figure 3.3: Schematic diagram illustrating some of the main components of a MBE growth chamber and RHEED system.

3.2 Thin film characterization

This section will describe some of the most important characterization methods used to investigate the samples grown, once taken out of the MBE system. Central for our investigation, the structure of the crystalline thin films and interfaces between each layers are studied using X-ray diffraction and reflectivity, as well as using transmission electron microscopy. Those techniques will help verify if lattice-matched single crystalline heterostructures with atomically flat interfaces were achieved. The transmission electron microscope can also be used to scan the surface of a sample and produce electron backscatter diffraction images, useful to determine the orientation of domains in a polycrystalline material. The surface of the samples is assessed by atomic force microscopy, measuring roughness and revealing the presence of islands, steps, and other topographic features. Lastly, SQUID magnetometry is employed to study the magnetic behaviour of the films and heterostructures. Relating to the overarching goal of creating a SS-SBTT, the objective is to measure independent magnetization of the two FM films of a trilayer, indicating that the intermediate buffer layer is effectively decoupling them and acting as a barrier for transported electrons.

3.2.1 X-ray diffraction and reflectivity (XRD/XRR)

X-ray diffraction is a technique which provides useful information about the structure of crystalline materials. The XRD system used throughout this work is an X-Pert PRO MRD^{TM} with CuKα_1 radiation source which yields as wavelength λ=1.54056 Å. Inside the XRD machine, samples are mounted with double-sided tape on a goniometer, an electromechanical stage which can rotate precisely in 3D space and introduce the sample in the path of the collimated monochromatic X-ray beam. Upon hitting the surface of a sample, incident X-rays scatter elastically in various directions, producing a diffraction pattern which reveals regularly spaced reflections portraying a specific crystal structure. The diffraction from X-rays on a lattice can be understood, in a semiclassical picture, by representing the atoms as being arranged into families of discrete parallel planes, which create conditions for constructive or destructive interference as the incident angle is swept. This interpretation is linked to Bragg's law, named after father and son William Henry and Lawrence Bragg by whom it was first suggested in 1913.[83] Bragg diffraction conditions are satisfied when this equation holds:

$$2d \sin\theta = n\lambda \tag{3.1}$$

where d is the lattice spacing, θ is the incident angle with respect to the planes, and lambda is the X-ray wavelength, as illustrated in Fig. 3.4 (a). Changing θ will result in different phases in the outcoming beams depending on the spacing d, modulating the intensity of the diffracted signal. In a typical diffraction experiment, the setup is as illustrated in Fig. 3.4 (b), where the X-ray source is held fixed while the sample is rotated by ω and the detector by 2θ. This experiment is referred to as an "$\omega - 2\theta$ scan". The exact intensity of the peaks associated to

each of the lattice planes depend on the structure factor (F_{hkl}), which takes into consideration possible systematic extinctions which originate from specific Bravais lattices and bases.

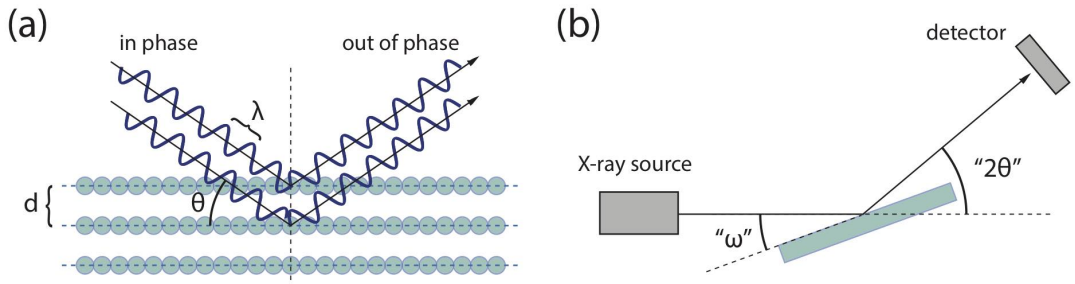

Figure 3.4: (a) Illustration of Bragg's law, where the incident beam hits the surface of a sample with angle θ. The relationship between the lattice spacing d and wavelength λ determines conditions for constructive and destructive interference. (b) XRD setup where a typical measurement consists of an "$\omega - 2\theta$" scan.

The "$\omega - 2\theta$" scans are usually performed over ω between 12°and 38°, as this range contains the two first –and strongest– reflections for the GaAs substrate, the (002) at $\omega = 16.514°$ and (004) at $\omega = 33.028°$.[84] The data points are taken in steps of 0.003° each measurement averaging the photon counts for 2-3 seconds, which yields a scan of a about 5 hours (those parameters can be changed in order to reduce noise and reveal finer features).

The other materials investigated in this thesis, Fe_3Si, Ge, Co_2FeSi, and later $FeGe_2$, have structures that are lattice matched to the GaAs substrate, meaning that their reflections should coincide with those of GaAs (this is different for $FeGe_2$, as will be explained in the Results chapter). Nonetheless, X-ray diffraction performed on thin films (<100 nm) give rise to an effect called "finite thickness oscillations". Indeed, as in Bragg's conditions for coherent scattering, the thickness of a thin film can itself consist in a plane, delimited by its interface with the underlying layer. The film then acts in a way analogous to a Fabry-Pérot interferometer. An elegant way to understand the pattern produced for a thin film is to see the diffraction as effectively taking the Fourier transform of a "square pulse" with width corresponding to the film's thickness. The result is a sync function (sync square for detected intensity) with oscillations related to the inverse of the thickness. For the GaAs substrate, the width can be considered infinite, in which case the reflection peaks converge towards delta functions.

X-ray reflectivity (XRR) is also employed as a mostly surface-sensitive measurement. The method consists in performing an $\omega - 2\theta$ scan, however for a range of small grazing angles, usually for ω = 2 to 6°, such as to collect the photons specularly reflected from the surface. Roughness and irregularities on the surface of the sample will translate into a deviation in the intensity of the X-rays detected compared to the ideal case described by Fresnel's law. For multilayer thin film stacks, XRR will also show oscillations with period related to the film thickness and amplitude to the interlayer roughness. The setup is similar to the XRD shown in Fig. 3.4 (b), however the detector and alignment of the machine have to be modified such as to accommodate the required small ω scan.

3.2.2 Transmission electron microscopy (TEM)

Generally speaking, TEM is a method in which a focused electron beam is passed through a thin sample in order to produce an image. A transmission electron microscope can be used in a wide variety measurements modes, each providing different information about a specimen. Electron scattering remains central to the ensemble of techniques. The resolution made possible by using electrons instead of visible light is orders of magnitude greater, owing to the wavelike nature of electrons with de Broglie wavelength in the picometers range. Indeed, a TEM with an accelerating voltage of 200 kV yields electrons having kinetic energy $E_k \sim 200$ keV. With a rest mass $m_e = 0.511$ MeV$/c^2$, the de Broglie wavelength can be calculated as follows:

$$\lambda = \frac{h}{\sqrt{2 \cdot m_e \cdot E_k}} = \frac{h}{\sqrt{2 \cdot 0.511 \frac{\text{MeV}}{\text{c}^2} \cdot 200 \text{ keV}}} \approx 2.7 \text{ pm} \tag{3.2}$$

where h is Planck's constant. Such wavelengths are sufficiently small to observe individual atoms within a lattice, uncovering far-reaching information regarding the structure of the layer stacks grown by MBE.

The preparation of TEM specimens is a sensitive task accomplished by trained scientists, consisting in mechanically lapping a piece of wafer along a specific crystallographic plane into a fine lamella, which is then polished and treated by Ar ion milling. The majority of images that will be presented in the following chapters were collected by Dr. B. Jenichen, using scanning TEM (STEM) high-angle annular dark-field imaging (HAADF), unless indicated otherwise, with a TEM JEOL ARM200. HAADF uses an annular detector to collect only electrons scattered from the specimen at high angles, which is well suited to resolve elements with large atomic number (Z). The stronger electrostatic interactions between the nucleus and the beam in high Z elements increases the number of high-angle scattering events, making them appear brighter in the images created. The contrast in these images can be reliably used to locate and identify atoms within a crystalline lattice.

Many TEM systems also offer the possibility to produce selected area electron diffraction (SAD) patterns. The sample being prepared into very thin lamellas (tens of nanometers), the high-energy electrons can easily pass through. The wavelength of these electrons is small enough for the atomic lattice to work as a diffraction grading. The resulting pattern is therefore a series of spots, each of them satisfying a given diffraction condition, which can be associated with Miller indices and lattice planes.

Another important measurement technique which provides information about the crystalline films is electron backscatter diffraction (EBSD). For these measurement, the samples are investigated using a Zeiss ULTRA 55 scanning electron microscope, with the stage tilted to a high angle with respect to the beam. As the electrons hit the surface of the sample, some may backscatter and escape. The direction of the backscattering events is related to the Bragg diffraction conditions, and the pattern created on the detector screen can be related to the spacing and orientation of the sample's lattice planes. A 2D map of the of the sample surface can thus be reconstructed, revealing the orientation of domains in polycrystalline materials.

3.2.3 Atomic force microscopy (AFM)

AFM is a surface characterization method providing sub-nm resolution information about the roughness of a sample. The surface is probed by an oscillating cantilever, at the end of which an atomically sharp tip scans the surface of a sample. The strength of the interaction between the top layer atoms of the sample and the tip create perturbations in the cantilever's oscillations, which can be converted into variations of the sample's relief. In other words, the images extracted from an AFM measurement are analogous to topographic maps. A useful quantity to extract from such measurements is the "root mean square" (rms) roughness (R_{rms}) of a sample, which is essentially a 2D averaging of the atomic hills and valleys over the surface scanned. In some cases, AFM can reveal the presence of islands or quasi-3D droplets formed on the surface. Those should be avoided considering the heterostructures sought-after in this research.

MBE growth conditions can have drastic effects on the surface topography of a sample, which is important when attempting to grow atomically flat heterostructures. AFM is therefore an powerful tool to investigate the quality of the thin film stacks, especially along the steps required to optimize the solid-phase epitaxy approach we wish to develop in this thesis. Ideally, the roughness should be kept as low as possible (below 1 nm rms). The AFM system used to measure the samples presented in this thesis is a Dimension Edge^{TM} from Bruker.

3.2.4 SQUID magnetometry

A Quantum Design MPMS® superconducting quantum interference device (SQUID) is used to obtain the magnetization of the samples. As an external magnetic field is applied along a specific orientation of the sample, the SQUID measures the magnitude of the sample's magnetization. For spintronics applications, and in the context of this research, it is essential to obtain quantitative information about the magnetic polarization of the materials under study, as well as the effects that come into play once those are combined into heterostructures. SQUIDs are sensitive magnetometer able to detect extremely weak magnetic fields by taking advantage of superconducting loops made of Josephson junctions (JJ). In a JJ, a superconducting current of Cooper pairs tunnels through a barrier without requiring an applied voltage (Josephson effect). A loop can be constructed in which two JJs are inserted, as shown in Fig. 3.5 (a), where a current I splits into two equal parts I_a and I_b. When magnetic field Φ appears through the loop, an applied screening current I_s produces an equal counteracting magnetic field. The current I_s adds up in opposite directions in the loop, which translates into a readable voltage proportional to Φ.

The samples are not directly interacting with the SQUID superconducting loop. Instead, they are inserted through an arrangement of four coils as shown in Fig. 3.5 (b), themselves within the solenoid which applies the external (static) magnetic field. Two of the loops have the current flowing clockwise, while the others are counterclockwise, to cancel out the effect of the applied static field. The magnetized samples are oscillated through the four loops, producing a current which is routed to the SQUID by another coil, shielded from the applied field

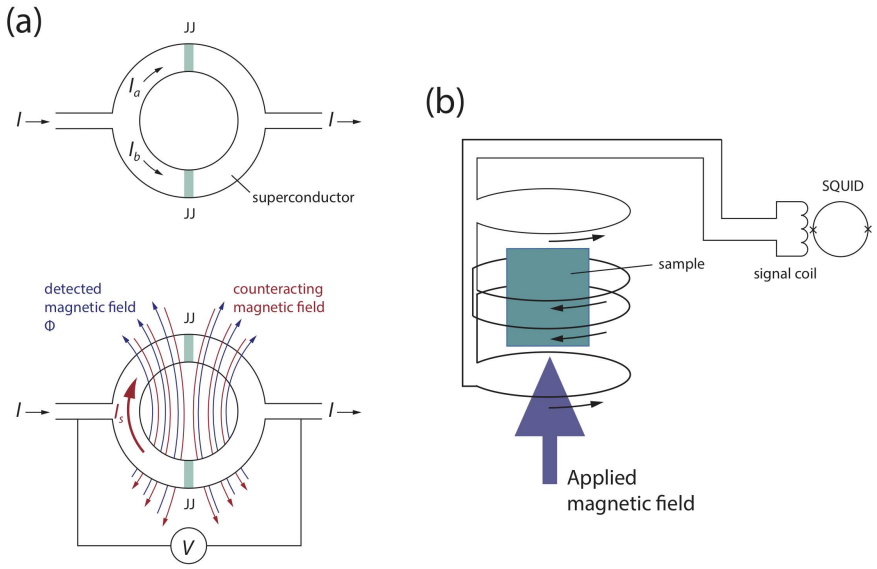

Figure 3.5: (a) Superconducting loop inside a SQUID magnetometer. (b) Four coils which pick up the current building up as the magnetized sample is moved up and down and transferred to the SQUID superconducting loop.

(the full circuit diagram is more involved[85]). The magnetization of the sample is measured by averaging the voltage applied to the superconducting SQUID loop over several periods.

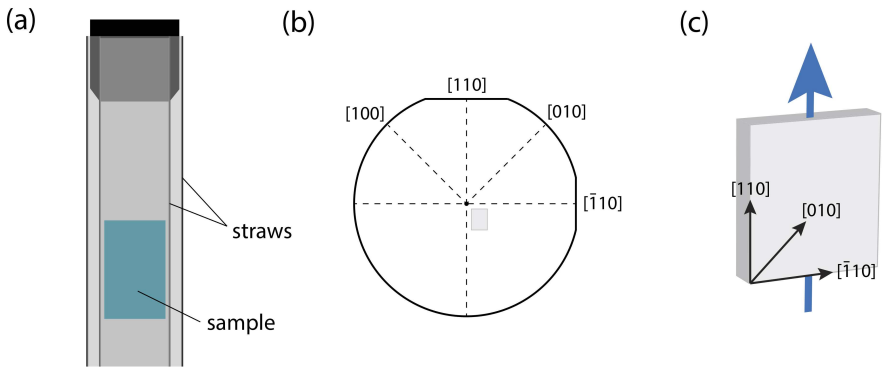

Figure 3.6: (a) Sample as inserted in the SQUID system held between two polyethylene straws. (b) GaAs wafer diagram with main and secondary cuts indicating the [110] and [$\bar{1}$10] planes. (c) Sketch of a sample as measured in the SQUID magnetometer, measuring magnetization in the [110] direction (parallel to the [$\bar{1}$10] planes).

The SQUID system can operate at temperatures ranging from 4 to 300 K. However, the superconducting elements need cryogenics in order to function. The SQUID system has an insulating jacket which must be filled with liquid nitrogen (LN2). An internal reservoir is then filled with liquid helium. Samples are inserted and held within two interlocked polyethylene straws, with diameter fitting to an adapter on the insert rod, shown in Fig. 3.6 (a). Care must be taken when preparing the samples to keep track of the orientation of the pieces taken from

the wafers. The convention is to measure a given sample along three crystallographic orientations: [110], [$\bar{1}$10], and [010], shown in Fig. 3.6 (b) and exemplified in (c). The measurements are designed and controlled via the dedicated *MPMS MultiVu* software. Magnetization hysteresis loops are usually measurements from +5000 Oe to -5000 Oe, with increasing resolution as the field approaches 0, since the coercivity of the thin films studied is on the order of a few Oe. (1 Oe = 79.58 A/m, representing magnetic field strength H. As a comparison, 1 T of magnetic flux density in vacuum is equivalent to 795 775 A/m, using $H = B/\mu_B$.) The SQUID expresses the magnetic moment m of the sample, per convention, in electromagnetic units (emu), which are A·m^2. The magnetization M corresponds to emu/m^3, or magnetic moment per volume m/V. Since not all wafer pieces are cut with the same dimensions, it is convenient to normalize all measurements to the saturation magnetization, in order to better compare the samples together.

3.3 Transport experiments

3.3.1 2-, 3- and 4-terminal resistance measurements

Electrical transport measurements are essential in order to learn about the properties of the thin films and heterostructures created throughout this project. In the simplest case, the resistance of a thin film can be measured by applying a voltage across the sample and measuring the resulting current. The resistance is then given by Ohm's relation $R = V/I$. By modifying the sample's geometry (such as its contact configuration, thickness) as well as the environment in which the sample is measured (temperature, alignment of an external magnetic field), a rich set of parameters can be extracted, and relevant physical effects can be revealed.

When measuring the resistance of a sample using Ohm's relation, at least two contacts must be made on the sample itself. This 2-terminal approach has limitations, since the contacts themselves have a resistance that must be added in series with that of the sample in the measurement circuit, as shown in Fig. 3.7 (a). In samples sufficiently large, the lead resistance remains negligible and 2-terminal probe measurements can be used reliably. However, for nanoscopic structures in which the signals of interest are expected to be small, the parasitic contact resistance can be pronounced. This effect is especially problematic when measuring a semiconducting sample since, as we know, metal-semiconductor junctions give rise to Schottky barriers with temperature-dependent rectifying I-V signature (see equation 2.3), drastically complicating the interpretation of the measurements.

Those limitations can be circumvented by using, instead, a 4-terminal probe measurement set-up as shown in Fig. 3.7 (b). In this configuration, voltage is sensed via an additional pair of contacts. The voltage measured within the sample therefore does not include the voltage drop that occurs through the current source contacts, which provides a more accurate reading. A 4-terminal sensing approach is therefore desirable to study transport in semiconductor thin films and materials having a small resistivity. One should note that a hybrid 3-terminal configuration is also possible, in which case a single contact is used twice for current sourcing

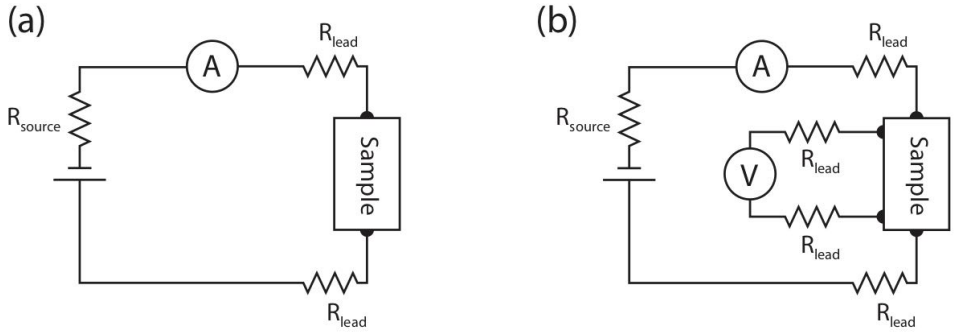

Figure 3.7: (a) 2-terminal I-V measurement circuit diagram. The potential across the sample is set from a voltage source, and current is measurement using an ammeter. (b) 4-terminal measurement circuit diagram, in which case the lead resistance is eliminated. A potential is applied via a voltage source, while both a voltmeter and ammeter measure the voltage drop and current across the sample using different sets of contacts.

and voltage readout. This approach offers more reliable measurements as the 2-terminal one, and can prove useful when a sample imposes geometric limitations.

3.3.2 Vertical spin valves

To investigate the possibility to operate the SS-SBTT as previously described, the FM/SC/FM trilayers should first be used to create vertical spin valves (to be distinguished from lateral spin valves). The objective of the devices is to measure the TMR while having the FM electrodes aligned along different magnetization directions, hence revealing the spin valve effect described in the previous chapter. For this purpose, only the two FM electrodes are contacted, allowing for 2- or 3-terminal measurements. (Contacting and modulating the SC tunnel barrier itself is not required nor attempted for the spin valve investigation, and would represent another fabrication challenge.) As an external magnetic field is then swept, the different coercivity of the two FM films should, if the devices work as intended, generate high resistance plateaus corresponding to an antiparallel magnetization state.

The mask used to pattern the trilayer stacks and the resulting spin valve structure are shown in Fig. 3.8, taking as example a $Fe_3Si/FeGe_2/Co_2FeSi$ trilayer. Each mask created contains an array of 36 'devices' (not shown in figure), and each device is designed to offer the possibility to test six different vertical spin valves, as depicted in (a). Increasing the number of spin valves per device can save a significant amount of measuring time, especially when the experiments are conducted at low temperature in a cryostat. This way, a single cooldown offers the possibility to perform multiple experiments, while minimizing the risk associated with the eventuality of faulty contacts and leakage.

The effective spin valve surface area is a $1 \times 1\mu m^2$ square, circled in (b) at the intersection between the underlying Fe_3Si film and AuTi contact lead. A closer view is provided in (c), where the spin valve area is indicated by a green square. The reason to reduce the size of the

spin valve to a minimum (1 µm being the lower limit for photolithography) is to minimize the chances of leakage current through defects in the $FeGe_2$ buffer layer.

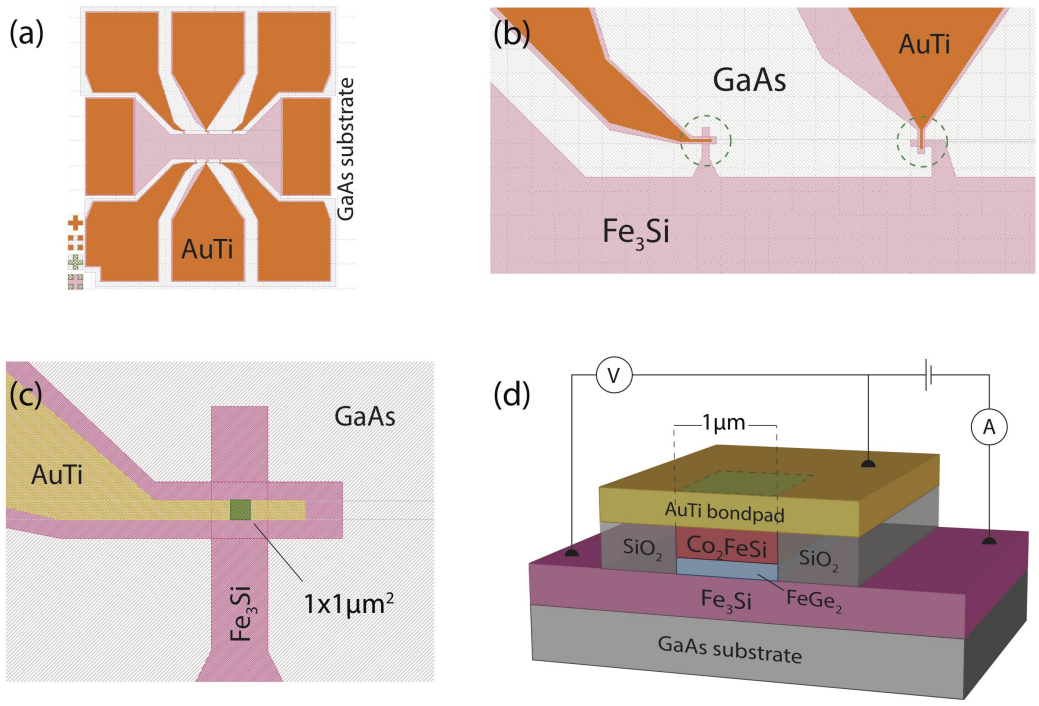

Figure 3.8: (a) Large view of the mask used to create in total six spin valve devices. All three layers are etched, except for a 1×1 µm^2 square at the intersections (green is next figures). The underlying Fe_3Si layer is preserved over the pink-colored area. The whole surface is coated in SiO_2, over which AuTi contact leads are then deposited (orange). (b) Closer view showing how the contact pads overlap the films for two spin valve devices. (c) Selected section of the mask around a single spin valve showing the effective 1×1 µm^2 area of a spin valve, where the original three layers remain (green). (d) Schematic diagram showing a 3D cross-section and the structure of a spin valve, with 3-terminal measurement circuit diagram.

The first step of the fabrication is to etch the three epitaxial layers in order to expose the semi-insulating GaAs substrate outside the pink area of the mask. The two uppermost $FeGe_2/Co_2FeSi$ layers are then selectively etched from the pink area, *except* for the 1×1µm^2 square shown in (c). The whole surface is afterwards covered by an insulating SiO_2 film such as to match the thickness removed with the $FeGe_2/Co_2FeSi$ films (typically 6+12 nm). After lifting the remaining resist from the spin valve square area, AuTi contact leads are evaporated over the SiO_2 (drawn in orange), which will come in contact only with the top Co_2FeSi electrode. A cross-section of the resulting structure is shown in (d). This device allows for 2- or 3-terminal measurements, as illustrated by the circuit diagram superimposed. As a current is passed form the Fe_3Si to the Co_2FeSi electrodes through the $FeGe_2$ buffer layer, the voltage is measured from another contact on the Fe_3Si to the same contact to the Co_2FeSi. The Fe_3Si and Co_2FeSi films having different thicknesses and coercivity should allow for their magnetization to be controlled independently while applying small in-plane magnetic fields.

3.3.3 Sheet resistance

The resistance of films being only a few nanometers thin can (and should) be treated differently than the resistance of bulk materials. Normally, the resistance is a bulk piece of material is expressed in terms of the material's resistivity ρ and the sample's physical dimensions (length (L), width (w), thickness (t)) such that $R = \rho L/(wt)$. For two dimensional films with uniform thickness, it is however useful to combine the resistivity and thickness together in a quantity called the sheet resistance R_s such that the sample's resistance is

$$R = \frac{\rho}{t}\frac{L}{w} = R_s\frac{L}{w}. \tag{3.3}$$

The units of the sheet resistance are Ω/sq, or 'Ohms per square', which is equivalent to Ohms, however exclusively used to denote R_s. Conveniently, if the film thickness is known, the film's resistivity can be directly retrieved as

$$\rho = R_s t. \tag{3.4}$$

The sheet resistance is useful because it is independent form the film's contacts and dimensions, and can be measured directly via 4-terminal sensing using the Van der Pauw method.[86] In the latter, four contacts (1,2,3,4) are made at the extremities of a piece of sample. A current I_{12} is applied between contact 1 and 2, while the voltage V_{34} is measured across contacts 3 and 4. The normal resistance is therefore obtained using Ohm's law: $R_{12,34} = V_{34}/I_{12}$. A similar measurement is also done perpendicular to the first one, which yields a second resistance $R_{23,41}$. The sheet resistance R_s must then be solved for (numerically) using the expression

$$e^{-\pi R_{12,34}/R_s} + e^{-\pi R_{23,41}/R_s} = 1. \tag{3.5}$$

The sheet resistance of samples can be calculated directly in a dedicated Hall measurement setup available in the lab. The system is equipped with a magnet and can perform standard Hall characterization field sweeps, as well as 4-terminal measurements along various sample orientations. This system can be used to extract other useful information about thin film samples, such as the carrier type, 2D density and mobility.

3.3.4 Hall effects

Measuring the Hall effect in thin films adds a completely new dimension to the set properties available for study, as it reveals how charge carriers respond to the Lorentz force resulting from the application of an external magnetic field. In the classical Hall regime, the Lorentz force $F_B = e(\mathbf{v} \times \mathbf{B})$ relates the torque exerted on carriers with charge e to their velocity $\mathbf{v}$ and magnetic field vector $\mathbf{B}$. For a magnetic field vector strictly perpendicular to the flow of current, the lateral drift of charges creates an accumulation on one side of the sample, which translates into a compensating electrostatic force $evB = F_e = eV_H/w$, where w is the width of the sample and V_H the so called Hall voltage. Expressing the current through the sample

as $I = NevA$, where N is the electron density and A the sample's cross-section area, we can retrieve the Hall voltage expressed

$$V_H = \frac{wIB}{eNA} = \frac{IB}{ne} \tag{3.6}$$

where n is the planar electron density ($n = NA/w$). Using Ohm's Law and equation 3.6 yields the Hall resistance, simply written as

$$R_H = \frac{B}{ne}. \tag{3.7}$$

In semiconductor samples, the conduction mechanisms can be dominated either by electrons or holes, each having different densities and mobilities. The equation for R_H can be generalized in the following way to account for both contributions:

$$R_H = \frac{N_h\mu_h^2 - N_e\mu_e^2}{e(N_h\mu_h + N_e\mu_e)^2} \tag{3.8}$$

where μ_h and μ_e are the carrier mobilities for holes and electrons, while N_h and N_e the respective carrier densities.[87] This relation can be useful to characterize an thin piece of semiconducting material. In the most basic case, the sign of the Hall voltage will determine the type of the majority charge carriers in an extrinsic semiconductor.

An important aspect which should not be neglected is that the materials investigated in this thesis are ferromagnetic, which drastically modifies the interpretation of the Hall measurements performed on our samples. Indeed, magnetoresistive effects in ferromagnetic materials must be understood in terms of the anomalous Hall effect (AHE), in which a combination of magnetic polarization and spin-orbit coupling produces a finite Hall voltage even *without* the presence of an external magnetic field.[88] It is relevant at this point to introduce the so-called Planar Hall Effect (PHE). The PHE, related to the anisotropic magnetoresistance (AMR), generally describes the relationship between resistance and the orientation of the sample's magnetization relative to the current direction. The microscopic origin of the AHE in real materials is tedious to analyze, since it can appear from a number of effects. Two explanations arise from scattering events, called "side-jump" and "skew scattering". An "intrinsic deflection" can also occur from the topological properties of a material, related to the electrons' Berry phase curvature.[89] The details of these effects will not be explored in this thesis.

Nonetheless, the behavior of the Hall resistance while changing the in-plane magnetization M of ferromagnetic thin films can illustrate the presence of magnetism in a new way, and provides an additional approach to investigate magnetic hysteresis and anisotropy. The relationship between the Hall voltage V_H and magnetization orientation of a ferromagnetic sample was derived by K. Okamoto.[90] The expression, which encompasses both the conventional Hall effect and PHE, is as follows:

$$V_H = R_s\frac{MI}{d}\cos(\theta) + k\frac{M^2I}{d}\sin^2(\theta)\sin(2\phi) \tag{3.9}$$

where M represents the magnetization of the material, θ is the angle between M and the z-axis, ϕ the angle between M and the current I, R_s a coefficient related to the normal Hall effect, d the sample thickness and k another constant factor. A schematic diagram illustrating the angles and magnetization vector is shown in Fig. 3.9.

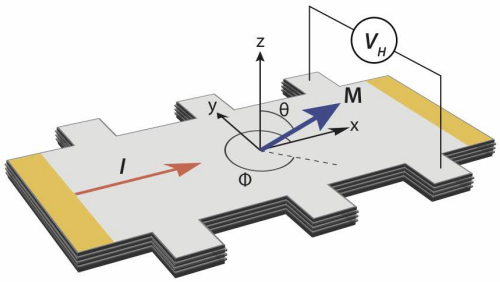

Figure 3.9: Diagram showing the generalization the Hall effect when considering the magnetization (M) of the sample being along an arbitrary orientation with respect to the applied current (I). The normal Hall effect is retrieved when $\theta = 0$ and the magnetization component is uniquely along the z axis. For $theta = 90°$, the system is in the planar Hall regime, in which case only the angle ϕ is relevant.

To perform Hall measurements, the samples are usually prepared such as to have a so-called *Hall bar* geometry, where a rectangular 'bar' is garnished with sets of lateral contacts. Fabricating mesoscopic Hall bars (in the micrometer range) can help reduce the contribution from defects and impurity, especially when studying thin epitaxial films. The Hall bars are patterned on the samples by a combination of photolithography, etching and metal evaporation using the mask shown in Fig. 3.10. First, a thin layer of photoresist is applied on the surface of the wafer piece by spin coating. The area surrounding the Hall bar is then exposed, developed, and chemically etched, leaving the central structure shown in Fig. 3.10 (b). The Hall bar is then contacted by evaporating metallic contacts and bonding pads, as shown. In total, eight contacts are made, which can serve to apply current and measure voltage drop across different parts of the sample simultaneously. Once patterned, the Hall bar samples are mounted on an 8-pin chip holder and contacted via gold wire bonding.

3.3.5 Cryostats

The spin valve and Hall bar samples can be measured in different two cryostats systems. One is a tabletop'optical' cryostat from *Oxford Instruments plc* with effective minimum temperature of about 5 K, illustrated in Fig. 3.11. This smaller device can be filled either with liquid nitrogen or liquid helium. It is therefore a useful versatile tool to test samples under various conditions. The temperature of the samples is monitored by an *Oxford Instruments* ITC 4 temperature controller system, with can heat the holder and sample space. It is equipped with two oil-cooled coils powered by a *Kepco* bipolar operational power supply able to provide 7 A, which can together generate magnetic fields $\mu_0 H = 20mT$ at the sample's position. The insert and sample holder can be rotated manually, which allows to orient the sample arbitrarily with respect to the external magnetic field (only along one axis).

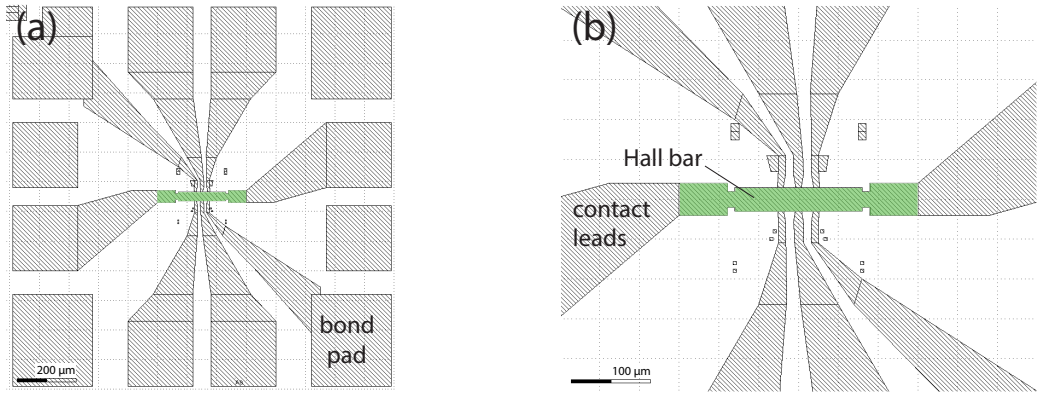

Figure 3.10: (a) Lithographic mask used to fabricate the Hall bars, with bond pads and leads connecting to the central mesa. (b) Closer view of the mask showing the details of the Hall bar section. A total of 8 contacts are made on the effective Hall bar surface area. The width is 30 µm and length between the most distanced lateral contacts is 40 µm.

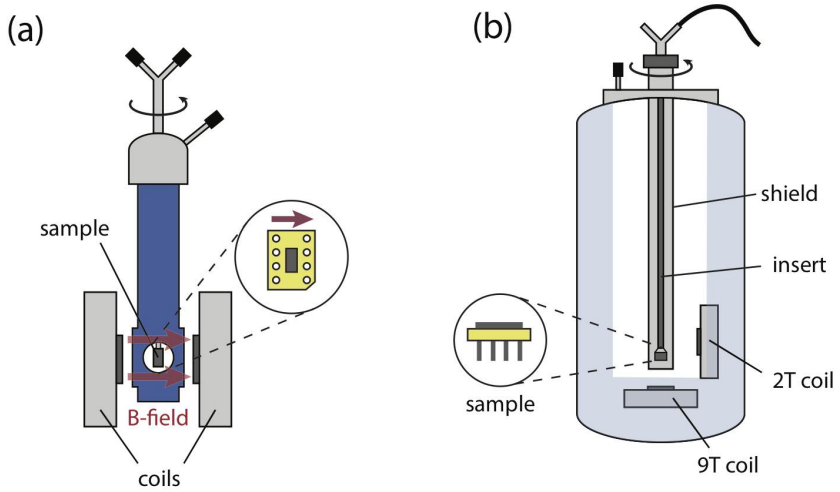

Figure 3.11: (a) *Oxford Instruments* tabletop cryostat. The sample is visible through a glass porthole, which allows for visual confirmation of the alignment with the magnetic coils. The sample is held vertically on the insert. (b) *Attocube* cryostat diagram, showing the position of the two independent superconducting coils with the respect to the sample, held horizontally at the bottom of the insert.

The second cryostat is an Attocube liquid Helium system (attoLIQUID series) equipped with two perpendicular superconducting coils and base temperature of 4 K. The presence of two coils is useful since magnetic fields can be applied in and out of plane. The possibility to rotate the insert itself offers the possibility to subject the samples to any field orientation in three dimensions. The sample is held horizontally in the insert tube (facing up), perpendicular to the large 9 teslas magnet placed at the bottom of the cryostat as illustrated in Fig. 3.11 (b), which can be used for Hall measurements. The in-plane magnet is smaller and can generate fields up to 2 teslas. Both superconducting coils are controlled by *Oxford Instruments* IPS 120

power supplies. The temperature is monitored using a *LakeShore 332* cryogenic temperature controller.

The experiments in both cryostats are controlled via a Python-based graphical user interface (LabGUI), which executes user-defined scripts communicating with the instruments involved in each measurements. Currents are applied using a Keithley 6221 DC and AC current source. A Stanford Research System SRS830 DSP lock-in amplifier is also available to apply (AC) and measure voltage. DC voltages are also measured using a Keithley 2182 nanovoltmeter.

4 Growth and Characterization of vertical FM/SC/FM Spin Valves

This chapter is dedicated to the research accomplished in order to realize and characterize lattice-matched hybrid FM/SC/FM trilayers. This step, certainly essential to the creation of a spin-selective Schottky barrier tunnel transistor (SS-SBTT), is a fundamental growth challenge which has been tackled in the past using a number of approaches, each reaching low to moderate degrees of success. As explained earlier, the difficulty lies in growing a SC layer over a FM layer by MBE due to the incompatible crystallization energies between the two types of materials. The direct growth by MBE of a semiconductor over a metallic surface will inevitably generate intermixing and degradation of the FM/SC interface, which in turn would prevent efficient spin tunneling through the emerging interfacial Schottky barrier. The pivotal solution investigated here, and central experimental innovation presented in this thesis, is to use a combination of MBE and solid-phase epitaxy (SPE), whereby a thin amorphous film of Ge is annealed slowly over Fe_3Si.

The development of the SPE method will be described in details, with accompanying results taken along the optimization of the annealing process. The approach consists in depositing an amorphous layer of Ge at a temperature low enough to remain in a 'safe range', where the bonds of Fe_3Si are less likely to dissociate. The amorphous Ge is then crystallized by annealing, with hopes of achieving minimal intermixing with the underlying metallic surface. The optimization of the SPE approach was guided by an in-depth investigation of the the structural properties of the thin film stacks by XRD, TEM, and AFM. The outcome of this SPE approach was first published in 2017, where the successful growth of lattice-matched trilayer stacks were reported.[91] The method was then extended to combinations involving both Fe_3Si and Co_2FeSi, in which case high quality hybrid trilayers could as well be obtained.[92] An important part in the investigation of the samples is to understand the magnetic properties of each films forming the trilayer stacks. Indeed, the functioning of the proposed SS-SBTT requires the SC tunnel junction to magnetically decouple of the two FM contacts. Furthermore, heterojunctions of ultra-thin FM metals and semiconductors can host various surface effects and coupling, whose investigation is primordial to assess the feasibility of our device concept. This part of the study was conducted by SQUID magnetometry.

An unexpected outcome of the SPE approach was the synthesis of a new layered polymorph of $FeGe_2$, whose structure will be discussed here as required to provide a full depiction of the trilayers that were obtained. The original idea behind the SPE approach was to prevent any reaction of the Ge with the metallic substrate. Instead, the annealing of amor-

phous Ge triggered a highly reproducible intermixing mechanism with the underlying Fe and Si atoms, resulting quite remarkably in a lattice-matched compound preserving the integrity of the Fe_3Si interface. The lattice-matched trilayers obtained by MBE and SPE are therefore $Fe_3Si/FeGe_2/Fe_3Si$. The SPE of Ge over Co_2FeSi results in a different crystalline Ge-rich compound, which nonetheless preserves the fully crystalline pseudomorphic growth relationship of the layer stacks. Although the creation of $FeGe_2$ might raise questions regarding the success of the SPE approach to grow a semiconductor (Ge) over a metal, this surprising result does not exclude the possibility to operate the heterojunctions as originally intended. Further details about the properties of $FeGe_2$ will be examined in the next chapter.

Lastly, this chapter will present and discuss vertical spin-valve measurements performed using $Fe_3Si/FeGe_2/Fe_3Si$ and $Fe_3Si/FeGe_2/Co_2FeSi$ trilayers at low and room temperature. Going back to our original goal to use the FM/SC/FM trilayers as a building block for a spin-selective transistor, the samples were processed into spin-valves using photolithography, with contacts made on each of the FM films. This configuration allowed to investigate spin injection mechanisms. The spin-valve signals measured establish the trilayers as a promising candidate to realize a SS-SBTT.

4.1 MBE and optimization of SPE parameters

4.1.1 Sample preparation and GaAs buffer layer

Once the GaAs(001) substrates are inserted inside the MBE system, they are first brought to the III-V growth chamber. In the III-V growth chamber, the holders are reoriented and held facing down, towards the effusion cells containing elemental Ga and As, and slowly rotated. The substrates first are heated rapidly (20°C/min) to 500°C, and then slowly (10°C/min) up to 580°C in order to evaporate the thin oxide layer applied by the manufacturer to shield the GaAs surface against contamination. As the temperature rises, the RHEED beam is aligned on the surface of the substrate. The slow appearance of a GaAs RHEED pattern confirms the evaporation of the amorphous oxide film. The sample are then brought back to 540°C, the growth temperature of GaAs in the system. Always while rotating the samples, the As shutter is opened, with a crucible temperature of 420°C ensuring an As-rich environment. The 'hot lip' of the As cell is independently kept at a higher temperature (600°C) to avoid condensation and shutter blockage. The Ga (with temperature 945°C, hot lip 995°C) shutter is then sequentially opened and closed 10 times, a method which traps impurities in the first monolayers of the film. After this step, the Ga shutter is left opened for 45 min, which results in a buffer layer of 350 nm. The growth sequence is summarized in Table 4.1.

Once the deposition is completed, the Ga shutter is closed and the temperature is brought down to 200°C. The As shutter is left opened down to 300°C to ensure that the surface of the fresh GaAs buffer layer is As-terminated with a (2×1) reconstruction.[32] The typical RHEED images corresponding to the [010] and [110] azimuths are shown in Fig. 4.1. The images are taken by a CCD camera focused on the (round) photoluminescent screen and connected to a

Time	Thickness	Material	
15 sec.	2.8 nm	GaAs	} 10x
45 sec.	-	As	
45 min.	350 nm	GaAs	

Table 4.1: Growth sequence of the GaAs buffer layer. The first two steps are repeated 10 times.

software dedicated to RHEED analysis (SAFIRE). As can be seen in the RHEED photographs, the presence of a high number of streaks and so-called Kikuchi lines confirms that the GaAs buffer layer is extremely flat with ideal crystallinity and reconstruction.

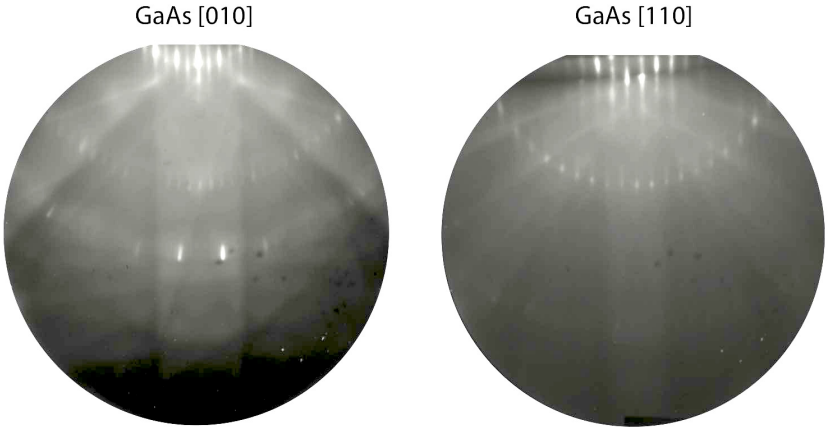

Figure 4.1: RHEED image of the GaAs surface after growth, showing the two principal patterns along the [010] and [110] directions. The diagonal Kikuchi lines indicate a very flat surface.

Growth of Fe_3Si and Co_2FeSi

After growing the GaAs buffer layer, samples from the III-V chamber are transferred into the metal growth chamber, where a first layer of the Heusler alloys Fe_3Si and/or Co_2FeSi is grown. The optimal growth parameters for both materials were determined after a series of investigations conducted throughout the last two decades.[32,48,55] Fe_3Si and Co_2FeSi are grown with substrate temperature of 200°C. For Fe_3Si, the cell temperatures are T_{Fe}=1325°C and T_{Si}=1365°C. These settings yield a growth rate of 16 nm/h, with ideal atomically sharp interface with the GaAs(001) substrate. Co_2FeSi requires cell temperatures T_{Co}=1420°C, T_{Fe}= 1242°C, and T_{Si}=1320°C, which translates into the same growth rate. These settings are optimized to produce the $L2_1$ ordering (theorized to exhibit a half-metallic character) for the Co_2FeSi, and DO_3 structure for Fe_3Si. One should note that the temperatures quoted above will inevitably vary from a MBE system to another, and even sometimes need to be adjusted within our own system. The fundamental parameter to respect in order to obtain the right

stoichiometry is the atomic *flux* and ratios between the Fe, Co and Si cells for the different compounds.

Typical XRD curves corresponding to the two Heusler alloys are shown in Fig. 4.2, used as reference. In (a), the sample is GaAs/Fe_3Si (36 nm), while in (b) GaAs/Co_2FeSi (36 nm). The GaAs(002) is clearly visible in both cases, with superimposed oscillating functions with periods confirming the thickness of the layers (analyzed using the X'Pert Epitaxy program). Both films indeed appear lattice-matched with the GaAs substrate. The visible finite thickness oscillations further indicate that the interface with GaAs is smooth over large areas of the samples.

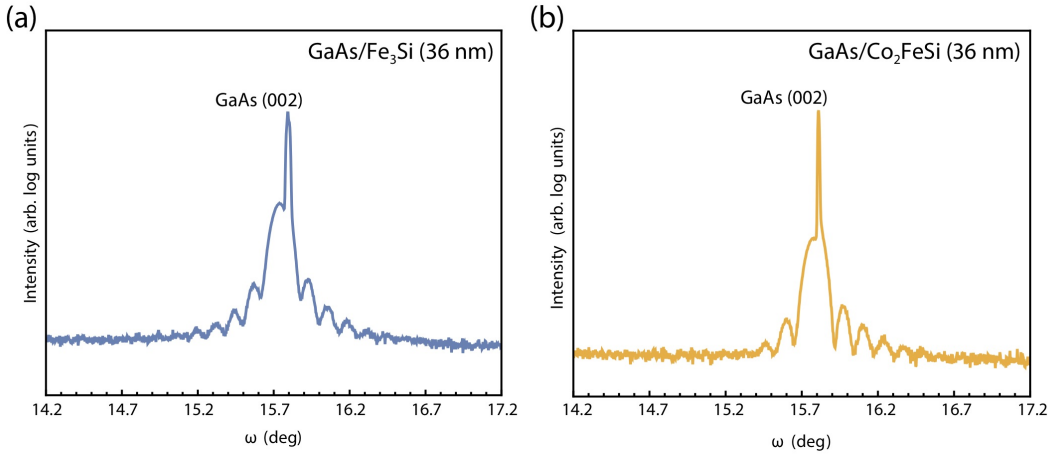

Figure 4.2: XRD of 36 nm Fe_3Si and Co_2FeSi, both on GaAs substrates, about the GaAs (002) reflection showing finite thickness oscillations.

The choice of growing Fe_3Si or Co_2FeSi with 36 nm thickness as a first layer is somewhat arbitrary at this time (layers with different thicknesses were also investigated). However, the idea here is to tune the ratio of this first layer with the thickness of the subsequent layer into a well-defined ratio in order to easily identify the finite thickness oscillations of each film in the XRD curves. For instance, by growing the next layers with 4 and 12 nm, the oscillations should show commensurate beating patterns in a ratio of 1:9 and 1:3. This will become important to assess the quality of the interfaces within the heterojunctions. This range of thicknesses is also ideal given the wavelength of the X-rays used, producing a sufficient number of oscillations to resolve each film before the signal is lost to noise. The GaAs/Fe_3Si (36 nm) samples constitute the starting point from which the SPE of Ge will be investigated.

4.1.2 The solid-phase epitaxy approach

Generally speaking, SPE is a technique used to crystallize an amorphous compound by annealing. Heat applied to a sample provides the energy required to activate chemical bounds and agitate the atoms, which under the right conditions can push the amorphous film to reconfigure into a single-crystalline lattice. The goal here is to develop and optimize a SPE approach to crystallize amorphous Ge over Fe_3Si. The technique was found successful in sim-

ilar thin film applications.[93,94] As explained previously, Fe_3Si grows crystalline in our MBE at 200°C, while Ge requires (at least) a slightly higher temperature in the 300°C range. In our study, we aim to take advantage of the the relatively small difference in crystallization energy between the two Fe_3Si and Ge, which gives hope to obtain fully crystalline Ge after annealing, while avoiding intermixing and degradation of the interface. If the approach is successful, a capping Fe_3Si layer could then be safely grown at 200°C over Ge, as schematized in Fig. 4.3. The amorphous film is obtained by depositing Ge with a substrate temperature of 150°C. The challenge lies in finding the optimal Ge thickness, annealing rate, annealing time, and peak temperature in order to obtain crystalline Ge, assuming that the feat is possible.

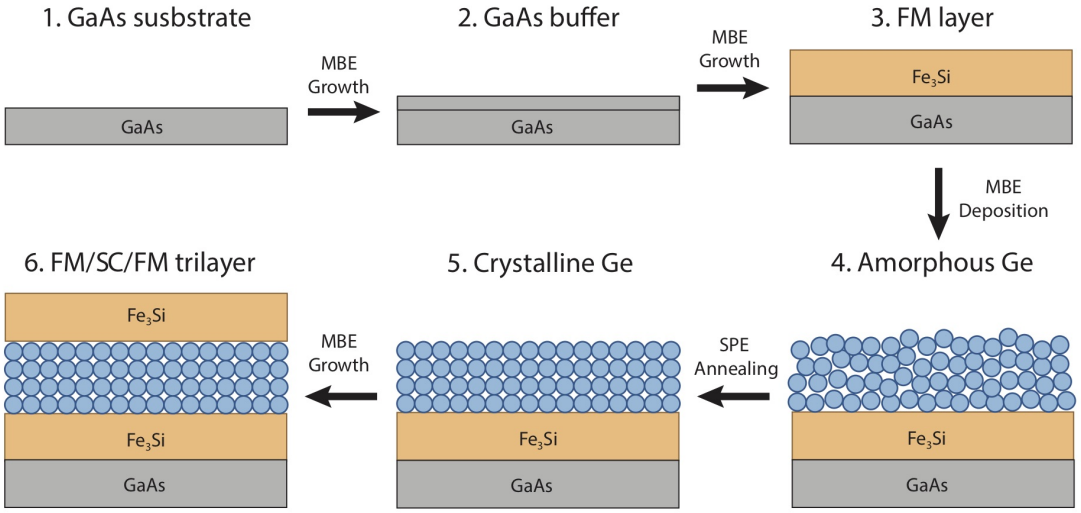

Figure 4.3: Diagram showing the growth sequence of a trilayer stack including the SPE approach in the ideal case. A GaAs buffer layer is applied on the substrate (2), on which a first crystalline Fe_3Si film is grown (3). The amorphous layer of Ge is deposited (4) and would then be crystallized by annealing into its pure diamond cubic form (5), after which a capping Fe_3Si layer could be grown epitaxially (6).

4.1.3 Annealing parameters optimization in Fe_3Si/Ge bilayers

A compelling part of the investigation concerns, first, the optimization of the annealing parameters required to crystallize amorphous Ge over Fe_3Si. Those parameters are the annealing rate R_H, the annealing time t_A and the annealing temperature T_A. The SPE of Ge was previously studied experimentally and theoretically[95–98], however not specifically on metallic Heusler alloys. Knowing that Ge grows crystalline on GaAs at 300°C, a possible range of T_A between 200 and 380°C was investigated with hope observing crystallization from the amorphous phase. As discussed in the previous chapter, experiments have demonstrated that depositing Ge on Fe_3Si using a substrate temperature of 150°C yields an amorphous film while preserving the integrity of the Fe_3Si/Ge interface. The idea is to start from there and attempt to crystallize the amorphous film by annealing.

Preliminary growth experiments were conducted by J. Kalt in 2015 in the context of a masters project. For that purpose, bilayer samples were prepared with 9 nm of amorphous Ge over 9 nm of Fe_3Si, on GaAs(001) substrates. A series of samples were annealed at different rates and temperatures. The effect of the different annealing parameters was investigated during growth by RHEED, and subsequently by AFM and XRD, revealing information about the crystallinity of the films, surface roughness and interface quality. AFM suggested that a slow annealing rate R_H = 5°C/min yields smoother Ge surfaces with rms roughness as low as 1 nm. The parameter which has the most drastic effect on the structure of thin film is the annealing temperature T_A. The effects of T_A are well illustrated by the XRD curves shown in Fig. 4.4, showing six different samples that were annealing at temperatures ranging from 240°C to 380°C (the lower curve shows a sample without any annealing), with R_H = 5°/min, and annealed for 10 min once T_A is reached. In (a) the wide $\omega - 2\theta$ scan, from ω=9 to 64°, covers the (002), (004) and (006) reflections of the GaAs substrate (fine sharp peaks). The Fe_3Si peaks are superimposed, as expected from the lattice-matched growth, with finite thickness oscillations corresponding to 9 nm better visible in the close-up view in (b). The curves associated with T_A of 240, 280 and 320°C contain similar features: the Fe_3Si peaks and oscillations remain visible, which indicates that the interfaces of the film are well preserved. Also noticeable are the broader peaks at 16°, 25°, 35°, 45°, and 57°. The location of these peak do not correspond to those of pure Ge, indicating the presence of a different compound. The position of the peaks being slightly to the right of the GaAs peaks hints towards slightly smaller lattice parameters. Later investigations will explain that the compound associated to this XRD peak is $FeGe_2$, as labeled in the figure.

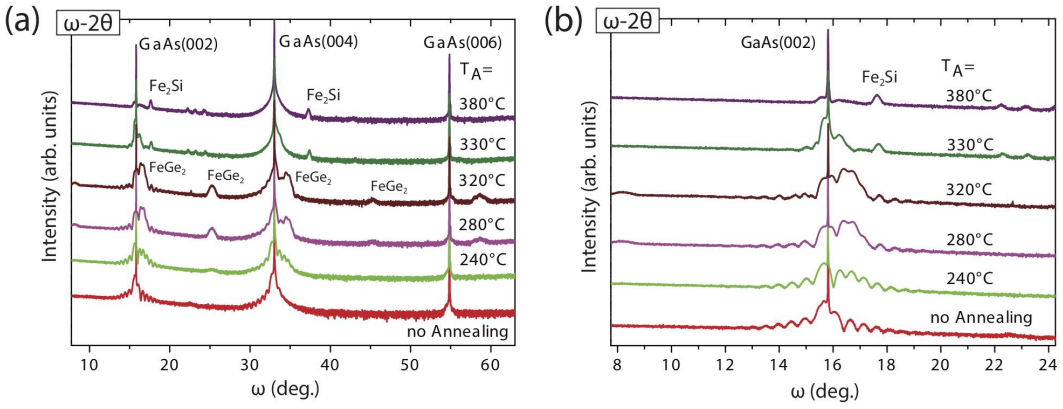

Figure 4.4: (a) Wide $\omega - 2\theta$ scans for 9 nm amorphous Ge annealed at different temperatures over 9 nm Fe_3Si on GaAs(001). (b) Detailed view of the curve about the GaAs(002) substrate peak. [91]

The Fe_3Si peaks are reduced for the T_A = 330°C, and vanish completely at T_A = 380°C. The disappearance of the peak indicates that the layer was totally degraded during the annealing process. Instead, a new peak associated to the byproduct Fe_2Si emerges. The creation of this byproduct already became noticeable at T_A = 330°C. Those annealing temperatures ($>$ 330°C)

are evidently too high, producing intermixing and destroying the Fe_3Si/Ge interface. Based on these XRD curves, the optimal T_A should be found between 240 and 320°C.

Since the goal of the SPE approach is to crystallize amorphous Ge over Fe_3Si while preserving impeccable interfaces with minimal intermixing, the optimal T_A should be the *lowest* at which a crystalline compounds starts to form. Building on the results of J. Kalt, the range of annealing temperatures was reduced to allow a finer investigation. This time, bilayer samples with 36 nm of Fe_3Si and 4 nm of amorphous Ge were prepared, annealed to T_A at 5°/min for 10 min. The deposition of a thinner Ge film (4 nm instead of 9 nm) is justified in two ways. On the first hand, the full crystallization of a thinner film is expected to be easier to realize, requiring less energy and thus reducing the chances of intermixing at the interface. In this case, the possibility to proceed in a sequential way subsists, where thin amorphous Ge films are crystallized one after the other to reach the desired thickness. We have to keep in mind, nonetheless, the original aim is to use Ge as a barrier for spin tunneling from one FM contact to another, in which case its thickness should remain below 4 nm (or thinner) to preserve a meaningful tunneling probability amplitude (see Eq. 2.2).

As the samples are grown in the MBE metal chamber, RHEED serves as an indicator of the crystallinity of the Ge-rich compounds. The deposition of amorphous Ge and annealing routine is represented schematically in Fig. 4.5. As the Ge amorphous layer is deposited on top of Fe_3Si at 150°C, the RHEED streaks disappear. This is due to the fact that the disordered film does not offer any periodic lattice for diffraction to occur. The annealing begins after the 4 nm Ge film is deposited, until the desired T_A is reached. For sufficiently high T_A, a RHEED pattern starts to re-emerge, usually after ∼4 minutes. The annealing temperature is then maintained for 10 minutes, after which there is no noticeable change in the RHEED pattern, indicating a that the process is stabilized and the crystallization is 'complete'. The samples are then brought down to room-temperature and taken out of the MBE.

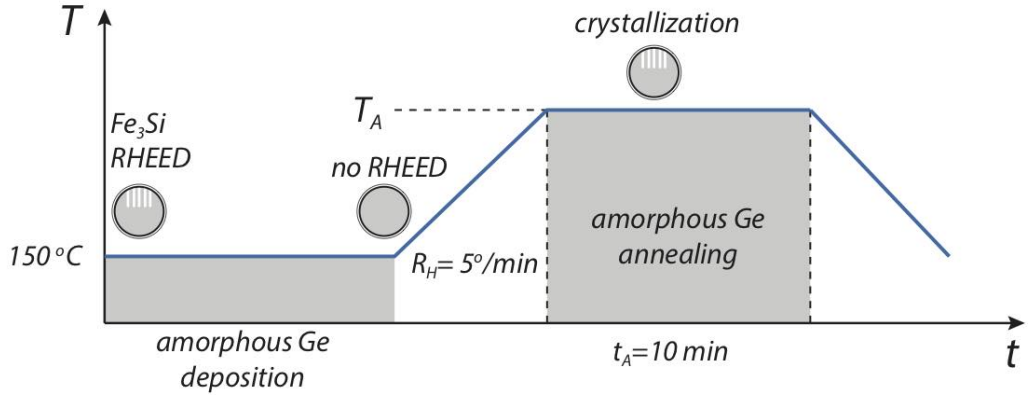

Figure 4.5: Schematic showing the deposition of amorphous Ge and annealing with relevant parameters identified.

Fig. 4.6 shows the XRD curves taken for the Fe_3Si/Ge (36/4) nm bilayers annealed between 200°C and 260°C. A bilayer that was not annealed is also shown as a reference (lower purple curve). In (a), all curves contain the GaAs substrate (002) and (004) peaks, with su-

perimposed Fe_3Si peaks and finite thickness oscillations. The period of these oscillations is shorter than those previously shown, as expected from thicker 36 nm films. The close-up views provided in (b) and (c) show that the oscillations persist over a large number of periods, which confirm that the interfaces of the Fe_3Si films are extremely sharp over extended areas of the sample. There is no noticeable difference between the XRD curve of the amorphous Ge (purple) and sample annealed at 200°C (red). The features previously observed in Fig. 4.4 however start to appear with T_A = 225°C. The rounded peaks of $FeGe_2$ are present, carrying the Fe_3Si thickness oscillations. The existence of a $FeGe_2$ (003) peak around 25.5°is related to the layered structure of the material, with reduced (halved) vertical symmetry lifting the systematic extinction usually predicted for cubic crystal lattices bases (such as GaAs and Fe_3Si). An increase in T_A beyond 225°C does not further affect the XRD curves, which can be interpreted as a 'complete' crystallization of the amorphous Ge into $FeGe_2$.

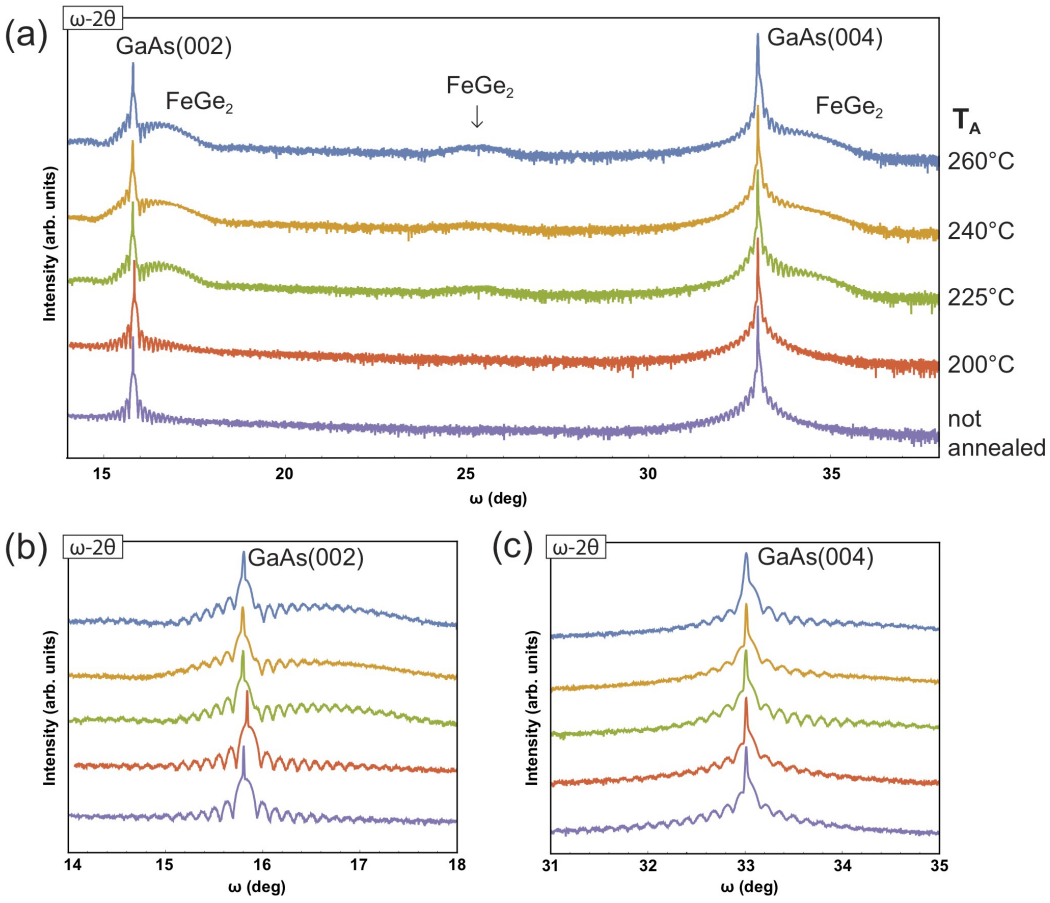

Figure 4.6: (a) Large angle $\omega - 2\theta$ scans of the annealed Fe_3Si/Ge (36 nm/4 nm) bilayers with different T_A. (b) Detailed view about the GaAs(002) substrate peak. (c) Detailed view about the GaAs(004) substrate peak.

At this point, RHEED and XRD cannot probe the details of the interface, and are not sensitive enough to detect sub-nm amounts of materials that would be left amorphous. The following investigations will reveal more about the crystalline structure of the films, and the

surprising formation of $FeGe_2$ which proceeds by diffusion of Fe into the amorphous Ge layer. At this point, our investigation demonstrates that the annealing of Ge can be achieved while preserving a high quality of the underlying crystalline Fe_3Si film. XRD and RHEED indicate that the SPE method yields a crystalline film on top of which the growth of a capping Fe_3Si can be attempted. The next section will describe the growth of the full trilayers.

4.1.4 Growth of $Fe_3Si/FeGe_2/Fe_3Si$ trilayers

With sufficient evidence that a crystalline compound forms by means of the SPE approach, the growth of a capping Fe_3Si layer was attempted using the well established MBE procedure described in the previous chapter. In this part of the study, the samples were annealed with T_A = 260°C for 10 min (the XRD does not show sign of interface degradation at this temperature, and seems to favor a complete crystallization of the amorphous film), after which they are brought back to the growth temperature of Fe_3Si (200°C). The shutters are left opened for 45 min, which under normal conditions yield a 12 nm Fe_3Si layer.

RHEED

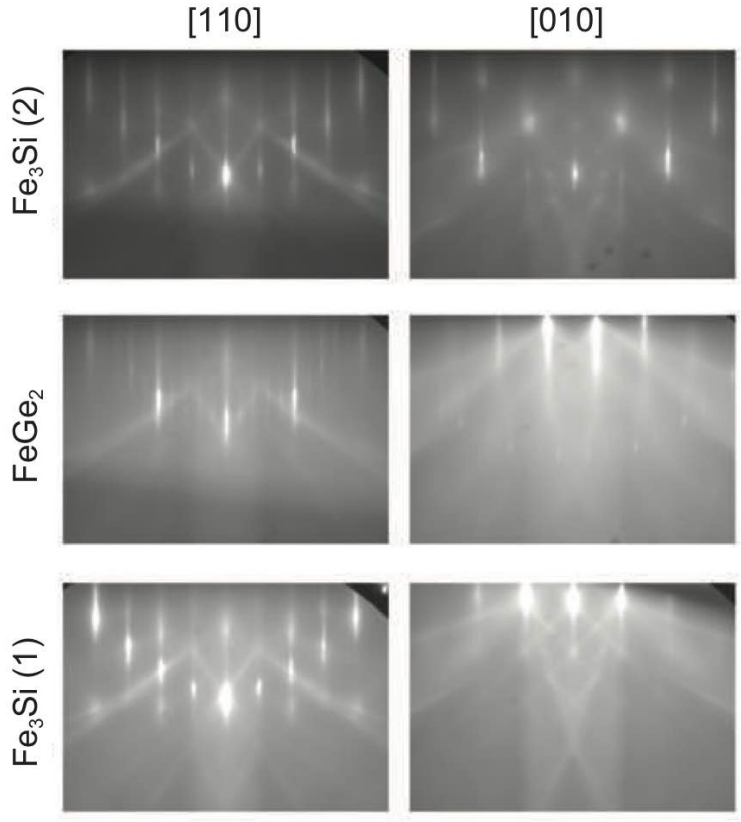

Figure 4.7: *In-situ* RHEED patterns along the [110] and [010] azimuths, taken after growing each layer of the $Fe_3Si/FeGe_2/Fe_3Si$ sample. All three layers are lattice-matched, and show ideal crystallinity.[91]

As the Fe_3Si layers are grown and during the SPE of Ge, the samples are constantly monitored by *in-situ* RHEED. Fig. 4.7 shows RHEED images taken after the growth of each layers in a typical $Fe_3Si/FeGe_2/Fe_3Si$ trilayer sample along the two main crystallographic azimuths, [110] and [010]. The RHEED images show that all layers are crystalline and lattice-matched. One can see that the patterns for both Fe_3Si (1) and Fe_3Si (2) layers are identical, and perfectly aligned for the two given orientation of the MBE sample holder. The RHEED image corresponding to $FeGe_2$ is shown as it appears at the end of the 10 min. annealing time. This pattern appears slowly as the compound forms, forming streaks that coincide with those of Fe_3Si for both orientations. The distance between the main vertical streaks are identical, which proves that there is a physical correspondence between the lattice spacing of the compounds. The fact that the patterns are aligned confirms that the growth is pseudomorphic across the whole layer stacks. In other words, the lattices preserve the epitaxial relationship and the matched films sit directly on top of each other with minimal strain. The clarity of all patterns and presence of Kikuchi lines suggest that the compounds have high crystalline quality, with sharp and flat surfaces.[91]

The observed Fe_3Si RHEED patterns correspond to what one would expect for this material, and can compared to what has already been reported in literature on the topic.[64] However, the patterns of $FeGe_2$ are unexpected and show streaks that are different from those expected for pure Ge. The exact structure of $FeGe_2$ will be discussed in the following section, along with the investigations conducted to first *identify* that the compound is indeed $FeGe_2$.

AFM

The optimization of the SPE annealing parameters relied on AFM measurements to assess the samples' surface quality. Indeed, incorrect growth and annealing parameters can deteriorate the surface of the films, which would prevent the realization of high quality heterojunctions and hinder spin transport across the FM films. AFM can further illustrate the quality of the individual layers and offers extra information regarding the relative roughness of the Fe_3Si and $FeGe_2$ surfaces. To illustrate the success of the SPE approach, Fig. 4.8 (a) contains (10×10) μm^2 AFM scans taken on four different samples, each of them containing an extra layer building up to the full trilayer stack using the optimal annealing parameters determined above. (A deeper AFM study has been published by J. Kalt.[99])

In Fig. 4.8, the image labeled (1) shows the surface of a sample on which a 36 nm layer of Fe_3Si has been grown by MBE. This film is grown following well established procedures, and therefore shows a typical rms roughness (R_{rms}) of 0.357 nm. The surface can be considered atomically flat, and depicts state-of-the art epitaxial films achieved by MBE. Image (2) shows the sample after the deposition of 4 nm of amorphous Ge. The roughness is comparable, even slightly decreased down to 0.339 nm. One should note that each of the images shown here are taken using different samples (samples are usually not put back inside the MBE system), and the roughness of the underlying Fe_3Si could vary within this range. The difference in roughness between the sample shown in (1) and (2) is therefore not significant. Then, the annealing of the amorphous Ge generates the $FeGe_2$ surface shown in image (3). In this case,

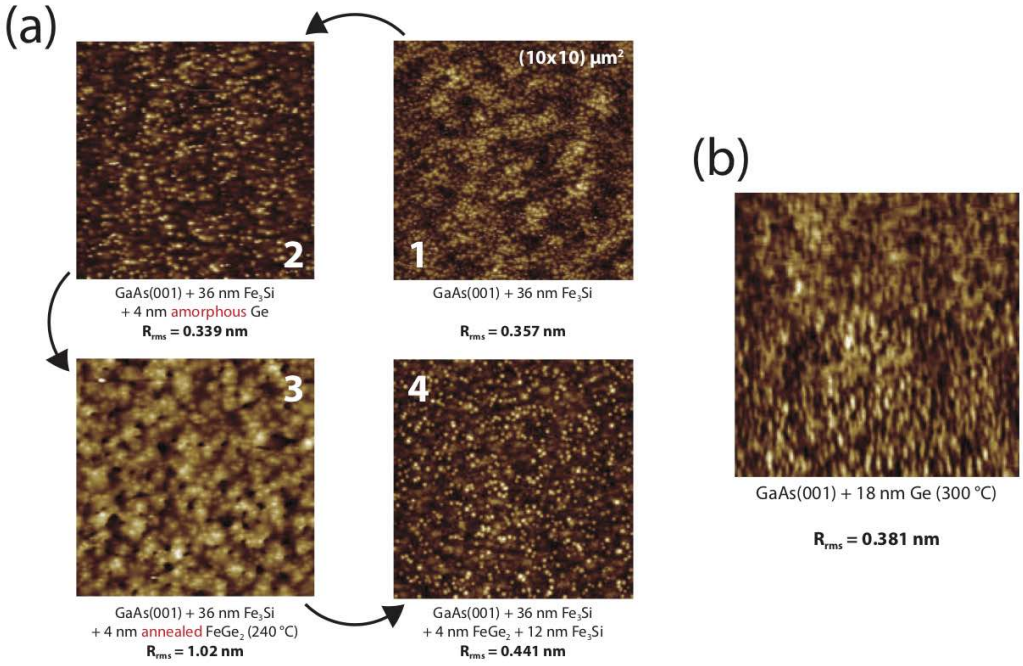

Figure 4.8: (a) AFM of individual layers constituting a trilayer stack. (b) Ge is also shown as reference and to illustrate the difference with $FeGe_2$ surface. All layers grown by MBE show ideally low rms roughness, as expected for such epitaxial films. The annealed $FeGe_2$ layer is comparably coarse, but is not negatively influencing the capping Fe_3Si layer.

the rms roughness reaches R_{rms}=1.02 nm. This value is objectively 'low' for such epitaxial films, and the $FeGe_2$ layer can be still considered ideally flat. Indeed, the 12 nm capping Fe_3Si shown in (4) brings back the rms roughness to 0.441 nm. Fig. 4.8 (b) shows the AFM taken on a pure crystalline Ge surface as reference. The surface structure is qualitatively different from that of $FeGe_2$.

TEM

One of the most striking evidence of the high quality of the $Fe_3Si/FeGe_2/Fe_3Si$ trilayer stacks is found in the the following set of TEM images, produced by B. Jenichen. Fig. 4.9 shows cross-section HRTEM (a), dark-field TEM (b) and SAD (c) images of a trilayer stack with film thicknesses of (36/4/12) nm.[91] The sample was cut and a lamella prepared parallel to the (110) planes, with conventional growth direction along the (001) direction. In (a), the close-up view of the HRTEM contains the top of the first 36 nm Fe_3Si film, the 4 nm $FeGe_2$ buffer layer, and the top 12 nm Fe_3Si film. The image illustrates the exceptional quality of the layers and interfaces. As previously indicated by the RHEED images, the HRTEM confirms that both Fe_3Si films preserve the same orientation. Both $Fe_3Si/FeGe_2$ interfaces are atomically flat and lattice-matched. The wider field of view presented in (b) also suggests that the interfaces are uniform over larger areas of the sample. In (c), the SAD pattern shows the spots generated as

the electron beam diffracts through all three layers, whose clear appearance is expected from the high crystalline quality of the layer stack.

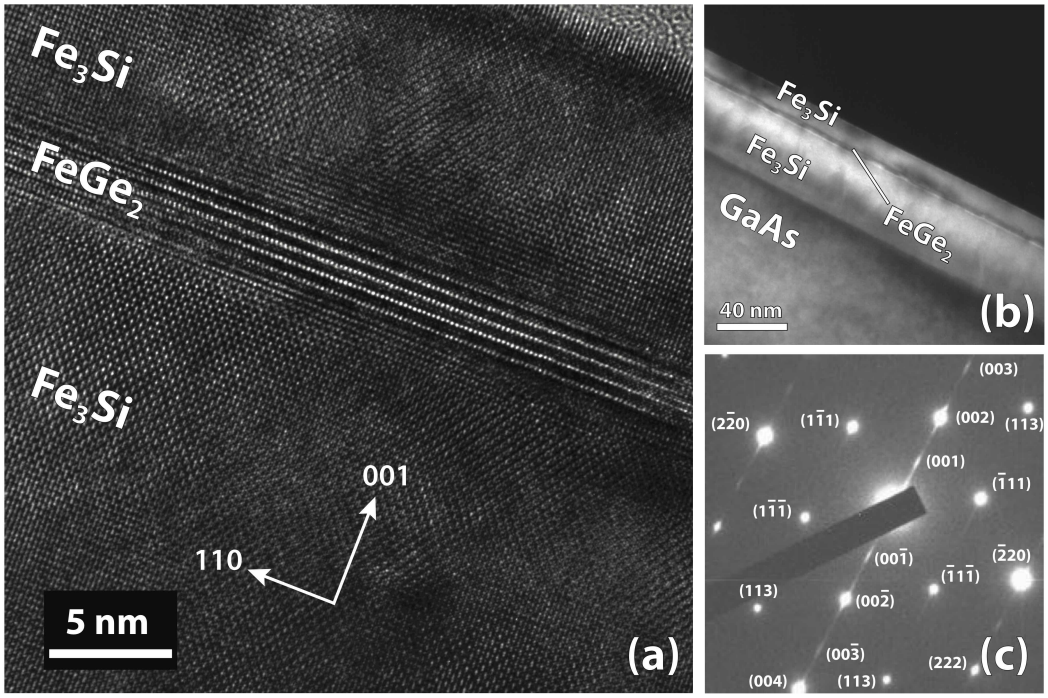

Figure 4.9: (a) HRTEM of a $Fe_3Si/FeGe_2/Fe_3Si$ stack, displaying the impeccable interface sharpness and preserved growth orientation. The layered nature of $FeGe_2$ appears clearly from the bright (Fe) contrast spots separated by darker Ge atoms. (b) A large dark-field TEM view of the sample, revealing ideal interface sharpness over wide areas. (c) SAD pattern including all three layers, where visible (001) and (003) reflections appears due to the symmetry lifted by the layered structure of $FeGe_2$.[91]

The layered structure of $FeGe_2$ can be clearly identified in the HRTEM shown in (a). The contrast reveals ordered monoatomic layers of Fe (bright), sitting between tetragonal Ge formations. The presence of these Fe atoms halves the periodicity of the lattice, which in turn gives rise to the so-called $FeGe_2$(003) peak visible in the XRD curves, as well as the (001) and (003) spots labeled in the SAD image which should not appear in case of diamond cubic Ge or Fe_3Si. The first conclusion to draw is that the SPE of Ge over Fe_3Si yields a fully crystalline lattice-matched compound, $FeGe_2$, which preserves ideal interface sharpness. In that sense, the original attempt to grow lattice-matched hybrid trilayers can be regarded as successful. At this point, the properties of $FeGe_2$ remain to be clarified in order to assess whether the trilayer stacks can be used to implement a SS-SBTT.

Variation of the $FeGe_2$ film thickness

The capabilities of the SPE were put to test by attempting to grow $Fe_3Si/FeGe_2/Fe_3Si$ trilayers with different $FeGe_2$ thicknesses. For device applications, the exact width of the tunnel barrier between the FM films will likely have to be optimized, hence the importance to understand

and master the crystallization of $FeGe_2$. Fig. 4.10 contains XRD curves of $Fe_3Si/FeGe_2/Fe_3Si$ trilayers with $FeGe_2$ thicknesses ranging from 4 to 8 nm. The bottom curve (red) corresponds to a $Fe_3Si/FeGe_2$ bilayer, presented as reference. For this series of samples, the annealing was done at $T_A = 240°C$, which was found to be adequate to crystallize $FeGe_2$ layers up to 8 nm. In all samples, the bottom Fe_3Si layer is 36 nm thick, while the capping Fe_3Si layer is 12 nm. The 1:3 ratio of these layers results in finite thickness oscillations which have periodicity which also respects the 1:3 ratio (with period inversely proportional to the film thickness). The effect of the capping layer is therefore easily made visible in the beating pattern observed in the trilayers, identified in the close-up view of Fig. 4.10 (c). The bilayer curve only features the short period oscillations caused by the thicker 36 nm Fe_3Si film. The presence of these beating patterns proves that the XRD curves indeed produces a convolution of both individual films contributions. This indicate that both interfaces with the $FeGe_2$ buffer layer are very flat over large areas of the sample, and generalizes the observations made by HRTEM over limited sections of a sample.[91]

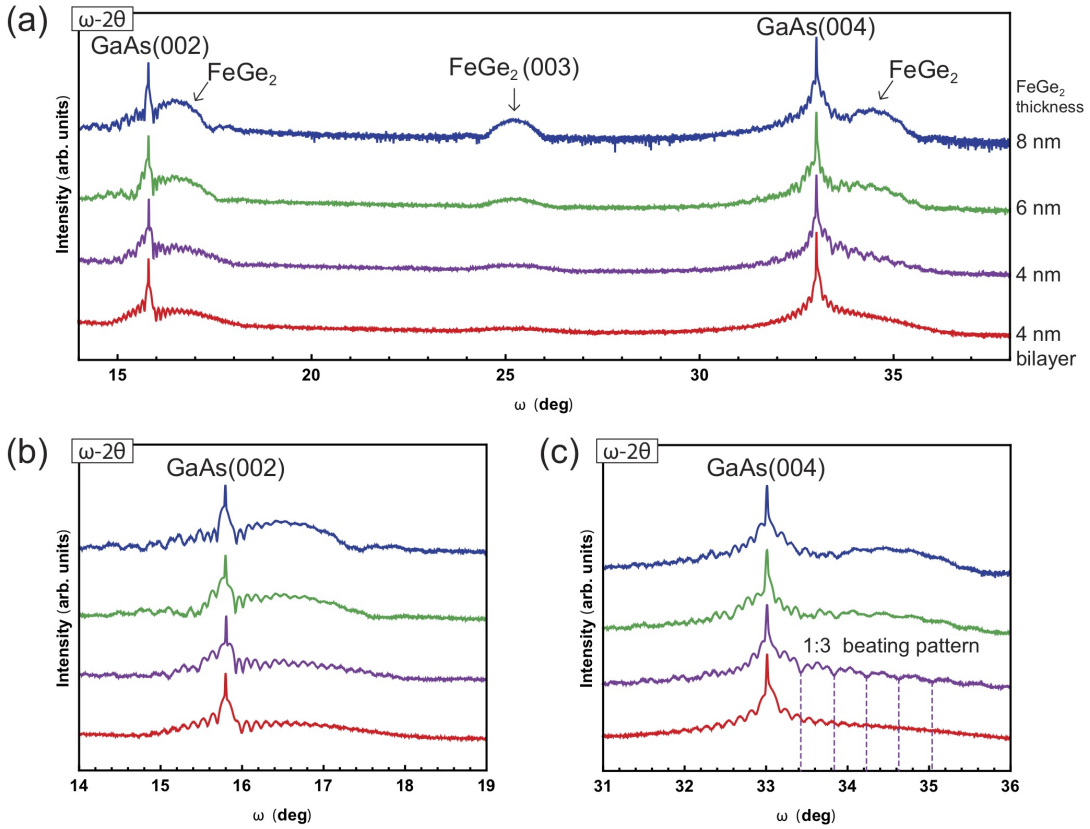

Figure 4.10: (a)-(b) XRD of $Fe_3Si/FeGe_2/Fe_3Si$ stacks with different $FeGe_2$ layer thicknesses, with a bilayer (red) shown as reference. The clear contribution of both Fe_3Si is recognizable in the beating patterns with 1:3 period ratio in (c), while the rounded peaks intensities correlate with the thickness of the $FeGe_2$ layer.[91]

The presence of $FeGe_2$ with different thicknesses can be recognized in the characteristic rounded peaks identified in (a). There is a clear correlation between the intensity of these

peaks and amount of Ge annealed during the SPE part of the growth. All three peaks are without any doubt linked to the $FeGe_2$ film. The sample with 8 nm $FeGe_2$ shows weakly emerging finite thickness oscillations (blue curve). The other layers are too thin to produce noticeable oscillations. One should note that the $FeGe_2$(003) peaks appears alone without carrying the finite thickness oscillations produced by the Fe_3Si. Once again, this effect is explained by the systematic extinction of such odd-numbered reflections in the Fe_3Si lattice.[91]

The $Fe_3Si/FeGe_2/Fe_3Si$ (36/8/12) nm trilayer was also investigated by HRTEM in order to probe the quality of the thicker $FeGe_2$ interlayer and capping film (image by B. Jenichen). Fig. 4.11 shows the micrograph produced for this sample. As previously observed in the $Fe_3Si/FeGe_2/Fe_3Si$ (36/**4**/12) nm sample, all films have high crystalline quality with atomically flat interfaces, with slight but noticeable thickness irregularities. The layered structure of $FeGe_2$ is once again recognizable. The film appears homogeneous, with no presence of amorphous Ge that could have been expected due to the film being thicker. This second HRTEM image confirms that the SPE approach allows to create stacks with variable buffer layer thickness (4-8 nm), without compromising the quality of the overall heterostructure.

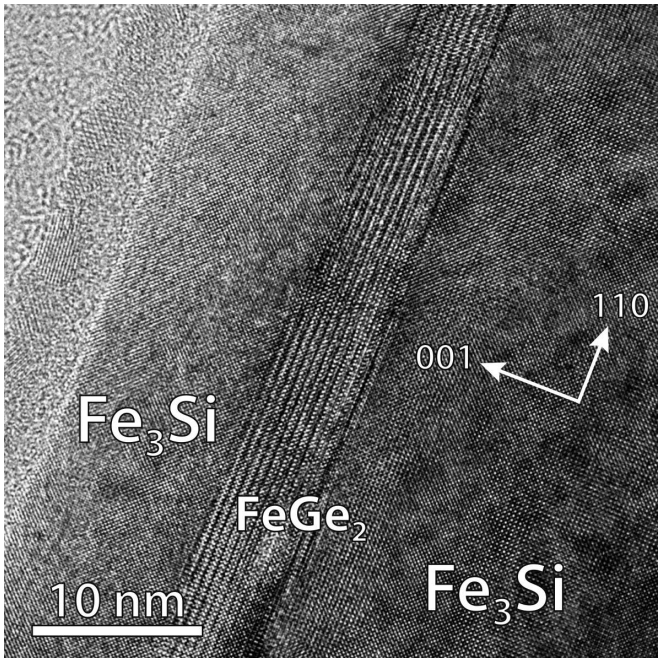

Figure 4.11: HRTEM of a $Fe_3Si/FeGe_2/Fe_3Si$ trilayer with 8 nm $FeGe_2$ (B. Jenichen). The trilayer stack also shows ideal interfaces, and the thicker $FeGe_2$ layer does not compromise the overall crystalline quality of the films.

4.2 The structure of $FeGe_2$

Since the first XRD curves identified new peaks forming at the expense of cubic Ge upon annealing, and TEM images could shed light on the layered structure of the crystalline compound obtained over the initial Fe_3Si layer (in Fig. 4.9, originally referred to as a 'superlat-

tice'[91]), investigations were undertaken in order to identify the exact nature of the film. This work was mainly carried by B. Jenichen *et al*, and conclusions reported subsequently.[100] The crystal structure proposed for $FeGe_2$ is shown in Fig. 4.12. The polymorph has a tetragonal lattice with body-centered Fe atoms in one out of two Ge planes, which corresponds to the space group *P4mm*. The experimental lattice parameters, obtained by XRD analysis, are shown in the figure. The lattice of $FeGe_2$ ($2a$=0.5654 nm) is exactly matched to the lattice of Fe_3Si (a=0.5654 nm) along the x axis, which in this case is perpendicular to the growth direction of the samples.[100] The films therefore sit directly on top of each other without strain, as illustrated in the TEM micrographs of the previous section.

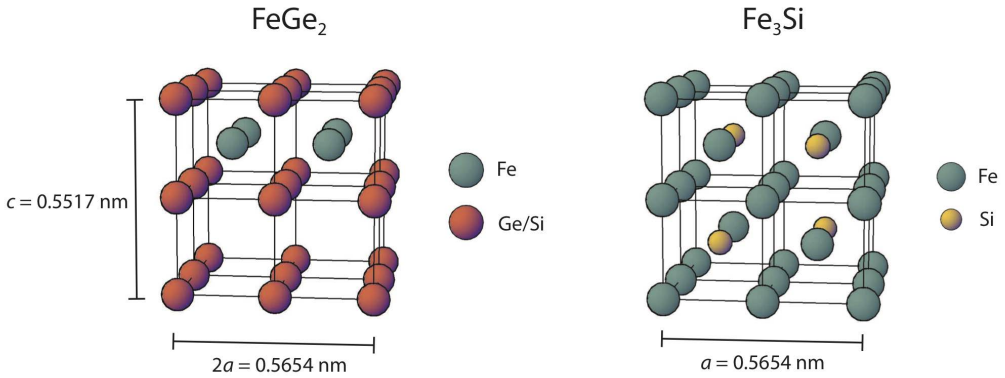

Figure 4.12: The structure of $FeGe_2$ (*P4mm*), with tetragonal primitive Bravais lattice, compared to the Heusler alloy Fe_3Si. The compounds are considered to be lattice-matched given the negligible different in their lattice constants in the plane.

A careful investigation of the diffusion taking place during the annealing of Ge reveals an upper bound on the content of Si incorporated. Assuming a complete absorption and intermixing of the amorphous Ge atoms within the uppermost Fe_3Si region implies that 17% of Si atoms in fact sit on Ge sites, as per the following chemical reaction equation:

$$1\ Fe_3Si + 5\ Ge \rightarrow 3\ Fe(Ge_{0.83}Si_{0.17})_2. \tag{4.1}$$

Despite the presence of Si atoms, for the sake of simplicity and clarity, the compound was and will remain through the rest of this thesis referred to as $FeGe_2$.

4.2.1 Energy-dispersive X-ray spectroscopy

An experimental evidence for the stoichiometry and presence of Si within $FeGe_2$ comes from energy-dispersive X-ray spectroscopy (EDX) measurements using the JEOL ARM200 (also used for HAADF). EDX is a spectroscopy method which can scan a sample and resolve spatially the chemical elements present in a sample. It relies on the unique electronic structure of each elements which contribute with specific peaks in the emission spectrum when excited by X-rays. The detector is sensitive to the intensity and energy of photons emitted during

the transitions of electrons between the discrete shells bound to the atomic nucleus. The data collected can then be plotted as a map indicating the location of each element in space.

The EDX measurement shown in Fig. 4.13 reveals the position and percentage of Fe, Ge and Si atoms along the cross-section of a $Fe_3Si/FeGe_2/Fe_3Si$ (36/4/12) nm trilayer sample. The three films are clearly recognizable in the density map, where Fe atoms are colored green, Si blue, and Ge yellow. The resolution, although limited, provides estimates for the percentage of the elements found in each parts of the layer stack. The Fe_3Si layers consistently contain 75% Fe and 25% Si atoms, as expected. The $FeGe_2$ film, being only 4 nm thick in this sample, appears as a distribution in which, at its highest point, the ratio of Fe to Ge (and traces of Si) atoms is about 1:2. Based on this measurement, the $FeGe_2$ film contains on average 60±5 % Ge, 35±5 % Fe, and 5±5 % Si.[100]

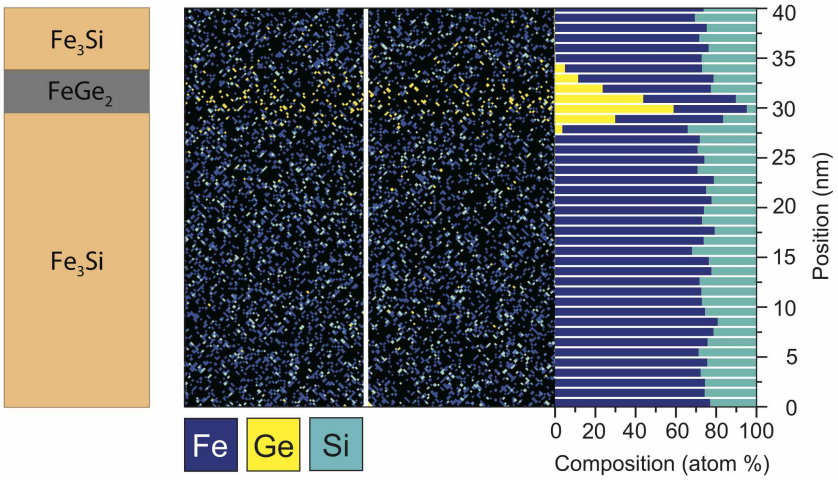

Figure 4.13: EDX of a $Fe_3Si/FeGe_2/Fe_3Si$ (36/4/12) nm trilayer taken in the vicinity the $FeGe_2$ interlayer.[100] The measurement clearly indicates the $FeGe_2$ film containing small traces of Si, in a ratio of 2:1 with the Fe atoms. The Fe_3Si films contain, as expected, a ratio of 3:1 between Fe and Si atoms.[100]

We notice that a number of Ge atoms are found relatively deep in the underlying Fe_3Si film. If accurate, the presence of these atoms could suggest that the annealing process promotes a strong migration and intermixing. The resolution of the measurement is however not high enough to evaluate the role of Ge in changing the properties of the Fe_3Si film. The presence of Ge therefore remains a negligible statistical deviation, as seen from the average composition percentage bar diagram.

4.2.2 TEM experiments and simulations

The structure of $FeGe_2$ was definitely understood by comparing TEM HAADF cross-section micrographs of a $Fe_3Si/FeGe_2/Fe_3Si$ sample to a simulated model for the $FeGe_2$ *P4mm* structure. The sample used to obtain the images is the same as for the EDX measurement shown above, a $Fe_3Si/FeGe_2/Fe_3Si$ (36/4/12) nm trilayer. The experimental and theoretical TEM mi-

crographs are presented in Fig. 4.14, along reproductions of the corresponding crystal structures to guide the interpretation of the contrast spots.

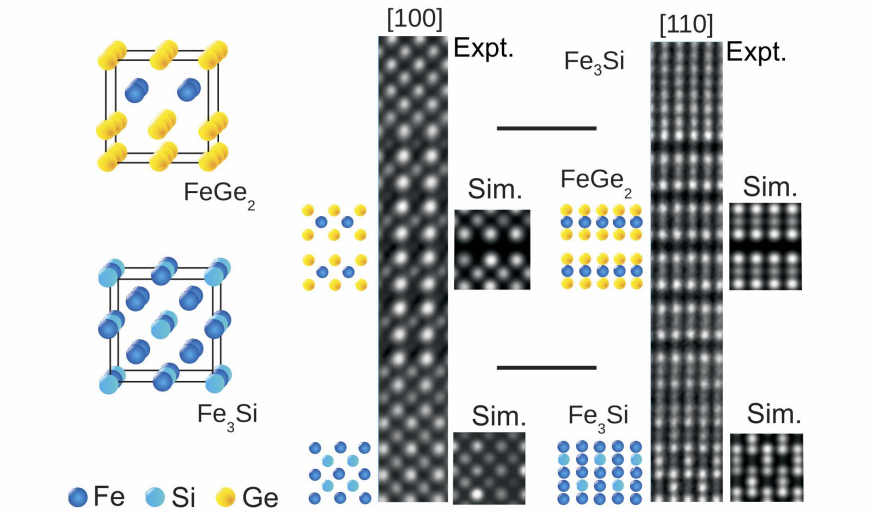

Figure 4.14: TEM experimental measurements and simulations revealing the structure of Fe_3Si and $FeGe_2$, with 3D diagram of the lattices as comparison. Both the [100] and [110] projections agree with the theoretical prediction, clearly revealing the layered structure of the $FeGe_2$ film.[100]

The long strips are the experimental images collected along the the [100] and [110] projections, both measuring 1 nm wide. The Fe_3Si structure is easily recognizable from the typical 'triplets' visible along the [110] orientation of the sample, with bright spots corresponding to Fe atoms and faint spots being the Si atoms. Those are compared to simulations of the expected pattern, shown in the small squares next to the strips. The simulations agree strikingly with the experimental micrographs along both orientations. The $FeGe_2$ region contains clear 'gaps' in which, on average, no Fe atoms are found.[100] The original larger-scale images from which the strips were taken are shown in Fig. 4.15. Here again, it is possible to observe the high quality of the layered ordering, extending over the whole are of the micrographs. The $FeGe_2$ film sits lattice-matched in between the two adjacent Fe_3Si layers.

4.2.3 XRD experiments and simulations

The layered nature of the $FeGe_2$ films is at the origin of the unconventional (001) and (003) XRD peaks, which would normally be forbidden for cubic structures (such as GaAs or Fe_3Si). XRD simulations were generated assuming the *P4mm* structure of $FeGe_2$. The resulting curve is shown next to the experimentally collected one in Fig. 4.16. Here again, the simulation reproduces the features observed experimentally, with broad (001), (002) and (003) peaks, confirming the structure proposed for $FeGe_2$. The large width of those peaks is explained by the film being only 4 nm thick.[100] The simulation also reproduces the finite thickness oscillations caused by the 36 nm Fe_3Si film.

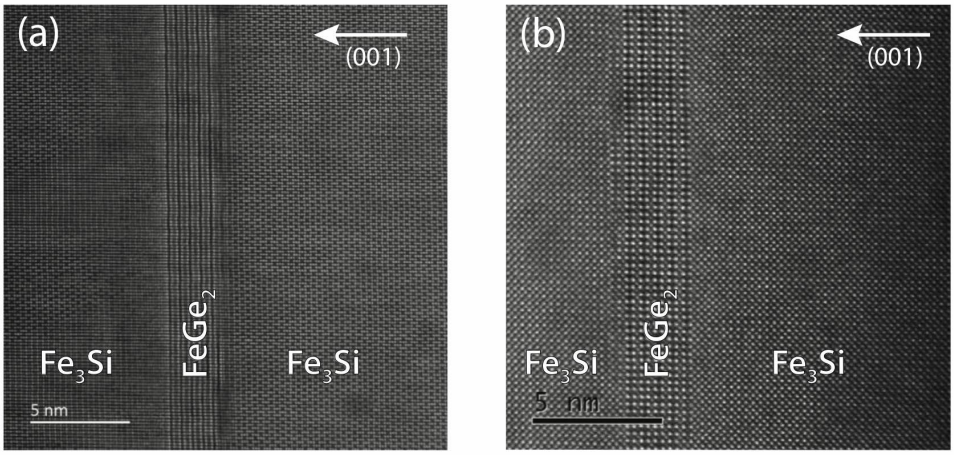

Figure 4.15: (a) STEM HAADF of the [110] and (b) [100] orientation used to produce the stripes shown in Fig. 4.14. The micrographs were published in the supplementary material of B. Jenichen *et al* (2018).

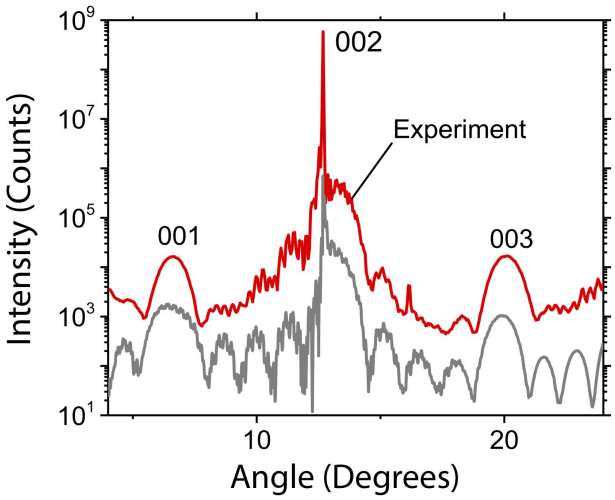

Figure 4.16: XRD simulation (grey) and experiment (red) for a $Fe_3Si/FeGe_2/Fe_3Si$ stack trilayer stack about the GaAs(002) substrate peak. The resemblance of the two curves confirms the *P4mm* structure proposed for the $FeGe_2$ films obtained by SPE. [100]

4.3 Growth of trilayers combining Fe_3Si and Co_2FeSi

The creation of FM/SC/FM hybrid trilayers suitable for the SS-SBTT requires being able to magnetize both FM layers independently. In other words, despite being separated by $FeGe_2$, the stacks should be able to operate as a conventional MTJ, in which both FM layers are decoupled. To achieve this effect, the two FM layers should have different coercivities. Technically, two Fe_3Si layers with different thicknesses should have different coercivities, as interfacial contributions become more prevalent in thin films compared to bulk materials (see eq. 2.11). However, this difference might not be large enough to produce a noticeable antiparallel magnetization state. Another option is to use two different FM materials having intrinsically

different magnetic properties, such as Fe_3Si and Co_2FeSi. This section will present our efforts to obtain different trilayer stacks using various combinations of those two Heusler alloys.

A total of four possible combinations of trilayers are possible using Fe_3Si and Co_2FeSi. Those are illustrated in Fig. 4.17, in which a color convention is used to identify the different materials: orange for Fe_3Si and red for Co_2FeSi. In this part of our investigation, the aims are to first verify if Co_2FeSi can be grown crystalline on top of $FeGe_2$, and then to see if the SPE approach can be extended to the crystallization of Ge on the Co_2FeSi surface. To facilitate the comparison with the $Fe_3Si/FeGe_2/Fe_3Si$ stacks that we previously obtained, the thickness of the FM films were kept in the same as before, (36/6/12) nm, within each the new trilayers (with 6 nm interlayers). The grey buffer layers are labeled $FeGe_2$ when the underlying film is Fe_3Si. As will be clarified next, the annealing of Ge over a Co_2FeSi surface yields another crystalline compound, labeled Ge(Co,Fe,Si).

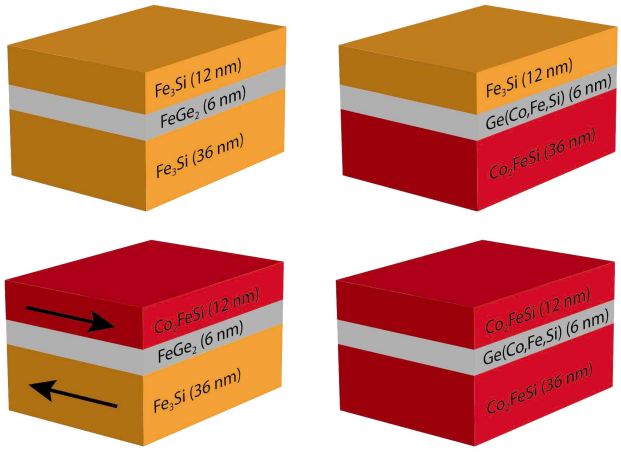

Figure 4.17: Four trilayer stacking sequences containing a first 36 nm FM layer (Fe_3Si or Co_2FeSi), 6 nm buffer layer of crystallized Ge, and a second 12 nm FM. The black arrows illustrate the antiparallel magnetization we hope to realize using films having different coercivities.[92]

4.3.1 RHEED

The first attempt to grow Co_2FeSi was done on top of a $Fe_3Si/FeGe_2$ bilayer sample. It was found that Co_2FeSi can be grown crystalline directly on top of the $FeGe_2$ surface, using the growth conditions described previously. The *in-situ* RHEED taken during the growth of a $Fe_3Si/FeGe_2/Co_2FeSi$ trilayer is shown in Fig. 4.18 (a). 6 nm of amorphous Ge were annealed at T_A=260°C for 10 min, which over the Fe_3Si surface creates the recognizable $FeGe_2$ RHEED pattern. Seen above, the growth of a 12 nm layer of Co_2FeSi leads to the pattern illustrated, depicting a high quality crystalline layer with streaks aligned with those of the $FeGe_2$ for each azimuths. The growth relationship is therefore preserved. The general clarity of the RHEED images and, there again, the presence of Kikuchi lines indicate that both $FeGe_2$ and Co_2FeSi films have ideal crystallinity and flat surfaces.

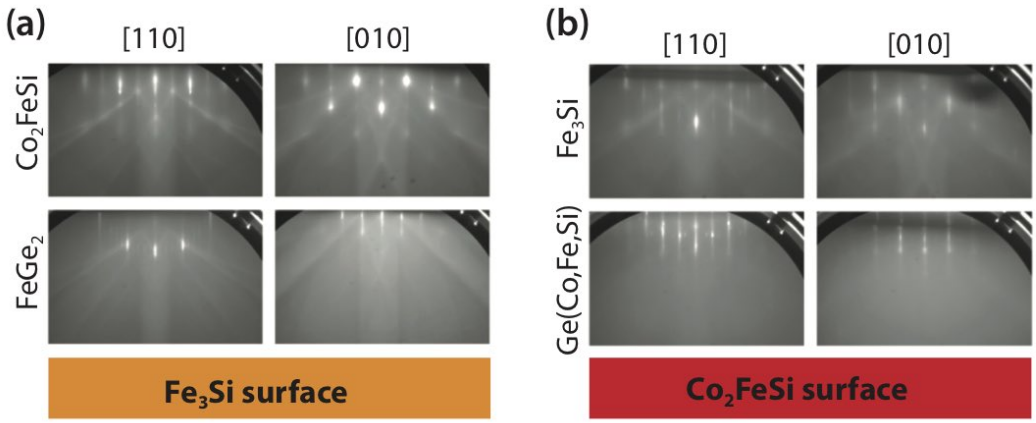

Figure 4.18: The RHEED comparing the SPE of Ge on (a) Fe_3Si and (b) Co_2FeSi surfaces. Once again, the lattice relationship is preserved, even when the annealing is performed on Co_2FeSi. The streak patterns for the annealed film are however different, suggesting the formation of a different crystalline compound referred to as Ge(Co,Fe,Si).[92]

We thereafter attempted to reverse the arrangement of the films within the trilayer stacks by first growing 36 nm Co_2FeSi directly on the GaAs substrate, over which 6 nm of amorphous Ge was then deposited. The annealing of Ge over Co_2FeSi was then performed up to T_A = 245°C for 10 min., and resulted in the RHEED pattern shown in Fig. 4.18 (b). We notice, this time, that the RHEED streaks that appeared after annealing are different that those of $FeGe_2$. They also do not correspond to the pattern one would expect for pure Ge. This unidentified film is nonetheless crystalline, with lattice spacing related to the overgrown Fe_3Si film along the [110] and [010] azimuths. The exact stoichiometry of the Ge(Co,Fe,Si) is not known for now, but the synthesis of the compound likely results from diffusion of atoms from the underlying Co_2FeSi, whose surface is known to be more reactive than that of Fe_3Si. Importantly, the growth of the trilayer stack still proceeds in a pseudomorphic way, with the main RHEED streaks being aligned for the same sample holder orientation. As compared to $FeGe_2$, the Ge(Co,Fe,Si) produces a relatively blurry pattern. The is a limited number of features and no Kikuchi lines, meaning that the surface of the film is not as flat. This does not prevent the capping Fe_3Si to be grown with high quality.

4.3.2 XRD of the four stack combinations

In addition to the two samples discussed above, which contain combinations of Fe_3Si and Co_2FeSi, a Co_2FeSi/Ge(Co,Fe,Si)/Co_2FeSi trilayer could also be realized by growing the capping Co_2FeSi by MBE using the standard procedure. A new $Fe_3Si/FeGe_2/Fe_3Si$ sample was also produced to complete the set of samples shown in Fig. 4.17. The four trilayer stacks were then investigated by XRD. The $\omega - 2\theta$ curves corresponding to each of those are compared in Fig. 4.19. The color code used for each sample is preserved in all (a), (b), and (c) subfigures. The light blue curve in the upper left corner of the insets corresponds to the $Fe_3Si/FeGe_2/Fe_3Si$ trilayer sample (a replica of the sample shown in Fig. 4.10). The dark blue

curve (bottom left) is the $Fe_3Si/FeGe_2/Co_2FeSi$ trilayer. The purple and red curves are the inverted combinations, with Co_2FeSi as the underlying layer, identified in on each plot in (a).

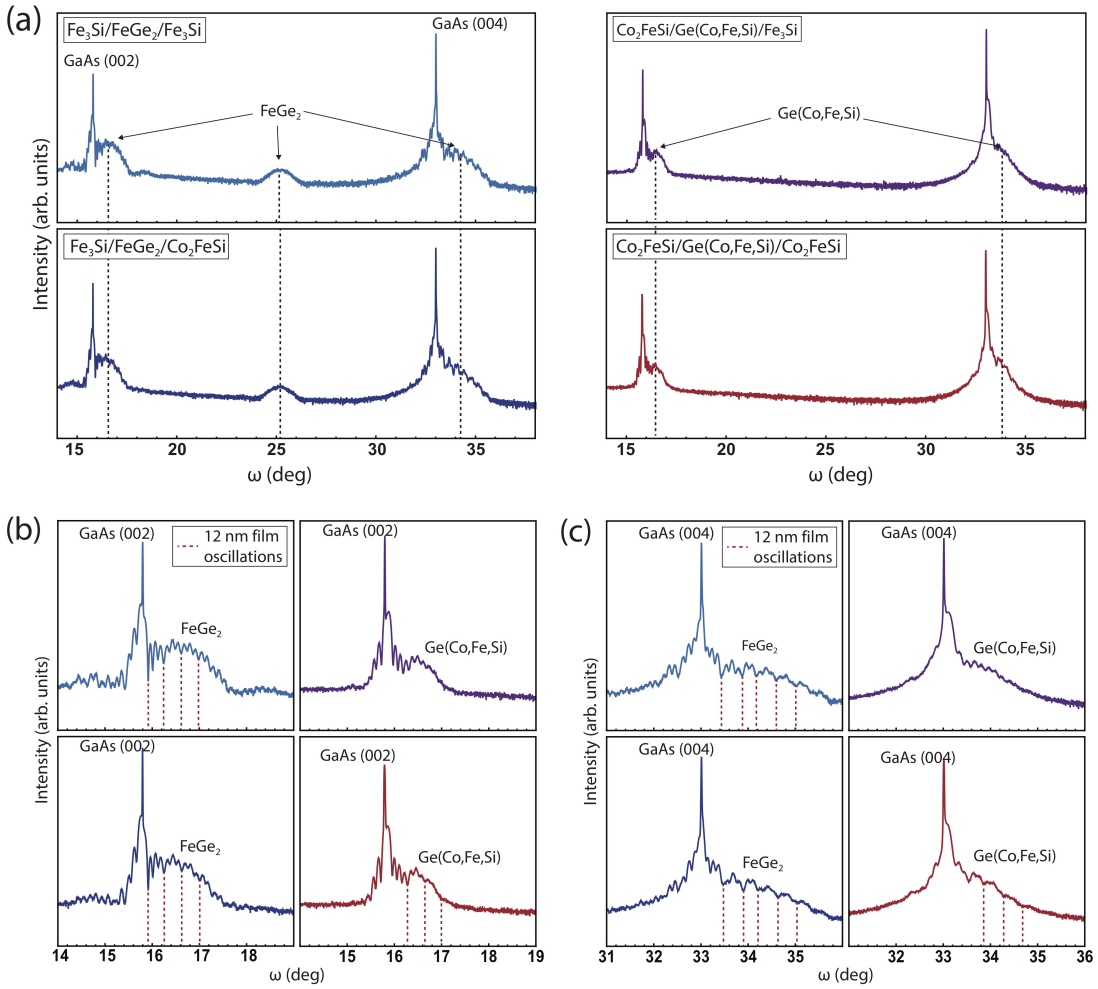

Figure 4.19: (a) XRD of four layer stacks consisting of different combinations of Fe_3Si, Co_2FeSi and Ge compounds and indicated on each curves. (b) Closer view about the GaAs(002) peak. (c) Closer view about the GaAs(004) peak. The presence of $FeGe_2$ is clearly noticed when Ge was annealed over Fe_3Si. The (003) satellite peaks however disappears when the SPE is performed over Co_2FeSi, once again indicating the formation of a different crystalline compound.[92]

In (a), we see a comparison of the four samples over a wide ω range. The two samples having Fe_3Si as a bottom layer show features that were described in previous XRD measurements. The two broad (002) and (004) $FeGe_2$ peaks are present, with the (003) satellite peak slightly above 25°. The contribution from the capping 12 nm Co_2FeSi (bottom left, dark blue curve) cannot be distinguishes from the 12 nm Fe_3Si at this scale, as one expects from the similar structure of the two Heusler alloys. This (003) satellite peak, however, disappears in the two samples for which the annealing was performed over Co_2FeSi. The RHEED images presented above already suggested that $FeGe_2$ and Ge(Co,Fe,Si) are indeed different compounds.

The XRD measurements further corroborates this claim, but also reveal that the Ge(Co,Fe,Si) compound formed during annealing, as opposed to $FeGe_2$, does not have a layered structure. Let us recall that the (003) satellite peak emerges due to the reduced symmetry of the film caused by the Fe planes seen the the HRTEM. Such an effect is not realized in Ge(Co,Fe,Si). Nonetheless, two comparable rounded peaks coincide at angles of $\sim$16.5°and 34°, which still establishes a relationship between the lattices of both Ge-rich films.

Fig. 4.19 (b) and (c) show close up view of the curves about the GaAs (002) and (004) peaks, respectively. As discussed previously, it is possible to identify the contribution from the two FM layers based on the finite thickness film oscillations. The films having a thickness ratio of 36:12 once again translates into beating patterns having a 1:3 periodicity, identified by red dotted lines. The effect is not as visible in the Co_2FeSi/Ge(Co,Fe,Si)/Fe_3Si curve, and therefore indicates inferior film and interface quality. Generally speaking, the number of film oscillations and sharpness of the films appears much clearer in the two samples for which SPE proceeds over Fe_3Si. The better quality of the samples in these cases likely comes from the layered structure of the $FeGe_2$, which while forming drives the diffusion of atoms in a layer-by-layer fashion, preserving the integrity of the interface. [92]

4.3.3 TEM

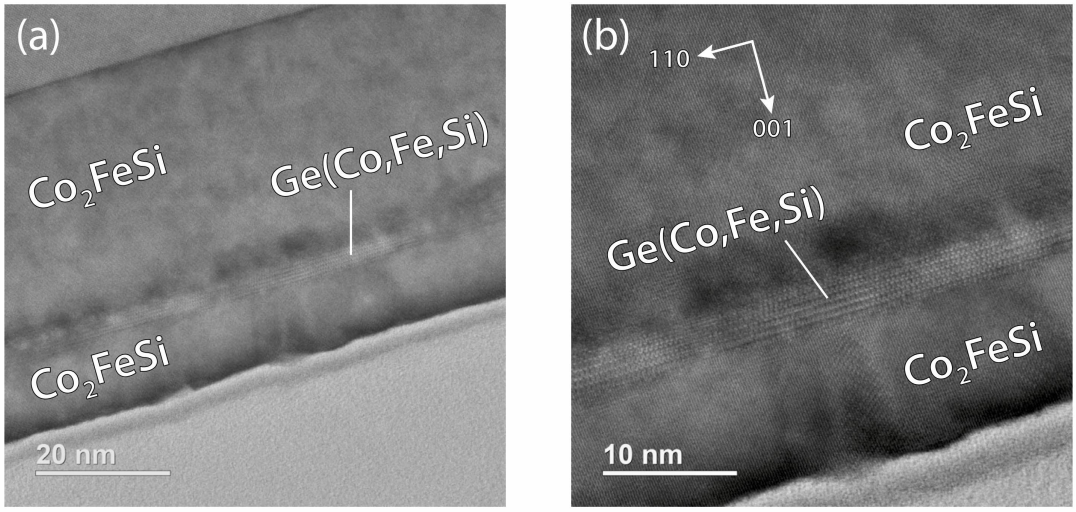

Figure 4.20: (a) Large and (b) close view of a HRTEM micrograph taken using a Co_2FeSi/Ge(Co,Fe,Si)/Co_2FeSi trilayer stack. The crystalline structure of the Ge(Co,Fe,Si) interlayer is visibly different than that of $FeGe_2$. The interfaces with Co_2FeSi are reasonably sharp (although not as good as the $Fe_3Si/FeGe_2$ interfaces).

In order to better understand the Ge(Co,Fe,Si) film formed over the Co_2FeSi surface, the Co_2FeSi/Ge(Co,Fe,Si)/Co_2FeSi sample was investigated by HRTEM. Two micrographs (made by B. Jenichen) are shown in Fig. 4.20 (a) and (b), featuring two magnifications. From the two images, we can reconfirm the result introduced by the XRD measurements: unlike observed in the samples for which the annealing of Ge is performed over a Fe_3Si surface, the

crystalline compound obtained by SPE over Co_2FeSi is not layered. The micrograph shows the GaAs substrate which is lattice-matched to the 36 nm Co_2FeSi layer. However, the interface between the latter film and the Ge(Co,Fe,Si) layer is relatively rough. Ge(Co,Fe,Si) appears nonetheless as a crystalline material, different from pure Ge, with a structure comparable to $FeGe_2$ (also expected from the location of the XRD peaks). The capping Co_2FeSi layer grown by MBE is also crystalline, with the same lattice orientation at the underlying Co_2FeSi. The growth is therefore pseudomorphic across the whole layer stack. It seems that there could be an amorphous deposit on the surface of the capping Co_2FeSi film. This effect is likely caused by handling of the sample during the preparation of the specimen for TEM, and does not reflect the state of the layer stack as it was grown in the MBE system.

4.4 Magnetic behavior of the thin films and stacks

One of the most important part of the investigation of the samples presented previously consists in magnetization measurements. Understanding the magnetic behavior of the FM films and their heterostructures is capital in order to guide our progress towards the realization of a SS-SBTT. SQUID magnetometry experiments were conducted systematically on samples having different combinations of layers, in order to understand the role of each individual films to the overall magnetization of the full trilayer stacks. Since the thin films exhibit magnetic anisotropy, each piece of sample is measured with in-plane field along the [110], [010], and [$\bar{1}$10] directions (see Fig. 3.6), respectively the red, green, and blue curves in all subsequent plots. The magnetization measurements presented in this subsection were conducted by L. Opperman, as work completed in partial fulfillment of the requirements for a Bachelor's degree in physics[1].

4.4.1 Correction of the magnetic hysteresis curves

The SQUID magnetometer used to measure the samples is a sensitive tool able to detect the magnetization of films as thin as a few monolayers. The curves collected must nonetheless by modified to correct for systematic errors introduced in the measurement. First, GaAs is diamagnetic, meaning that the antiparallel magnetization of the thick (350 µm) substrate contributes significantly to the total magnetization of the thin films ($\sim$36-60 nm of ferromagnetic material). This effect becomes apparent at large H fields. By designing the experiment such as to measure from +5000 Oe to -5000 Oe, the linear diamagnetic contribution is fitted (to a first order polynomial) and subtracted from the total signal. The magnetization hysteresis loops are then normalized to the saturation magnetization of the sample, which provides plots with unitless magnetization axis where all curves converge towards 1 or -1. This facilitates the comparison between the samples, which usually have different dimensions.

Next, the supercurrent flowing in the magnet is difficult to completely eliminate, which in turn can introduce a shift in the 'measured' value of the H field applied to the sample. Usually,

[1] Humboldt University of Berlin

a strong positive field will shift the hysteresis curve towards the positive axis, while a strong negative field shifts the curve towards negative values. These shifts have no physical meaning and represent a systematic error caused by the design of SQUID system. A single magnetic hysteresis loop must therefore be constructed from two separate loops, and reassembled based on the average shift caused by the large positive and large negative fields, as shown in Fig. 4.21. The result is a hysteresis loop centered at the origin, with magnetic switching representing the physical coercivity of the samples. Most of the interesting magnetic effects observed in the thin films usually happen within +/-100 Oe. The reason to measure from +/-5000 Oe is to ensure that the layers are completely magnetized at the beginning of the sweeps in both directions (as well as to be able to fit the diamagnetic contribution from the GaAs substrate).

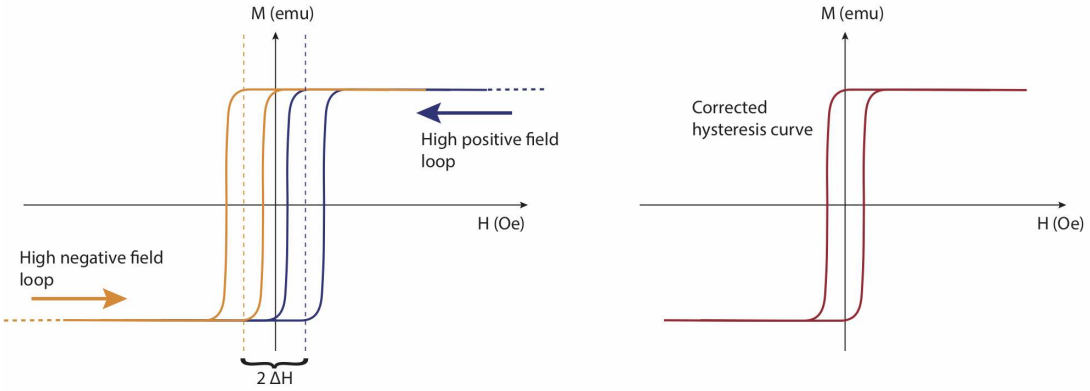

Figure 4.21: Averaging two offset loops into a reliable magnetic hysteresis curve considering the systematic bias introduced by the SQUID magnetometer.

4.4.2 Individual Fe_3Si layer

As a first measurement and reference for the following samples, the magnetization of a single 36 nm layer Fe_3Si was measured at 10 K and 300 K. The hysteresis curves are shown in Fig. 4.22. The loops are as one would expect from such single-crystalline thin films, with very sharp magnetization reversal.

One can first notice that the magnetization curves at low and high temperature are very similar. Fe_3Si is expected to loose its ferromagnetic character at a temperature of 840 K (its Curie temperature)[101], so it is no surprise that the hysteresis loops preserve their main features at both room temperature and low temperature. The 36 nm layer shows cubic magnetocrystalline anisotropy, as expected from the cubic crystal structure of Fe_3Si and previously reported in literature[64,79]. The easy magnetization axis is along the [010] direction and both [110] and [$\bar{1}$10] are equivalent hard axes. The coercivity along all three directions is higher at 10 K, accompanied by slightly rounded magnetization reversals. This is also expected from the higher energy required to flip the spins at low temperatures. At both 10 and 300 K, the magnetic switching is nonetheless very abrupt (within 1-2 Oe), and reflects the monolithic behavior of the high quality single crystalline film.

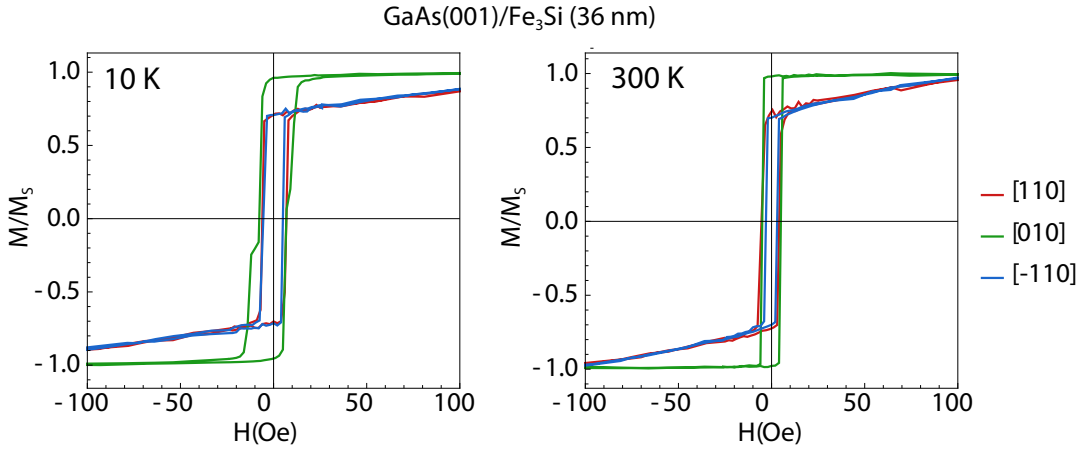

Figure 4.22: Magnetization of a 36 nm Fe_3Si film along the [110], [010] and [$\bar{1}$10] at 10 K and 300 K

4.4.3 Influence of amorphous Ge and crystalline $FeGe_2$

The magnetic behavior of isolated Fe_3Si films is relatively well understood. However, the picture can gain in complexity if the material is included within heterojunctions such as those created in the context of this study. The next step of the investigation of the magnetic properties of the layer stacks is to compare the hysteresis curves of Fe_3Si with those of a sample on which an amorphous 4 nm Ge layer was deposited, as well as with a sample on which $FeGe_2$ was formed through SPE. Those measurements, all taken at 10 K, are brought together in Fig. 4.23. In panel (a), the curves of pure Fe_3Si are shown again, but with each orientation plotted independently to facilitate the comparison. The placement and color code introduced in this figure will remain the same for the subsequent data: from left to right are the [110] (red), [010] (green) and [$\bar{1}$10] (blue) orientations of the samples. In (b), a 4 nm layer of amorphous Ge was deposited on top of the Fe_3Si film at 150°. Then, panel (c) shows a $Fe_3Si/FeGe_2$ (36/4) nm bilayer obtained by annealing the amorphous Ge (240°C).

As seen in (b), the presence of amorphous Ge on Fe_3Si already introduces changes in the magnetic features. The low deposition temperature leaves the Fe_3Si film intact, which means the the magnetic properties of the 'bulk' film should remain unchanged. However, the reduced coercivity along the [$\bar{1}$10] direction could originate from a perturbation of the spins at the Fe_3Si/Ge interface. Normally, single Fe_3Si thin films have an anisotropy contribution from the atoms found at the surface (eq. 2.11). The smaller number of nearest neighbors for those atoms increases the local density of states. This increases the chances of the Stoner criterion being be satisfied, meaning that magnetic ordering is more likely.[80] The presence of amorphous Ge reintroduces neighbors to the atoms on the Fe_3Si surface, which could counteract the magnetic ordering of the naked Fe_3Si film and reduce the coercivity. With that said, the effect is only present along the [$\bar{1}$10] direction (blue curve), but not along the [110] direction. This observation suggests that the interfacial effect emerging between Fe_3Si and Ge does not share the same cubic anisotropy. Furthermore, the presence of 'lobes' along the [$\bar{1}$10] also indicates that there is a secondary hysteresis superimposed over that of Fe_3Si, as if an inde-

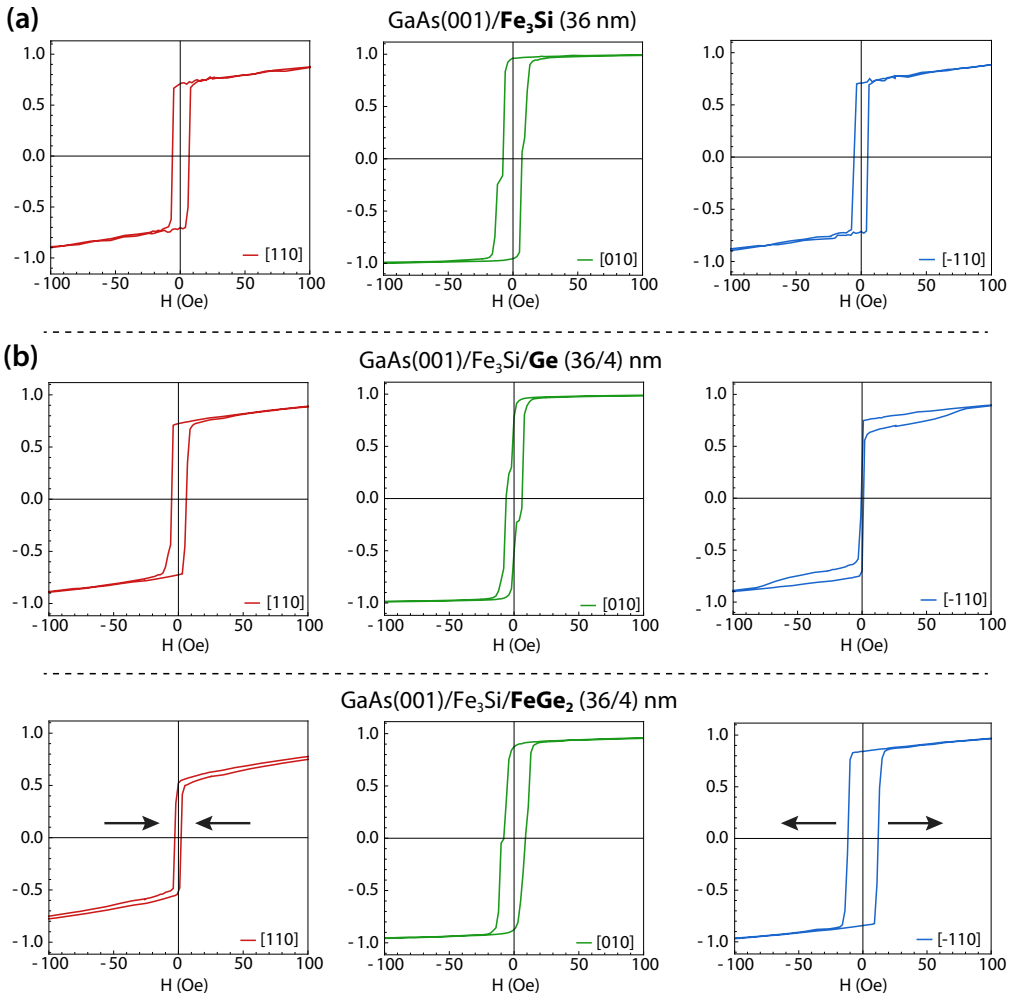

Figure 4.23: Effect of adding 4 nm of amorphous Ge and 4 nm of crystalline $FeGe_2$ on the magnetization of 36 nm Fe_3Si at 10 K along the [110], [010] and [$\bar{1}$10] orientations at 10 K. (a) Magnetization curves of 36 nm Fe_3Si. (b)Magnetization curves of Fe_3Si/Ge (36/4) nm. (c) Magnetization curves of $Fe_3Si/FeGe_2$ (36/4) nm.

pendent FM compound existed at the interface exhibiting uniaxial magnetic anisotropy. This could be the case if we assume the the first Ge atoms deposited at 150°already have enough energy to start forming and intermediary compound (in this case likely $FeGe_2$), even before properly annealing.

The presence of the $FeGe_2$ film, then, contributes quite drastically to the hysteresis curves shown in (c). The coercivity of the layer stack is decreased from 10 Oe to 5 Oe in the [110] direction, remained stable in the [010] direction, while it increased from approximately 10 Oe to 15 Oe along [$\bar{1}$10] direction. There is no distinctive independent switching for the Fe_3Si and $FeGe_2$ layers. In other words, their magnetic behavior is connected: the two films flip their magnetization in a single sharp step along all three orientations. The combined coercivity of Fe_3Si and $FeGe_2$ greater in the [$\bar{1}$10] direction, and reduced along the perpendicular [110]

direction. This effect could either come from the the $Fe_3Si/FeGe_2$ interface itself, and/or from the additional contribution of the $FeGe_2$ film to the magnetization.

The bonds at the interface are fundamentally different from those found in the bulk crystalline structure of the two thin films. The change in coercivity can be caused by interfacial effects where the spins present in the Fe_3Si layer are interacting with the spins found in the $FeGe_2$ layer, in such a way as to make the whole stack require more energy to reverse its magnetization in the $[\bar{1}10]$ direction, and less energy in the [110] direction (as explained above in case of the amorphous Ge). Another reasonable hypothesis is that $FeGe_2$ is *also* ferromagnetic. In this case, the opposite behavior of the interaction between the two layers in the [110] and $[\bar{1}10]$ depicts uniaxial magnetocrystalline anisotropy, where the hard and easy axes are 90°apart and intermediate axis in the [010] direction. Uniaxial anisotropy is normally observed in ultra-thin FM layers, for which contributions from the interfaces play a dominant role in the magnetization. Since the underlying 36 nm Fe_3Si was shown to have cubic anisotropy in Fig. 4.22, such shifts in coercivity must originate from the presence of $FeGe_2$. Also, the TEM images of the stacks grown using the SPE approach show that the annealing of Ge preserves the structural quality of the underlying Fe_3Si (this is related to the slow diffusion-controlled synthesis of $FeGe_2$). Apart from the properties of the interface, one can therefore expect that the magnetic behavior of the Fe_3Si film remains unaltered[92], which supports the hypothesis that $FeGe_2$ contributes itself to the combined magnetization.

4.4.4 Trilayers and influence of $FeGe_2$ thickness

To obtain a complete picture of the magnetization in the devices we ultimately aim to create, measurements were then conducted on $Fe_3Si/FeGe_2/Fe_3Si$ trilayers. We have shown previously that the thickness of the $FeGe_2$ buffer layer can be controlled within a certain range. It can then be interesting to investigate whether the $FeGe_2$ film thickness has an influence on the global magnetic behavior of the trilayer stacks. The trilayer samples containing different $FeGe_2$ thicknesses (used for the XRD shown in Fig. 4.10) were thus measured by SQUID. The results are compiled in Fig. 4.24, which compares in (a) a $Fe_3Si/FeGe_2$ (36/6) nm bilayer (shown for reference) with, in (b), trilayers having a 4, 6, and 8 nm $FeGe_2$ interlayer.

First, let us compare the $Fe_3Si/FeGe_2$ plots shown in Fig. 4.24 (a) with the ones shown in the previous Fig. 4.23 (c). The only difference between those two samples is the thickness of the $FeGe_2$ capping layer: 4 nm in the first sample, 6 nm in the second. The effect of these extra 2 nm can be seen quite strikingly along the [010] direction, where intermediate 'steps' appear through the main magnetization reversal along both directions of the loop. The steps are symmetrical and have identical linear slope. Such a linear dependence on H is usually attributed to paramagnetism, which as we know, cannot come from the underlying Fe_3Si film, and rather reflects a property of $FeGe_2$. This assertion will be confirmed in the next chapter through remanence measurements of an isolated $FeGe_2$ film, which undergoes a ferromagnetic-paramagnetic transition at 10 K. Those steps are not visible in the (36/4) nm sample, and thus originate from the thicker $FeGe_2$ contribution (and not the interface). The [010] orientation seems to favor the appearance of the $FeGe_2$ paramagnetic steps in all sam-

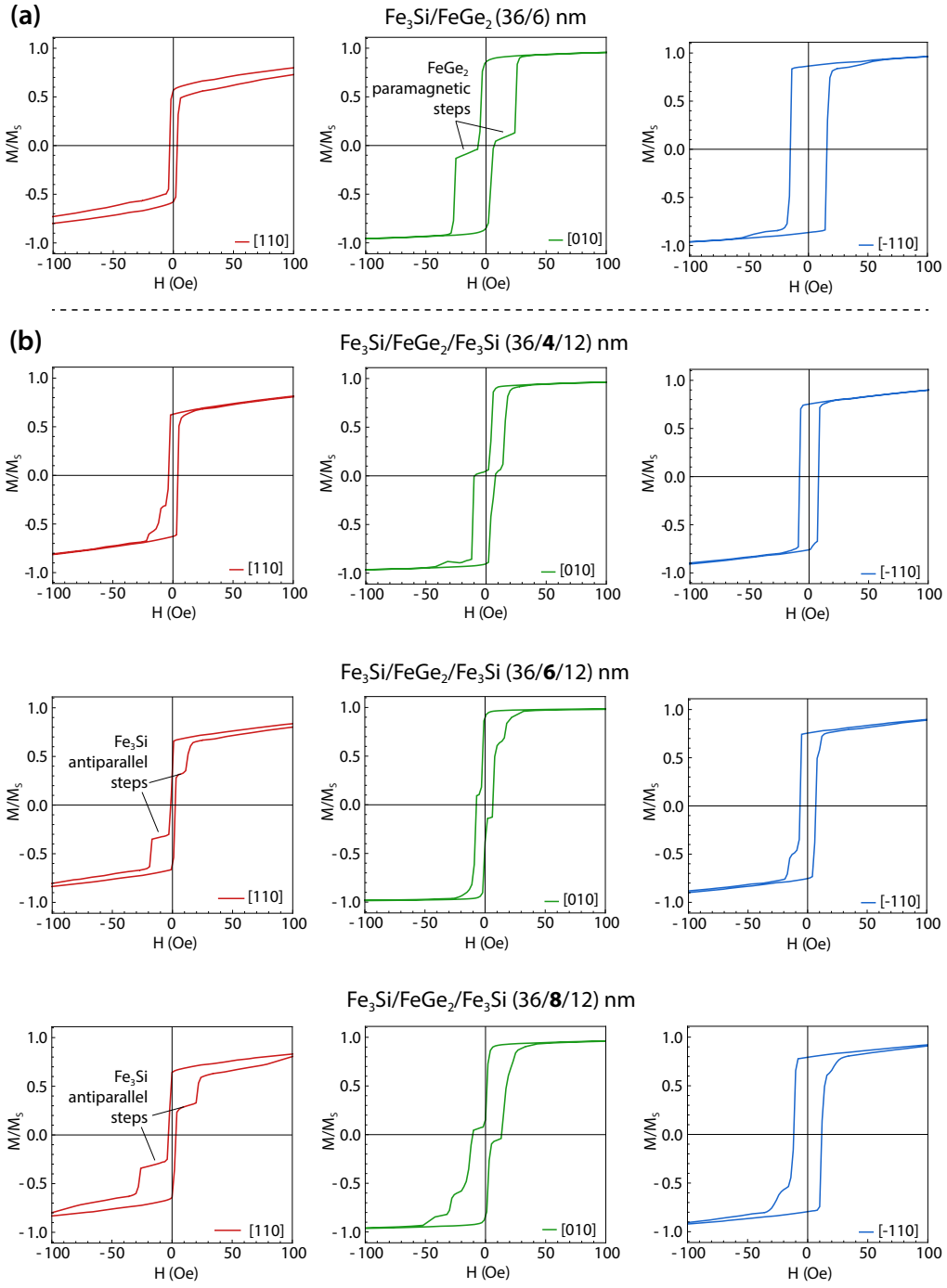

Figure 4.24: (a) 10 K magnetization curves of a $Fe_3Si/FeGe_2$ (36/6) nm bilayer (b) Magnetization curves for three $Fe_3Si/FeGe_2/Fe_3Si$ trilayers with different $FeGe_2$ thicknesses. Independent switching the the 36 nm and 12 nm Fe_3Si films can be seen along the [110] direction in the samples with 6 nm and 8 nm $FeGe_2$.

ples, and again suggest that it is the $FeGe_2$ intermediate axis (easiest being $[\bar{1}10]$ and hardest being [110]). The aforementioned uniaxial effect of the $FeGe_2$ is still observed along the [110]

and further amplified [$\bar{1}10$] directions, where the coercivity of the stack increases to 20 Oe. The thicker film thus establishes a clear trend in the [$\bar{1}10$] direction.

Finally, the growth of a capping 12 nm Fe_3Si layer introduces additional features in the magnetization of the thin film stacks, some of which are of great importance to operate the layer stacks as MTJs. Mainly, a step-like intermediary transitions before and during the magnetic switching of the trilayer sample. Some smaller features can also be observed, but are more difficult to interpret, especially those seen along the [010] and [$\bar{1}10$] directions, as they could result from pinning of small domains and other irreproducible effects that are unique to the nanoscopic structure of the $Fe_3Si/FeGe_2$ interfaces in each samples. However, there is a consistent step-like switching effect along the [110] direction (red curve), as seen in the samples with 6 nm and 8 nm $FeGe_2$. Of paramount importance, those two specific steps are attributed to the fully independent magnetization of the 36 nm and 12 nm Fe_3Si layers enabled by the sufficiently thick (>4 nm) $FeGe_2$ buffer layer itself aligned along its hard magnetization axis.

As discussed before, the coercivity increases following the thickness of the $FeGe_2$ buffer layer along the [$\bar{1}10$] orientation, also in the trilayer stacks. However, along this direction, one can observe that the $Fe_3Si/FeGe_2$ (36/6) nm bilayer has higher coercivity than the (36/6/12) nm trilayer. This is explained by the presence of the top Fe_3Si, which counteracts the contribution from the $FeGe_2$ film by modifying the atomic bounds at the second interface and reducing the anisotropy.

4.4.5 Trilayers with combination of Fe_3Si and Co_2FeSi

It is at this point relevant to compare the magnetic behavior of the trilayer stacks in which a combination of Fe_3Si and Co_2FeSi was used. In this part of the investigation, the magnetization curve of the $Fe_3Si/FeGe_2/Fe_3Si$ (36/6/12) nm trilayer stacks is reproduced and compared to the magnetization curve of the $Fe_3Si/FeGe_2/Co_2FeSi$ (36/6/12) nm sample. The two can be seen together in Fig. 4.25.

The results show that the magnetic behavior of the two samples is very similar along all three orientations. This is encouraging since it shows that the fabrication of our sample is highly reproducible, with the features observed being recognized in both trilayer stacks. However, the intention behind using Fe_3Si and Co_2FeSi was to exacerbate the difference in energy required to switch each FM film (Co_2FeSi has higher coercivity), which would yield clearer plateaus of antiparallel magnetization states. This effect, rather than relying on the choice of materials used, seems to strictly depend on the direction of external H field pointing along the [110] direction. Given our previous observations regarding the contribution of the $FeGe_2$ buffer layer to the total magnetization, the appearance of these plateaus is likely enabled by the fact that $FeGe_2$ has a uniaxial magnetocrystalline anisotropy with hardest axis along the [110] direction, which effectively isolates the magnetic behavior of the two FM films.

The magnetization hysteresis curves along the [110] direction for both hybrid trilayers are reproduced in Fig. 4.26 with some elements guiding the magnetization reversal process. In both (a) and (b), the loops contain a similar intermediary step, which has a magnitude exactly

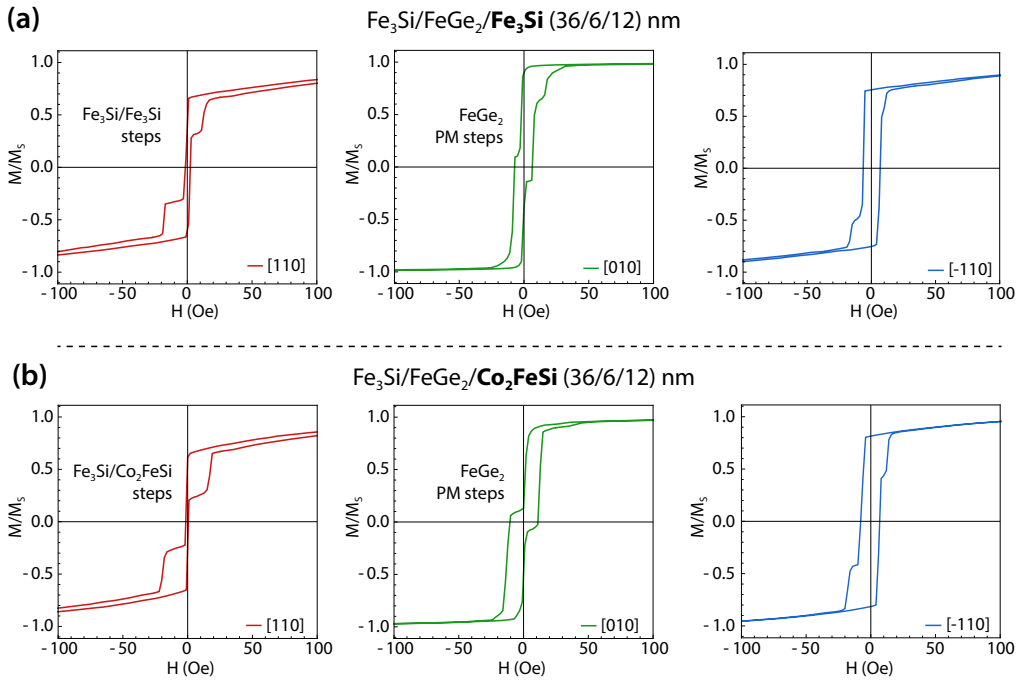

Figure 4.25: (a) $Fe_3Si/FeGe_2/Fe_3Si$ (36/6/12) nm hysteresis loop along all principal directions. (b) $Fe_3Si/FeGe_2/Co_2FeSi$ (36/6/12) nm hysteresis loop along all principal directions. The paramagnetic (PM) steps of the $FeGe_2$ are seen along its easy axis [010], while the FM films steps are visible along its hard axis [110].

$1/4^{th}$ of the total magnetization reversal amplitude. This ratio can be directly associated to the respective thicknesses of the two Fe_3Si films. The 36 nm film, being three times as thick as the 12 nm film, accounts for $3/4^{th}$ of the reversal amplitude. The effect is comparable but not quantitatively the same in (b), as the absolute magnetization of the 12 nm Co_2FeSi is higher than that of a 12 nm Fe_3Si film. The step associated with switching the Co_2FeSi is slightly bigger, accounting for approximately $1/3^{rd}$ of the magnetization reversal despite representing only $1/4^{th}$ of the thickness, which yields a magnetization per unit cell $\sim$8.3% larger than that of Fe_3Si.

At high positive magnetization ①, both layers are aligned along the same orientation. As the field is decreased passed 0, the thicker FM film flips and the stack reaches a plateau of antiparallel magnetization ②. A slightly stronger negative field eventually flips the thinner film, and both are oriented along the same direction again ③. On the other side of the hysteresis loop, the reversal proceeds in a similar way, reaching another antiparallel magnetization configuration ④. Returning to large positive field brings the system back to the start of the loop ①.

4.4.6 Effect of temperature on trilayers

Lastly, it is worth discussing the effect of temperature of the magnetic switching the trilayers. The $Fe_3Si/FeGe_2/Fe_3Si$ (36/6/12) nm sample is taken as an example, shown in Fig. 4.27.

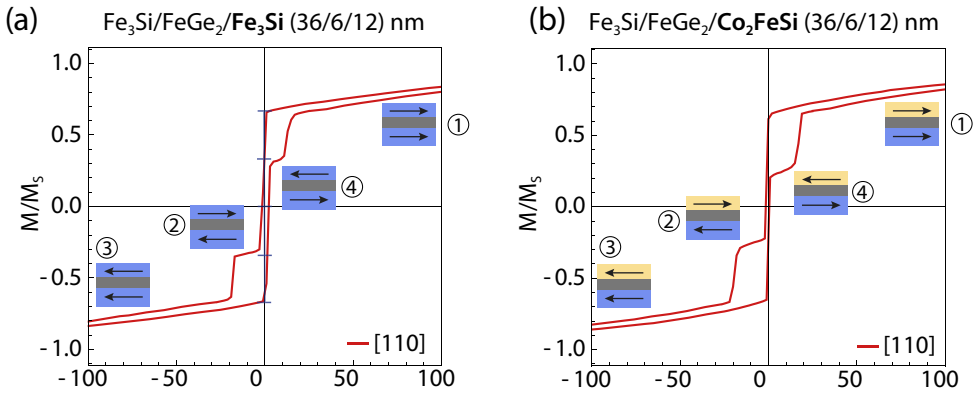

Figure 4.26: (a) $Fe_3Si/FeGe_2/Fe_3Si$ (36/6/12) nm hysteresis loop along the [110] direction showing plateaus of antiparallel magnetization. (b) $Fe_3Si/FeGe_2/Co_2FeSi$ (36/6/12) nm hysteresis loop showing the same effect.

The antiparallel magnetization plateaus disappear completely at room temperature, and the hysteresis loops resemble those measured for the single Fe_3Si film. This effect is explained by a temperature-dependent magnetic ordering in the $FeGe_2$ interlayer. SQUID measurements on thicker and 'isolated' $FeGe_2$ films (presented in the following chapter) suggest that the material loses its ferromagnetic character above 10 K. Assuming that the effective separation of both Fe_3Si films relies on the $FeGe_2$ being magnetized along its hard magnetization axis ([110]) means that the antiparallel magnetization plateaus can only be detected in the SQUID at temperatures below 10 K.

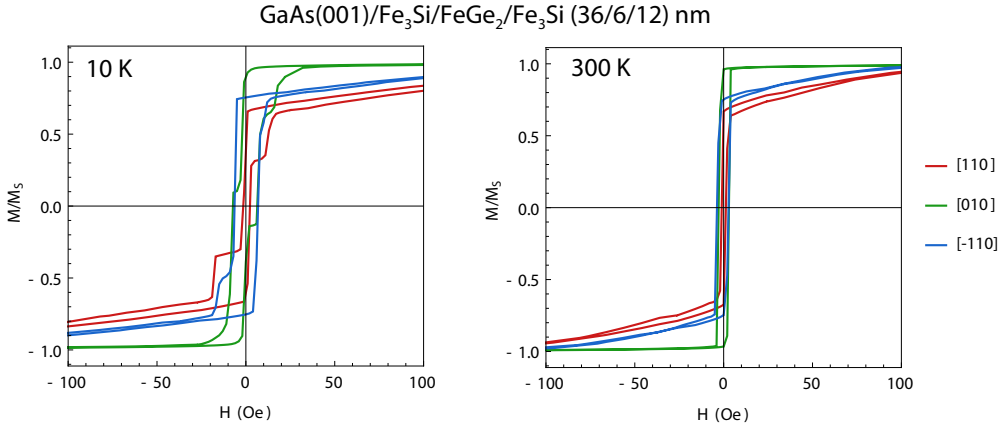

Figure 4.27: Hysteresis loop of a $Fe_3Si/FeGe_2/Fe_3Si$ (36/6/12) nm trilayer at 10 K and 300 K. All layers of the stack switch magnetization direction together at room temperature.

4.5 Vertical spin valve measurements

The growth of trilayers involving Fe_3Si, $FeGe_2$ and Co_2FeSi represents an important experimental achievement, thanks to the development of the SPE approach successful in crystallizing thin amorphous Ge. In addition, the observation by SQUID magnetometry of an independent magnetization switching of the FM layers (Fe_3Si and/or Co_2FeSi) indicates that the films can be magnetically decoupled by the insertion of a thin $FeGe_2$ film. Ultimately, an observation of the spin valve effect via direct measurement of the magnetoresistance across the trilayers would confirm that $FeGe_2$ can act as a barrier supporting spin-selective injection between the two FM films, and therefore constitutes another critical step towards the realization of the SS-SBTT. The spin valve measurements presented in this section were made in tight collaboration with D. Czubak, and constitute a preliminary exploration of the vertical transport effects across the heterojunctions. (A detailed investigation is discussed elsewhere[102], we focus here on the very possibility to observe the spin valve signals required for the SS-SBTT.)

4.5.1 Buffer layer thickness effect on signal valve amplitude

As previously stated and illustrated in Fig. 4.10, it was possible to produce $Fe_3Si/FeGe_2/Fe_3Si$ trilayer samples with $FeGe_2$ interstitial films having a thickness of 4, 6 or 8 nm. In those three samples, the bottom and top Fe_3Si layers are respectively 36 nm and 12 nm thin, as usual. Identical spin valve devices were first created using those three layer stack combinations (see Fig. 3.8) and measured in the *Oxford Instruments* cryostat depicted in Fig. 3.11 (a) at room temperature. An in-plane external magnetic field was applied in a range going from +40 mT to -40 mT (analogous to $\pm$400 Oe). A DC current of 1 mA is passed across the trilayer junctions, and the voltage is measured using a 3-terminal configuration as described in the methods section.

Fig. 4.28 shows the magnetoresistance percentage (MR%, see eq. 2.5) as the magnetic field is swept back and forth in the three spin valve devices. The most striking result visible in these curves is that spin valve signals are indeed measured in all three samples. In other words, the resistance of the electrons flowing from the first Fe_3Si layer to the second Fe_3Si layer depends on the relative orientation of the magnetization of the two FM films. Although the signals observed indicate spin selectivity, these measurements alone cannot conclude that the transport proceeds via tunneling. Nonetheless, these first observations constitute a determining proof of concept for the realization of the SS-SBTT.

The spin valve signals measured in these samples are consistent with the SQUID measurements shown in Fig. 4.26 (a) and Fig. 4.26(a). Indeed, a plateau was observed confirming the existence of an antiparallel magnetization of the 36 nm and 12 nm Fe_3Si films. This plateau occurred around 10 Oe, which can be associated with the high MR peaks happening for fields $<$5 mT (corresponding to values$<$ 50 Oe). The broadening of the high resistance peaks, especially for the thicker $FeGe_2$, suggests that the switching of the Fe_3Si magnetization orientation is not as sharp. Since the spin valve measurements were done at room temperature, it is harder to reconcile our observations with the room temperature SQUID measurements which

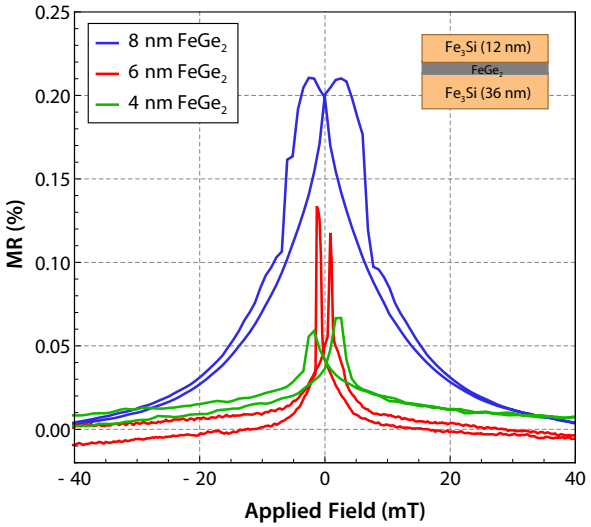

Figure 4.28: $FeGe_2$ thickness dependence of spin valve signal amplitude measured in three $Fe_3Si/FeGe_2/Fe_3Si$ samples. As the $FeGe_2$ buffer is made thicker, the MR % increases by a factor of 4, from 0.05% to 0.20%.

are not showing clear plateaus of antiparallel magnetization (Fig. 4.27 (b)). This could be explained by the geometry of the samples, which is drastically different in the SQUID versus spin valve experiments. For SQUID measurements, the trilayer samples and macroscopic pieces of wafer, and the two Fe_3Si films have exactly the same surface area. The processing of the spin valve devices removes almost entirely the upper Fe_3Si film, restricting it to a 1×1 μm^2 contact pad. It is known that the dimensions of thin film sample can have an effect on its coercivity, usually increasing it and broadening the magnetic switching due to a more significant contribution from edge effects compared to the bulk film behavior. This geometric factor could, in the spin valve devices, introduce an extra difference in coercivity between the bottom and top FM layers, hence revealing the room temperature signals shown above.

The measured magnetoresistance values are *very* small for such MTJ-like structures, especially considering that Fe_3Si is expected to have a polarization of 45%.[51] In theory, this could yield a TMR ratio up to 32.9% (as per eq. 2.7). The magnitude of the MR% could be strongly attenuated as the spins are *diffused* through the $FeGe_2$ buffer layer, as opposed to transported via tunneling. It is probable that the spin valves work via spin-selective diffusion of charges, or possibly thermionic emission over very small Schottky barriers emerging at the $Fe_3Si/FeGe_2$ interfaces. Indeed, the trend in the signal amplitude suggests that the presence of a thicker $FeGe_2$ buffer layer *intensifies* the spin valve signal. In other terms, a thick $FeGe_2$ layer increases the MR% measured in the antiparallel states of the FM electrodes. Such a behavior has been reported before and is consistent with the presence of a metallic barrier.[102] Further investigations should be made in order to learn more about the limits of this effect by inserting even thicker $FeGe_2$ buffer layers. This idea remains an experimental challenge, and would require further adjustments of the SPE approach. Importantly, these results do not

rule out the possibility to operate a SS-SBTT as intended based on such $Fe_3Si/FeGe_2/Fe_3Si$ heterostructures.

4.5.2 Spin valves involving Fe_3Si and Co_2FeSi layers

Another set of trilayer samples, this time involving both Fe_3Si and Co_2FeSi, were also used to investigate spin valve effects. The measurements, made at 300 K, are shown in Fig. 4.29. The red curve corresponds to a sample that was discussed above, with $Fe_3Si/FeGe_2/Fe_3Si$ layers being (36/6/12) nm thick. The blue curve shares the same layer thicknesses, however the top film is Co_2FeSi. In the green curve, the $FeGe_2$ buffer layer is replaced by a 2 nm MgO film, shown as reference.

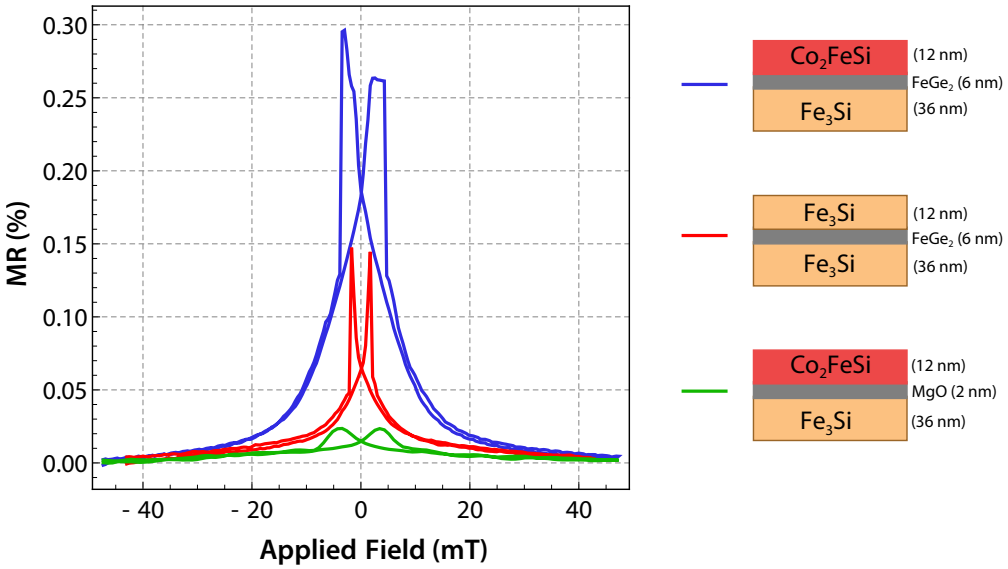

Figure 4.29: Room temperature spin valve signals using three samples in which the FM films consist of either Fe_3Si or Co_2FeSi. The green curve uses MgO as a buffer layer instead of $FeGe_2$.

Here again, a spin valve signal could be observed in all samples. However, the MR% is higher when using a combination of Fe_3Si and Co_2FeSi separated by a $FeGe_2$ layer. As expected from the higher polarization of Co_2FeSi, the spins transported from the Fe_3Si dispose of a lower number of available states in the antiparallel magnetization configuration, which translates into a higher magnetoresistance. Using such samples visibly offers advantages for practical applications, given that the high and low resistance states are more easily differentiated.

The sample using MgO as a barrier shows the lowest MR%. In this case, the 2 nm thin fully insulating MgO layer effectively acts as a tunnel barrier. However, the growth of Co_2FeSi over MgO does not yield a film quality comparable to that of the samples obtained using the SPE approach. The top Co_2FeSi film is polycrystalline, meaning that its magnetic switching is not

as sharp and 'monolithic'. The parallel and antiparallel magnetization states of the Fe_3Si and Co_2FeSi are therefore not as clear, which results in a smaller difference in magnetoresistance.

4.5.3 Temperature dependence of the spin valve effect

The spin valve signals shown previously were all measured at 300 K. However, as for the SQUID measurements, it is interesting to compare the amplitude of the MR% as a function of temperature. For this part of the investigation, a single spin valve device made from the $Fe_3Si/FeGe_2/Co_2FeSi$ (36/6/12) nm layer stack was measured while cooling down. In Fig. 4.30, the external magnetic field is swept as previously, and the resulting spin valve signals are shown taken at 300 K (blue) and 20 K (grey). Visibly, the decrease in temperature drastically affects the amplitude of the MR%, bringing it from 0.27% to a mere 0.06%.

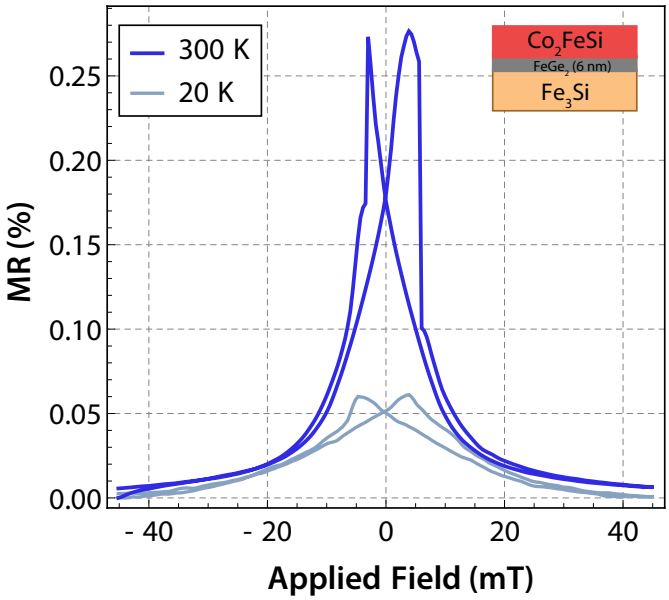

Figure 4.30: 300 K (blue) and 20 K (grey) spin valve signals measured in the same device made using a $Fe_3Si/FeGe_2/Co_2FeSi$ (36/6/12) nm trilayer stack. Low temperatures reduce the amplitude of the magnetoresistance in the sample.

This result is at first surprising. Indeed, one should expect the MR% to increase as the temperature is lowered, in case the transport of spins occurs via thermionic emission (eq. 2.3) or tunneling (record high TMR are measured at low temperature[27]). The perceived barrier height is harder to overcome for charges transported from the Fe_3Si layer to the Co_2FeSi, which should accentuate the difference is resistance between the parallel and antiparallel magnetization states. This observation once again suggests that transport via the $FeGe_2$ layer is in fact metallic, i.e. the potential barrier caused by $FeGe_2$ is vanishingly small. Furthermore, we have evidence that the polarization of Co_2FeSi and other Heusler alloys increases at low temperature.[44] In those specific spin valve devices, however, the decrease in MR at

low temperature is likely exacerbated by a transition towards ferromagnetism of the $FeGe_2$ buffer layer film[102], as suggested from the prior SQUID magnetometry. The fact that $FeGe_2$ becomes FM at low temperature does not prevent the SQUID measurements to show clear plateaus of antiparallel magnetization between the Fe_3Si and/or Co_2FeSi. However, a FM buffer layer drastically affects vertical transport. The presence of magnetism in the $FeGe_2$ layer is visibly detrimental to the spin valves, owing to the contribution of spin-spin interactions during transport. This effect is indeed problematic at low temperature, however most applications would only require devices to be usable at room temperature. Once again, the use of $Fe_3Si/FeGe_2/Co_2FeSi$ trilayers remains possible in order to operate the SS-SBTT as intended.

4.6 Summary

This chapter has presented the work done to grow and characterize high quality, fully crystalline and lattice-matched hybrid trilayers. The SPE approach was proven successful, insofar as a fully crystalline Ge-rich compound could be obtained by annealing over metallic Heusler alloys. Four variations of such trilayers were grown, using combinations of Fe_3Si and Co_2FeSi. The crystallization of amorphous Ge over Fe_3Si yields the new layered compound $FeGe_2$, while a different crystalline compound Ge(Co,Fe,Si) forms over Co_2FeSi. The synthesis of $FeGe_2$ over Fe_3Si is a surprisingly consistent process which preserves the quality of the underlying metallic layer while providing atomically flat interfaces. SQUID measurements have shown that some trilayers can exhibit independent switching of the two FM layer along the [110] direction, at low temperature and with sufficiently thick $FeGe_2$ interlayer. This result is encouraging, and constitute an significant step towards the realization of spintronic devices, in particular the SS-SBTT. Importantly, spin valve devices fabricated using different trilayer configurations were measured at low and room temperature. In all cases presented here, a spin valve signal could be measured. Thus, the transport of charges between Fe_3Si and Co_2FeSi through $FeGe_2$ can be considered spin selective. These measurements establish the trilayer stacks created throughout this investigation as adequate candidate to eventually fabricate a SS-SBTT.

Despite the success of the SPE approach and spin valve measurements, an important aspect has yet to be clarified: what are the properties of the new layered $FeGe_2$ compound we obtained? The original SS-SBTT device concept required Schottky barriers to form at the FM/SC interface, and take advantage of those to achieve efficient spin injection. Irregardless of the properties of $FeGe_2$, i.e. whether it is a SC or not, it was shown possible to implement a device that could possibly work as the original SS-SBTT intends to. In the following chapter, experiments will reveal further information about the properties of isolated $FeGe_2$ thin films.

5 A STUDY OF ISOLATED $FeGe_2$ THIN FILMS

5.1 Motivation

This chapter will present and discuss the results from our investigation of the layered $FeGe_2$ with space group *P4mm* obtained unexpectedly during the annealing of amorphous Ge over Fe_3Si epitaxial surfaces. This specific polymorph is new, to our knowledge, and has not been described previously in literature.[1] The layered structure of the $FeGe_2$ films is however similar to previously reported α-$FeSi_2$ thin films (*P4/mmm*).[103,104] Furthermore, due to the method used to produce $FeGe_2$, i.e. by annealing Ge over Fe_3Si, the resulting compound is suspected to contain up to 17% Si. Those Si atoms occupy Ge sites, meaning that the films depicted in this thesis are in fact a hybrid between $FeGe_2$ and α-$FeSi_2$. The electrical and magnetic properties of the $FeGe_2$ found in our trilayer samples are therefore expected to resemble those of α-$FeSi_2$. ($FeGe_2$ has been and will be systematically used to refer to the Si-doped *P4mm* polymorph.) Another $FeGe_2$ structure with space group *I4/mcm* exists[105], whose magnetic properties were studied recently[106], as well as in the form of nanowires.[107] A distinction will be made if this other phase is mentioned.

The solid-phase epitaxy of Ge over Fe_3Si provided a solution to grow the lattice-matched trilayers treated in the previous chapter. However, a number of questions came up as the presence of $FeGe_2$ was discovered. Importantly, is the material a semiconductor, and/or can it serve as an effective tunnel barrier separating two FM layers, as required to realize a SS-SBTT? We have shown through the spin valve measurements presented previously that $FeGe_2$ can indeed be used as a buffer layer supporting spin selective transport. The structural properties of $FeGe_2$, mainly studied by XRD and TEM, could be probed while the film was still sitting within the $Fe_3Si/FeGe_2/Fe_3Si$ trilayer stacks. However, electrical transport (and, to some extent, magnetization) measurements can only be attempted on 'bare' $FeGe_2$ thin films, otherwise the properties of the adjacent FM layers would dominate. The isolation of $FeGe_2$ constitutes a totally new challenge, coming with an additional set of constraints. Our efforts to isolate $FeGe_2$ thin films will be presented here, along with results shedding light on the electrical and magnetic properties of the new material.

[1] First mention of *P4mm* $FeGe_2$ in Jenichen et al. (2018)[100], from which some of the results also appear in this thesis.

5.1.1 Related compounds in the Fe-Ge-Si system

The combination of group IV semiconductors and ferromagnetic metals has been investigated by groups belonging to a wide range of fields in solid-state physics, with aim being to study and exploit non-trivial magnetic ordering effects taking place within reach of the semiconductor industry paradigm. The quest for room temperature ferromagnetic semiconductors remains an ongoing challenge in materials science, as they would constitute an important building block for applications in spintronics.[108] In that context, diverse combinations of Fe, Ge and Si were studied in the past, forming a promising materials system in which magnetism and semiconductivity could coexist, and generally expanding the set of compounds compatible with silicon-based microelectronics.

In the 1990's, the semiconducting orthorhombic phase of iron disilicide (β-$FeSi_2$) has been considered as a candidate for optoelectronic communication.[109] It has a direct band gap $E_g = 0.87$ eV. It is then possible to imagine substituting the Si atoms by Ge, while preserving the integrity of the crystalline structure. The Ge-Si-Fe system has indeed been explored, for example by creating β-$FeSi_{2-x}Ge_x$ (x=0.08).[109] This material has a direct band gap of 0.83 eV, indicating a red shift compared to that of β-$FeSi_2$ thin films, and thereby a possible tunability of the semiconductor's properties. Previously studied α-$FeSi_2$ is described as a metastable compound (as opposed to the β phase having a stable orthorhombic structure).[104] 50 nm thin films were formed along the (111) orientation on a Si(001) surface by means of pulsed laser deposition. Measurements on α-$FeSi_2$ have shown that the material exhibits nonmetallic ferromagnetism, while the bulk films have opposite metallic and nonmagnetic characteristics. These investigations are already useful to predict what to expect from the $FeGe_2$ thin films (with up to 17% Si atoms) obtained via our SPE approach, and suggest that the material could be a semiconductor.

5.2 Electrical and magnetic measurements

The experimental and theoretical results (TEM, XRD) presented in the previous chapter were conducted on samples in which the $FeGe_2$ was embedded between two Fe_3Si layers. This approach was successful in revealing the *structure* of the new material. However, a direct investigation of the electrical properties of $FeGe_2$ cannot be undertaken while the film remains in contact with an underlying metallic substance. Any electrical contacts made on the thin films would necessarily also probe the thicker Fe_3Si layer, in which case the contribution from $FeGe_2$ would be undetectable.

5.2.1 Film isolation

Knowing the stoichiometry of $FeGe_2$ (more precisely $Fe(Ge_{0.83}Si_{0.17})_2$), we can determine exactly the ratio of crystalline Fe_3Si to amorphous Ge required to achieve a complete intermixing of the two films. By performing solid-phase epitaxy as usually with a thinner Fe_3Si underlayer, we can hope to eliminate all residual Fe_3Si and obtain a single $FeGe_2$ layer sitting on the

GaAs substrate. This idea is illustrated schematically in Fig. 5.1. As explained previously, the thickness of the film is controlled by calibrating the growth rate (in nm/h), which is achieved by measuring the XRD finite thickness oscillations produced by the films once out of the MBE system (the shutters are left opened for a given time, and the resulting thickness is measured afterwards). The growth rate of *amorphous* Ge extracted from the calibration of crystalline samples, i.e. Ge was grown epitaxially on GaAs, otherwise the X-rays could not produce any diffraction peaks. We now need to convert the number of atoms per formula into a more convenient ratio of film thicknesses.

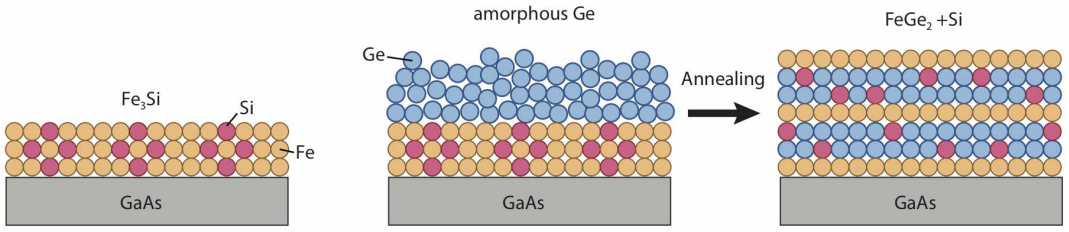

Figure 5.1: Solid phase epitaxy approach adapted to obtain a 'pure' $FeGe_2$ layers on GaAs. By calculating the exact ratio of Fe, Si, and Ge atoms required, we can achieve a complete intermixing which would result in $FeGe_2$ with 17% Si atoms substituting Ge.

To determine the effective film thickness ratio required to obtain the right stoichiometry for $FeGe_2$, we count the atoms contained in a 'monolayer' of each material. The unit cells of Fe_3Si and Ge are illustrated in Fig. 5.2, each measuring respectively 5.5655 Å and 5.5658 Å. The small lattice mismatch is negligible for thicknesses in the range we are investigating here.

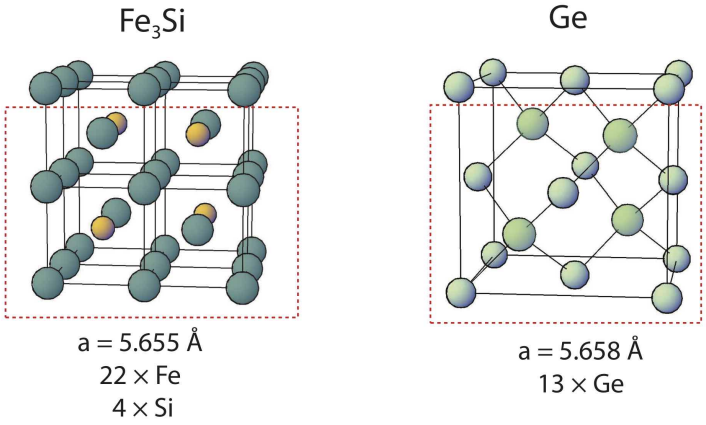

Figure 5.2: The Fe_3Si and Ge cubic structures, which per 'monolayer' contain 22 Fe, 4 Si and 13 Ge atoms. Assuming that all Si occupy Ge lattice sites in the $FeGe_2$ film, the effective thickness ratio between Fe_3Si and Ge is 1:3.08.

To avoid double counting for each unit cell, we consider only the atoms below the red dotted line: Fe_3Si contains 22 Fe atoms and 4 Si atoms, while an equivalent Ge thickness contains 13 atoms. The condition to respect the stoichiometry is thus to have in total 22 Fe

+ 4 Si + $n\cdot$ Ge. However, Si and Ge combined together should be twice the number of Fe atoms, so $4 + n = 2 \cdot 22 = 44 \rightarrow n = 40$. Each monolayer of Fe_3Si requires 40 Ge atoms, which translates into a thickness of $40/13 = 3.08$ Ge monolayers. Therefore, in terms of film thickness uniquely, a ratio of 1:3.08 of Fe_3Si and Ge should combine into a pure $FeGe_2$ layer where all Si atoms are sitting on Ge sites.

Based on the thickness ratio argument presented above, a number of samples were grown and annealed using MBE and the SPE method described in the previous chapters. The goal, however, is to achieve a complete intermixing between the Fe_3Si and Ge upon annealing. There is no upper limit found to the distance traveled via diffusion by the Fe and Si atoms into the Ge film. Still, the thickness of the films should remain as small as possible to maximize our chances of obtaining a pure and well ordered $FeGe_2$ film.

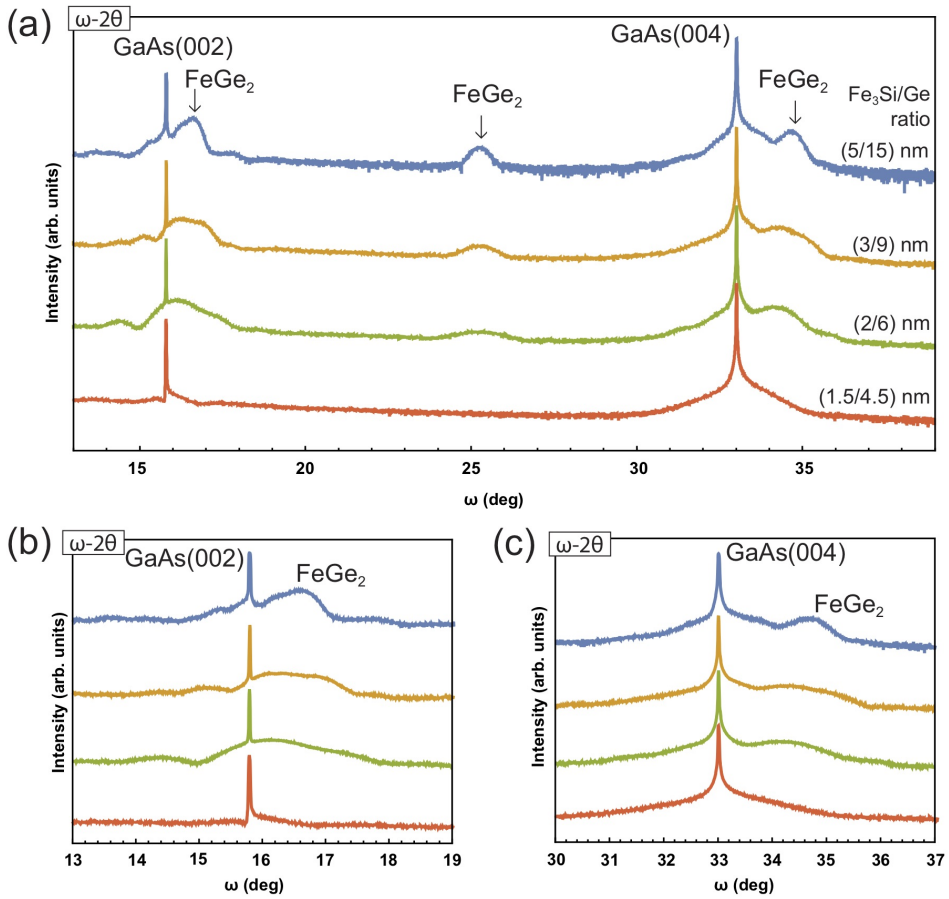

Figure 5.3: (a) XRD curves for samples consisting of different nominal $FeGe_2$ films. The samples are formed by annealing amorphous Ge over Fe_3Si, the films having a thickness ratio of 1:3. The characteristic $FeGe_2$ peaks can be observed in the three thicker films, while the thinner one failed to crystallize into the expected structure. Closer view about the (b) GaAs(002) and (c) GaAs(004) substrate peaks illustrate clearly the correlation between the peak heights and $FeGe_2$ nominal thickness.

On GaAs(001) substrates, a few nanometers of crystalline Fe_3Si are grown, on top of which amorphous Ge is deposited. The samples are then annealed as previously, from 150°C to

260°C at 5°/min, for up to one hour, and then brought back to room temperature. Fig. 5.3 shows the XRD curve taken on four samples with different Fe_3Si and Ge thicknesses but same 1:3 ratio. The samples having ratios of 2:6, 3:9 and 5:15 nm all share the same features. The characteristic rounded peaks corresponding to $FeGe_2$ are similar to those observed in Fig. 4.10, and their amplitudes correlate with the nominal thickness of the films. The 20 nm $FeGe_2$ sample (blue) is thick enough to show finite film thickness oscillations around the GaAs(002) substrate peak. In all curves, there is no noticeable feature that could be associated with Fe_3Si. The clear observation of $FeGe_2$ peaks suggests that the strategy was successful. Nonetheless, the XRD measurements are not sensitive enough to completely rule out the presence of an extremely thin residual Fe_3Si layer sitting underneath. The XRD curve of the sample with 1.5:4.5 thickness ratio does not show any sign of $FeGe_2$. This could indicate a lower limit in the formation of $FeGe_2$ using SPE.

Some of the samples previously discussed in the XRD curves where imaged by TEM, two of which are shown in Fig. 5.4. The micrograph shown in (a) depicts a sample with initial nominal film thicknesses of 3+9 nm (3 nm Fe_3Si and 9 nm Ge), in an attempt to obtain a 12 nm $FeGe_2$ film. We observe that there is about 2 nm of Fe_3Si left untouched below what seems to be another 2 nm $FeGe_2$. One should note that the surface of a sample can sometimes be damaged during the preparation of the TEM specimens. The etching of the lamella and manipulation of the sample could have removed a few nanometers of $FeGe_2$, which would explain why the film appears to be so thin. What is important to notice here is the presence of the Fe_3Si residual film. In this case, the annealing time (10 min) was insufficient, and the intermixing was not complete. The 2 nm Fe_3Si layer is too thin to be seen in the XRD curves, but is still thick enough to dominate in the context of electrical and magnetization measurements.

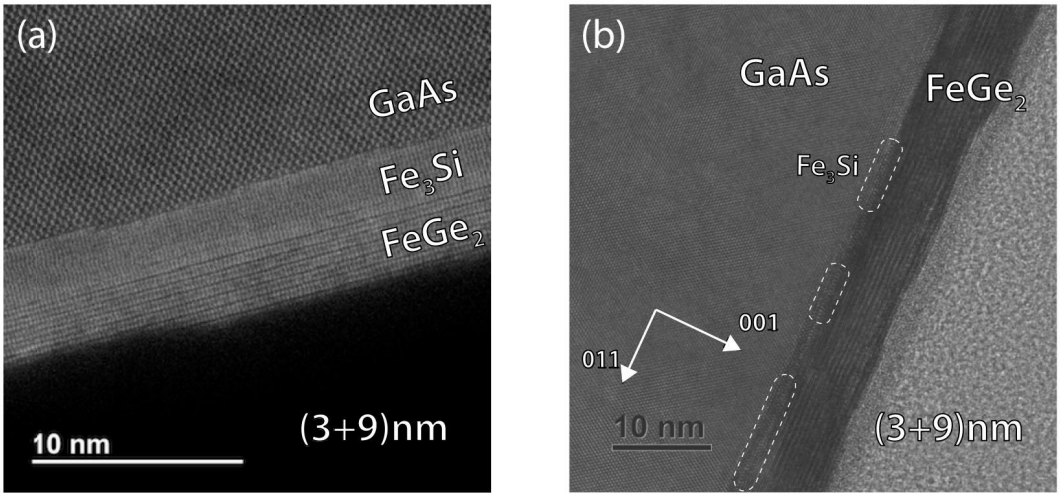

Figure 5.4: TEM micrographs of (a) a (3+9) nm sample, where 2 nm of Fe_3Si is still found underneath the $FeGe_2$ layer formed after 10 min annealing. The processing of the sample likely removed some $FeGe_2$ material from the surface, leaving the film thinner as it originally was. (b) a (3+9) nm sample annealed for 1 hour, where all Fe_3Si is mixed with Ge to form 12 nm $FeGe_2$.

The image shown in (b), depicts a sample in which the same initial layers where deposited (3+9 nm). This sample, however, was annealed for 1 hour at 260°C, which allowed the intermixing to proceed completely, yielding a single 12 nm layer of $FeGe_2$. There is essentially no visible Fe_3Si left, and the layered *P4mm* structured can be seen all the way to the interface with the GaAs substrate. Although there are 'patches' of Fe_3Si remaining on the surface (circled with dashed lines), those appear to be disconnected and should therefore not contribute to transport experiments attempted on the $FeGe_2$ film.

5.2.2 Temperature dependence of resistivity

Some of the 'pure' $FeGe_2$ samples obtained via the method previously discussed were subsequently used to create Hall bars. The design of the Hall bars has been described in Chapter 3, and shown in Fig. 3.10. The first and most straightforward step is then to use the $FeGe_2$ Hall bars for measurements of resistance at different temperatures. This can be achieved in the Attocube system, depicted in Fig. 3.11 (b).

The GaAs/$FeGe_2$ Hall bar samples are glued and bonded to a standard 8-pin G-10 (fiberglass laminate) chip holder, which in inserted at the bottom of the Attocube insert rod. The insert is then placed in a tubular metallic shield, which is pumped and filled with He gas (10 kPa). The insert is slipped slowly in the Attocube ,which was previously filled with liquid Helium, such as to immerse the metallic shield and cool down the sample via thermal exchange with the He gas. The base temperature for this system is limited to 4.1 K. Although the Attocube contains a heating element which can be activated to control the temperature of the sample, it is not being used to perform temperature measurements from 300 K down to 4 K (in order to save liquid He). Rather, the resistance of the sample is measured as the insert is manually brought down slowly in the Attocube (the insertion taking approximately 1 hour), making sure to let the system remain in thermal equilibrium throughout the process.

The longitudinal resistance of the Hall bar is measured using the 4-terminal configuration circuit (shown in Fig. 3.7 (b)), where the source applies a constant direct current of 10 μA and the voltage drop (V_{xx}) is measured along the sample using two different contacts parallel to the current flow. The temperature dependence of the resistance of two samples is presented in Fig. 5.5. The sample used in (a) is the (3+9) nm film discussed previously, in which there is a 2 nm Fe_3Si residue found underneath $FeGe_2$. As seen from the decreasing resistance of the sample as temperature is brought from 300 K to 4 K, the residual metallic Fe_3Si is assumed contribute principally to the electrical transport. This argument is better understood when compared with the curve shown in (b), which corresponds to the thinner (2+6) nm, isolated 8 nm $FeGe_2$ film. In this case, the behavior is reversed and the resistance is seen *increasing* as the temperature is lowered. This contrast in behavior suggests that only $FeGe_2$ is being probed in this second measurement, since the nonmetallic character cannot originate from conduction through any remaining Fe_3Si.

The positive linear slope seen in Fig. 5.5 (a) is conventional for metallic compounds, and the range of resistance values can somewhat be reconciled with our previous knowledge about the electrical properties of Fe_3Si. Making use of eq. 3.3, we can convert the resistance

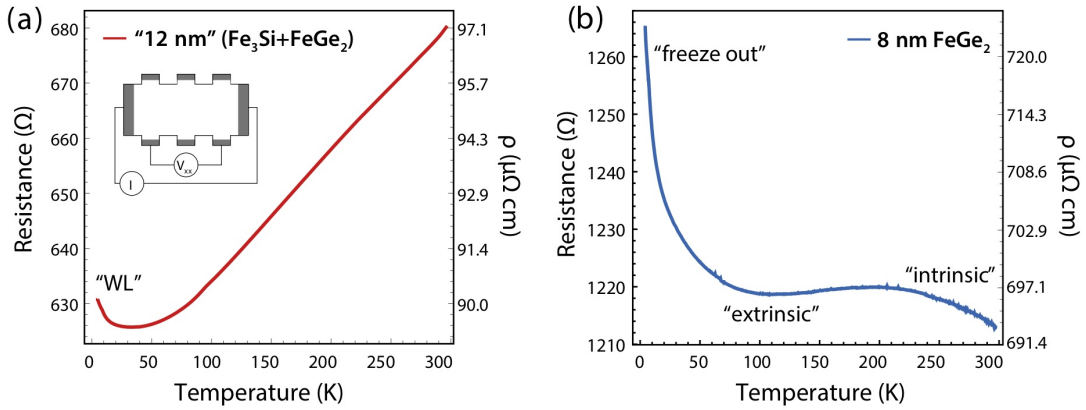

Figure 5.5: (a) DC 4-terminal measurement showing the resistance as a function of temperature in a $Fe_3Si/FeGe_2$ thin film stack. The slope indicates a metallic behavior, which is in fact caused by the leftover Fe_3Si still present after annealing. (b) Resistance as a function of temperature in a 8 nm thin film of pure $FeGe_2$. The increase of R at low temperature indicates a nonmetallic behavior, which can reasonably be attributed to $FeGe_2$ alone. The Hall bars used for the measurement were identical, with contacts as illustrated in the inset in (a), whose dimensions were used to calculate the film resistivity ρ (assuming 2 nm Fe_3Si).

values plotted above into resistivity, since we know the exact dimensions of the Hall bars: $\rho = t \cdot w \cdot R/L$, where $t \approx 2$ nm Fe_3Si (or 8 nm for $FeGe_2$), $w = 30$ µm and $L = 40$ µm are the effective thickness, width and length of the film tested. The converted values are shown on the secondary y-axis of the plots. The resistivity of Fe_3Si was previously reported to be 23 µΩcm at 77 K in a 32.6 nm film.[54] However, ρ is known to decrease with increasing thickness for metallic films in the 4-40 nm range[110], which can explain the higher values obtained for the 2 nm Fe_3Si residual layer. (As a comparison, a value of (75 µΩcm at room temperature was measured for ultra-thin 1.8 nm Fe films.[111]) The upturn of ρ for Fe_3Si at low temperature is, however, unconventional. One would rather expect the resistivity of metals to saturate (or drop to zero for superconductors) as the temperature approaches 0 K. Historically, similar observations have led to the discovery of the Kondo effect, which involves scattering with magnetic impurities becoming significant at low temperatures.[80] In our Fe_3Si thin film, such positive correction of ρ is rather attributed to weak localization (WL) effects. A very similar $\rho(T)$ behavior has been observed and discussed in the previously mentioned 1.8 nm thin Fe films.[111,112] WL is also expected to be stronger in 2D systems[113], as the available "paths" for electrons to go around each other are further constricted.

The curve of the 8 nm $FeGe_2$ sample shown in (b) is drastically different and corresponds, quite surprisingly, to a textbook example of $\rho(T)$ for extrinsic semiconductors. As the temperature is decreased from room temperature, the resistivity increases as expected in "intrinsic" SCs due to having less carriers excited to the conduction band. If the SC contained impurities, the "extrinsic" contribution will eventually dominate for a range of temperature where the number of thermally excited electrons has become low enough, hence the slight reversal to a "metal-like" slope. This change is however weak, and in this regime resistivity can be con-

sidered nearly constant in this transitive range.[114] All carriers ultimately "freeze out" a low temperature, meaning that none will be able to reach the conduction band which translates into a diverging resistivity.

It is intuitively difficult to understand why $FeGe_2$ (or $Fe(Ge_{0.83}Si_{0.17})_2$) would behave like an extrinsic SC. Normally, 'extrinsic' refers to a pure SC which has been modified via the insertion of doping elements. This is not the case for the fully ordered $FeGe_2$ structure, which is bound to this specific stoichiometry. One explanation could be that deep-level traps are caused by the insertion of Fe in Ge. Those traps are know to form as transition metals are inserted in Si and Ge,[115] and are usually detrimental to the electrical properties expected by conventional doping approaches.

Building on the experimental observation that $FeGe_2$ behaves like an extrinsic SC, the $\rho(T)$ curve in Fig. 5.5 (b) can be converted into a more insightful $\log(\sigma)$ vs $1/T$, from which it is possible to estimate the material's energy gap.[116,117] Indeed, the conductivity $\sigma = 1/\rho$ in a SC is expressed

$$\sigma = e \cdot (N_e \mu_e + N_h \mu_h), \tag{5.1}$$

where $N_{e,h}$ and $\mu_{e,h}$ are the concentration and mobility of electrons and holes, e is the electron charge. In the purely intrinsic regime, we find an equal number of electrons and holes, thus we have

$$\begin{aligned} N_e = N_h &= 2\left(\frac{k_B T}{2\pi\hbar^2}\right)^{\frac{3}{2}} (m_e^* m_h^*)^{\frac{3}{4}} \exp\left(\frac{-E_g}{2k_B T}\right) \\ &= C \cdot T^{\frac{3}{2}} \exp\left(\frac{-E_g}{2k_B T}\right) \end{aligned} \tag{5.2}$$

where some terms were grouped into a constant C, and E_g is the band gap.[78] Combining the two previous equations provides an expression for $\sigma(T)$:

$$\sigma(T) = C \cdot e(\mu_e + \mu_h) T^{\frac{3}{2}} \exp\left(\frac{-E_g}{2k_B T}\right). \tag{5.3}$$

In the high temperature intrinsic regime, $\mu_{e,h}$ will be dominated by lattice scattering (rather than impurity scattering) and decrease at a rate $\propto T^{-3/2}$. This can be understood from the increasing thermal velocity ($\propto \sqrt{T}$) and phonon scattering cross section ($\propto T$), which contribute together to reduce the mobility as T increases.[78] Within this estimate, the shrinking mobility exactly compensates the $T^{3/2}$ term of the carrier concentration, and we are left with a conductivity which is essentially $\propto \exp\left(-E_g/2k_B T\right)$. The consequence is that plotting $\log(\sigma)$ as a function of $1/T$ will produce a linear curve over temperatures corresponding to the intrinsic regime (high T), of which the slope is $s = -E_g/2k_B$:

$$\log(\sigma(T)) = \log\left(C \cdot \exp\left(\frac{-E_g}{2k_B T}\right)\right) = C + \left(\frac{-E_g}{2k_B}\right) \cdot \left(\frac{1}{T}\right). \tag{5.4}$$

This approach has been applied to our previous plot and the result is shown in Fig. 5.6. The curve is divided into linear sections, which can be associated with the intrinsic and ex-

trinsic regimes. The relevant part of the curve in found at higher temperature (low 1/T), over which a linear model was fitted to extract s (dotted red line). The slope was found to be $-(6.26 \pm 0.06)$ with units $[\frac{1}{K^{-1}}] = [K]$ (since log(σ) becomes unitless). We should note that the conversion of R to ρ and then σ depends on a constant scaling factor obtained from the geometry of the Hall bar. The uncertainty on these physical dimensions is not carried on the value of the slope s, as those would only affect the constant intercept in the model. Only the standard error in the linear slope fitting parameter was used to convey the uncertainty on E_g.

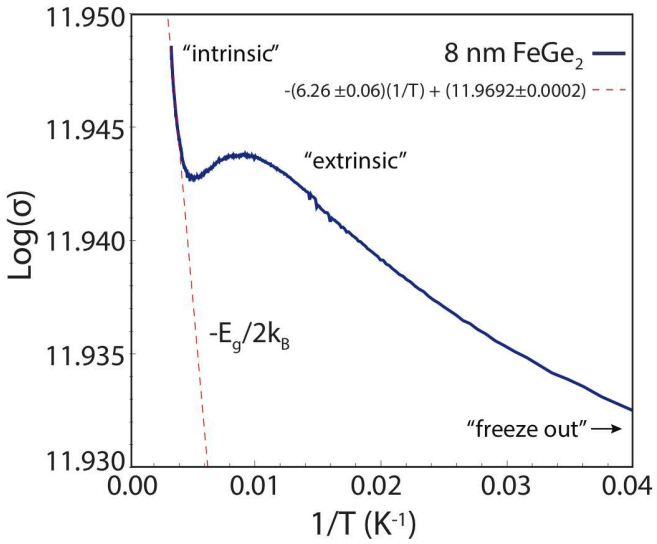

Figure 5.6: The $\rho(T)$ for the 8 nm $FeGe_2$ thin film converted into log(σ) plotted against 1/T. The slope indicated by the red dotted lines is equal to -$E_g/2k_B$.

Making use of eq. 5.4 and the slope extracted above, the value found for the band gap of $FeGe_2$ is $E_g = (6.26 \pm 0.06)$ K $\times\, 2k_B = (1.08 \pm 0.01)$ meV. For all intents and purposes, this value is *vanishingly* small. Although the 'semiconducting' character of $FeGe_2$ can be quite clearly detected in the context of lateral transport in the Hall bars, such a small E_g means that $FeGe_2$ cannot practically be used as a semiconductor. The compound should rather be regarded as a semimetal. This result helps understand the spin valve measurements discussed in the previous chapter: there is arguably no Schottky barriers emerging between Fe_3Si and $FeGe_2$, and the spin-selective transport is metallic.

5.2.3 Magnetization of a 12 nm $FeGe_2$ thin film

The successful isolation of $FeGe_2$ on GaAs substrates enables the direct study of the material's magnetization by SQUID magnetometry. Fig. 5.7 shows a series of measurements taken using a 12 nm $FeGe_2$ film (of which the TEM micrograph was previously shown in Fig. 5.4 (b)), and mounted in the system as described before. The measurements are taken along the [110] orientation of the GaAs substrate at different temperatures ranging from 2 K to 300 K, with

H being swept back and forth between $\pm$10000 Oe (to ensure a full magnetization of the film in both directions of the sweep). The diamagnetic contribution from the GaAs substrate was removed by fitting the high field parts of the hysteresis loops with a linear model. Since all measurements were done using the same piece of sample, the magnetization curves are not normalized to the magnetization saturation (as apposed to the different trilayer samples from the last chapter) and the amplitude of the hysteresis loops can be directly compared.

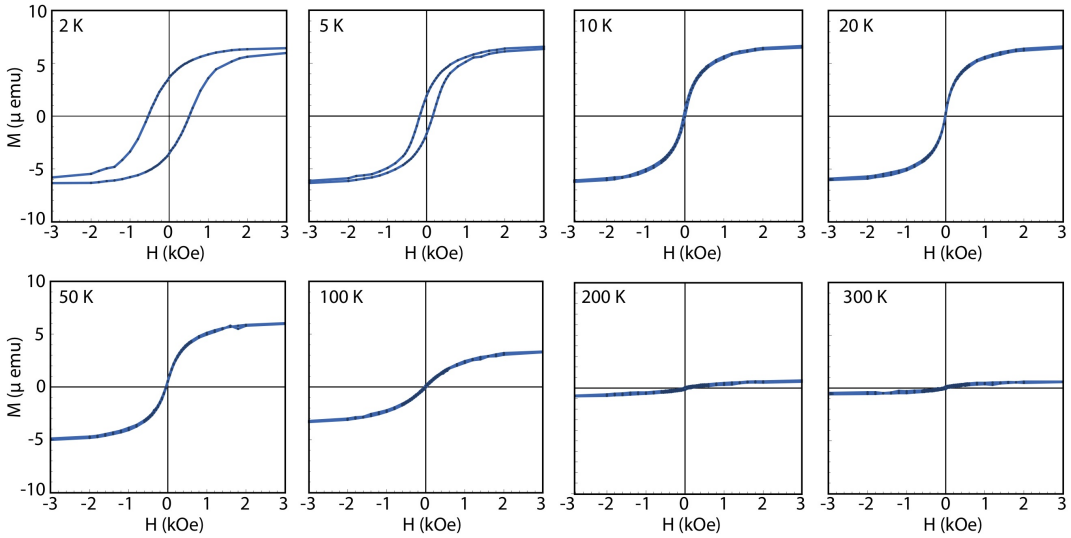

Figure 5.7: Magnetization of a 12 nm $FeGe_2$ film along the [110] orientation taken at different temperatures. The material is clearly ferromagnetic at low temperatures, and gradually transitions towards paramagnetic above 10 K. (Measurement taken by J. Herfort.)

The magnetization of $FeGe_2$ shows a clear temperature dependence, and demonstrates that the material undergoes a ferromagnetic transition at low temperatures. The film exhibits the strongest hysteresis at 2 K with coercive field $\sim$ 600 Oe, meaning that the material is magnetically much harder than Fe_3Si and Co_2FeSi, which usually show a sharp magnetization reversal within 20 Oe or lower. This coercivity decreases at 5 K, and eventually disappears starting at temperatures of 10 K and above. The film is then in a paramagnetic state, meaning that the Curie temperature of $FeGe_2$ is around 10 K. The amplitude of the magnetization in the paramagnetic state further decreases at higher temperatures, as expected from the $\chi \propto 1/T$ dependence of the magnetic susceptibility.[118]

The remanence of this 12 nm $FeGe_2$ film was directly investigated by magnetizing at low temperature and slowly warming up the SQUID sample space. The magnetizing field applied for this measurement was (only) 4 Oe, also along the [110] orientation, which should be sufficient to measurement a magnetization of the $FeGe_2$ film alone. Starting from 2 K, the sample is then brought back to room temperature while performing magnetization measurement at regular T intervals. The remanence curve obtained is shown in Fig. 5.8. As expected from the hysteresis loops shown above, the $FeGe_2$ thin film looses its ferromagnetic character around 10 K. This transition is relatively sharp (considering the logarithmic scale), and allows

to establish a good estimate for the Curie point. The material being paramagnetic beyond this point is observed in the linear behavior of M about 0 emu up to 300 K.

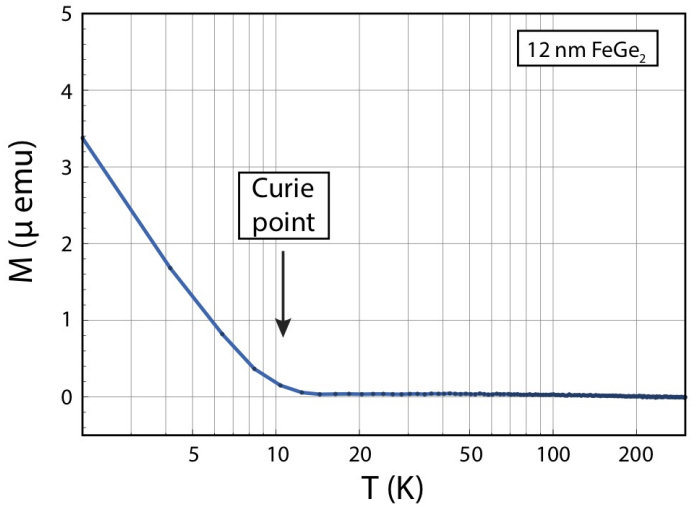

Figure 5.8: Remanence of a 12 nm $FeGe_2$ film along the [110] orientation with 4 Oe magnetizing field. The Curie point around 10 K is consistent with the disappearance of the ferromagnetic hysteresis shown before. (Measurement by J. Herfort.)

5.2.4 Planar Hall effect

The possibility to apply magnetic fields in and out of plane in the Attocube has been used to investigate the planar Hall effect (PHE) in the Hall bar samples discussed above. Alike the conventional Hall effect, the PHE measures the voltage build up across a sample and perpendicular to the applied current. However, the external magnetic field is applied *in* plane, which effectively modifies the magnetization of the sample instead of drifting charge carriers due to Lorentz forces. To appreciate these experiments, we refer to the theory presented in Chapter 3 regarding measurements of the Hall effect in ferromagnetic materials. As a reminder, the generalized Hall voltage as a function of the sample's magnetization M was expressed

$$V_H = R_s \frac{MI}{d} \cos(\theta) + k \frac{M^2 I}{d} \sin^2(\theta) \sin(2\phi), \tag{5.5}$$

which accounts for both the normal Hall effect and anomalous Hall effect.

To understand what to expect from such measurements, we should consider the magnetization M as a hysteresis loop that is effectively a function of the applied magnetizing field H, as exemplified in the first panel of Fig. 5.9. Thus, in eq. 5.5 the measured V_H is also hysteretic, and reflects the shape of the magnetization as the external H field is swept. If the component of the external magnetic field is perfectly out of plane, then $\phi = 0$ and the PHE term vanishes. The V_H then reflects the normal (linear) Hall effect plus a shift between the two different directions of the sweep (the effect commonly associated to the AHE). The interesting configuration for us comes when $\theta = \pi/2$ and the component of the external field is purely in-plane. In this

case, and R_H can be simply expressed

$$R_H = constant \cdot M^2 \sin(2\phi) \tag{5.6}$$

and the shape of M^2 can be accessed directly *without* a contribution from Lorentz forces. The measurement R_H is then $\propto M^2$, and the hysteresis curve adopts a double lobe shape as seen in the second and third panel of Fig. 5.9. Depending on the value of ϕ, the orientation of M with respect to I, the sign of R_H can be either positive or negative. In all cases, the points of R_H closest to the origin correspond to the coercive field H_c of the material, i.e. the point at which the sample's effective magnetization is zero.

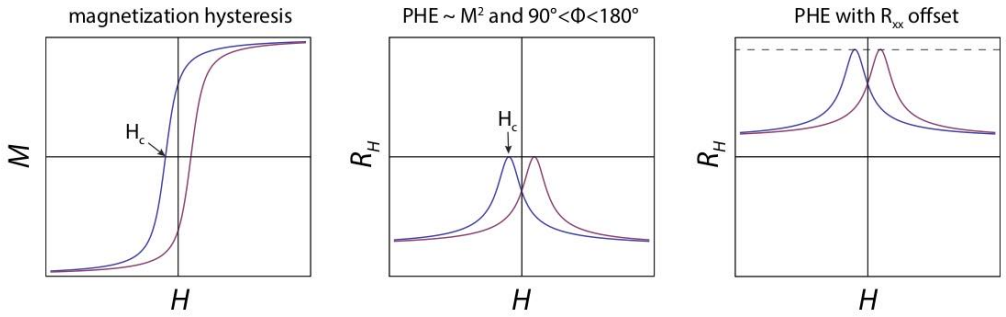

Figure 5.9: A typical magnetic hysteresis loop and corresponding R_H measurement in the PHE regime.

Upon measuring real samples, the curve shown in the central panel can however be shifted vertically due to residual longitudinal resistance (R_{xx}), a factor that is not included in eq. 5.6. Indeed, in case the lateral contacts used to measure V_H are not *exactly* aligned, which is usually the case, a V_{xx} component can be picked up by the measurement and shift the hysteresis curve further below or above the the origin. This case is represented in the last panel of Fig. 5.9.

With these key concepts in mind, it is possible to grasp the PHE measured in the 8 nm $FeGe_2$ thin film and shown in Fig. 5.10. The plots correspond to two PHE measurement taken at 'equivalent' angles $\phi = 170°$and $\phi = 280°$. Those angles are only approximative since the Attocube system is not equipped to precisely report angles: the whole insert tube must be rotated manually, and not all angles are accessible due to different components blocking each other. This approximation is nonetheless sufficient for a qualitative appreciation of the PHE. The measurements are done at 4.1 K. This means that the $FeGe_2$ is technically reaching towards the "freeze out" part of the conductivity, but transport should be dominated by impurity scattering and make anomalous Hall events better observable. At this temperature, we have seen from SQUID measurements the sample is in its ferromagnetic state. A DC current of 50 µA is applied along the Hall bar, and V_H is measured using lateral contacts half-way as the external in-plane field is swept back and forth from ± 0.5 T.

The curves are visibly hysteretic, with the blue and red parts corresponding to the two directions of the magnetic field sweep. This result indicates that the magnetization of $FeGe_2$

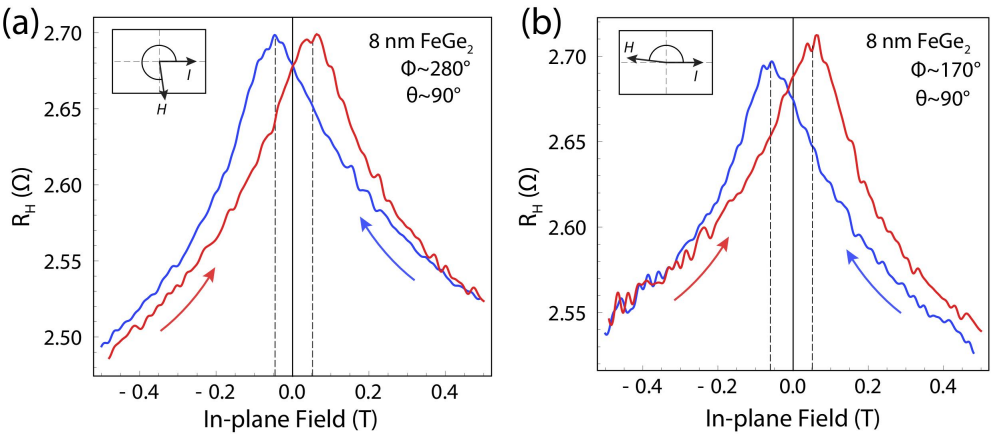

Figure 5.10: Planar Hall measurements done at 4.1 K in 8 nm $FeGe_2$ film along 'equivalent' orientations of the external magnetic filed with respect to the current.

also follows a hysteresis curve, confirming again that the material is ferromagnetic at low temperature. The coercive field H_c is seen at $\sim$0.05 T, which corresponds to a magnetic field strength in vacuum of $\sim$ 500 Oe ($H = B/\mu_0$). This value is consistent with the coercive field observed at 5 K in the SQUID magnetometer. The shape of the PHE does not contain sharp magnetic switching along both angles investigated. Thus $FeGe_2$ does not show a clear easy magnetization axis and, as opposed to Fe_3Si and Co_2FeSi, and does not have a cubic magnetocrystalline anisotropy.

The curves are also shifted vertically by about 2.7Ω. As explained above, this is due to a possible offset in the alignment of the contacts measurement V_H. Indeed, the $R_{xx}(T)$ curve previously discussed reaches $\sim$1265 Ω at 4.1 K. A longitudinal offset of a few nm between the contacts could therefore account for the 2.7Ω residual resistance in the R_H calculated above. The symmetry of the hysteresis confirms that θ was close to 90°in both measurements.

5.3 Summary

To sum up, the new *P4mm* polymorph of $FeGe_2$ has been, and still remains, an interesting subject of investigations in materials science and solid-state physics. The material was originally obtained by accident, but still provided the right properties for the spin valve signals to be detected and establish a proof of concept for the SS-SBTT. The formation of *P4mm* $FeGe_2$ comes from a minimization of the elastic energy of the thin film, which prevents the obtention of the material in a bulk form. It was possible to completely isolate the material into 8 nm and 12 nm thin films over semi-insulating GaAs, with which transport measurements could be conducted. The resistivity of $FeGe_2$ indicates that the compound behaves like an extrinsic semiconductor, although with an extremely small band gap. A study of the PHE could peak into the behavior of the magnetization of $FeGe_2$, and confirmed that the material is ferromagnetic at low temperatures.

The discovery of $FeGe_2$ could find interest in the growing field of 2D ferromagnetism. The presence of ferromagnetism in low-dimensional systems is usually forbidden, but has been realized in small number of materials. A search for new 2D ferromagnets is ongoing for a number of fundamental and technological developments. Although the layered structure is not separated by Van der Waals gaps, it might be possible to isolate the films down to a single monolayer using methods other than exfoliation.

6 Conclusion and Future Work

6.1 Initial goals

The overarching goal of this thesis has been to fabricate the hybrid ferromagnetic/semiconductor trilayers which would constitute a building base for a Spin-selective Schottky barrier tunnel transistor (shortened as SS-SBTT). The device would offer the possibility to perform conventional logic operations while preserving the spin polarization of electrical currents. The SS-SBTT therefore constitutes and interesting new component on which the next computational paradigms could be built, combined with research efforts invested in the field of spintronics.

The principle of the SS-SBTT is inspired from the combination of magnetic tunnel junctions (MTJ) and Schottky barrier tunnel transistors (SBTT). MTJs, usually made of two ferromagnetic (FM) films separated by a thin insulating tunnel barrier, can offer two distinct resistance states depending of the relative direction of the magnetization of the FM films. The low magnetoresistance state is achieved when the films are magnetized along the same orientation, as tunneling events involving spins from the majority spin subband are favored. This feature plays the role of spin filter. Combined with the idea of the SBTT, the spin polarized current could then be modulated, and the device operated as a spin-selective transistor. The fabrication of the SS-SBTT requires growing high quality lattice-matched FM/SC/FM thin film stacks. MBE is usually well suited to produce FM/SC heterostructures in which the FM film is grown over SC films or substrates. However, growing FM/SC/FM trilayers implies that a SC must be grown over a FM film at some point during the process. SC have higher crystallization energies than most metals, meaning that a direct growth is likely to produce intermixing between the film and destroy the interface, lowering drastically the chances to realize efficient spin injection. This challenge originally lead to the idea to develop the solid-phase epitaxy (SPE) approach.

6.2 Main results

The choice of Heusler alloys used in this thesis, Fe_3Si and Co_2FeSi, was based on their advantageous magnetic properties (high magnetization, high Curie temperature), as well as on their lattice parameter being compatible with Ge and GaAs. Considerable experience had already been acquired over the past decades regarding the growth these compounds by MBE on GaAs(001) substrates. Ge itself grows at low temperature for a semiconductor (300°C), which minimizes the changes of undesirable reactions at the interface with Fe_3Si upon crystallization

by annealing. To optimize the SPE parameters of amorphous Ge over Fe_3Si, bilayer samples were annealed at rate of 5°C/min up to temperatures ranging from 200 to 380°C and studied by RHEED and XRD. It was first possible to detect the crystallization of the amorphous film from the appearance of RHEED streaks after a few minutes into the annealing procedure. These RHEED streaks are aligned with those produced by the GaAs(001) and Fe_3Si surfaces, which indicate a pseudomorphic growth relationship. However, XRD revealed that annealing temperatures above 280°C can trigger the formation of undesirable byproducts and degradation of the interface. The range of 'safe' annealing temperatures was determined to be between 240-280°C, which result in the formation of a crystalline Ge-rich compound over which it was possible to grow a capping Fe_3Si or Co_2FeSi film by MBE.

TEM and XRD studies revealed that the Ge-rich compound obtained by SPE is $FeGe_2$, which sits lattice-matched over Fe_3Si. Tuning the thickness of the $Fe_3Si/FeGe_2/Fe_3Si$ trilayers to be (36/4-8/12) nm allowed to see a 1:3 beating pattern in the XRD curves, which confirmed that the stacks had impeccable interface quality over extended areas. HRTEM micrographs of the trilayers also confirmed the high quality of the interfaces between the FM films and $FeGe_2$ when SPE is performed over Fe_3Si. When SPE is performed over Co_2FeSi, another crystalline compound is created instead, labeled Ge(Co,Fe,Si), which also forms in a lattice-matched way and enables the growth of a capping metallic layer. The XRD curves and TEM micrographs show that this specific compound is not layered. The interfaces with the adjacent films are less sharp, due to the higher reactivity of Co_2FeSi. The realization of such trilayers represents a rare example of epitaxial growth of a Ge-rich compound over a metal, and paves the way for other applications in materials science.

The investigation of the samples by SQUID magnetometry revealed that it is possible to dissociate the magnetic behavior of FM films when separated by a $FeGe_2$ buffer layer thicker than 4 nm. The low-temperature SQUID magnetic hysteresis loops taken with $Fe_3Si/FeGe_2/Fe_3Si$ and $Fe_3Si/FeGe_2/Co_2FeSi$ samples showed plateaus of antiparallel magnetization along the [110] axis, with amplitudes consistent with the contribution of the individual 36 nm and 12 nm FM films to the total magnetization. A careful study of the stacks containing sequentially single, double and triple layers, revealed that there is an interplay between the magnetization of the individual thin films. The interfaces contribute noticeably to the total magnetization along different axes, especially for thinner $FeGe_2$ films. The features produced can be associated to details of the atomic bonding between the layers. However, those effects do not prevent the trilayer stacks to achieve distinct states of parallel and antiparallel magnetization observable at low temperature, as expected to operate conventional MTJs.

Vertical spin valves were created using $Fe_3Si/FeGe_2/Fe_3Si$ and $Fe_3Si/FeGe_2/Co_2FeSi$ trilayer samples and tested at room and cryogenic temperatures. It was possible to detect spin valve signals, as indicated by clear peaks of high magnetoresistance (MR) corresponding to the aforementioned states of antiparallel magnetization of the two FM films. The magnitude of the MR peaks never exceeds 0.30%, which remains small as compared to conventional spin valves. Decreasing the thickness of the $FeGe_2$ buffer layer further decreases the MR amplitude, which does not corresponding to a typical tunneling behavior. Instead, the injection

likely proceeds via spin-preserved thermionic emission over the vanishingly small potential barriers emerging at the $FeGe_2$ interfaces, which is effectively perceived as metallic conduction. The MR is the highest at room temperature, which is related to the ferromagnetic transition happening in $FeGe_2$ at low temperatures, causing spin-spin interaction and reducing the difference in resistance between the parallel and antiparallel orientation of the FM electrodes. Those results, despite deviating from the original SS-SBTT device concept, do not prevent using the devices fabricated for eventual applications, and establish a satisfying implementation of vertical spin valves based on our hybrid trilayer stacks.

The formation of $FeGe_2$ came as a surprise, and motivated a series of investigations conducted in parallel with our original device-oriented goal. $FeGe_2$ is a new metastable layered polymorph with space group *P4mm*. Its structure was fully confirmed by both XRD and TEM experiments and simulations. Given that the compound forms by annealing amorphous Ge over Fe_3Si, we expect that Si atoms are diffusing and substitute at most 17% of the Ge sites. We have succeeded in isolating $FeGe_2$ on GaAs(001) by tuning the thickness ratio between the underlying Fe_3Si and amorphous Ge such as to obtain the right stoichiometry once all atoms are intermixed. Hall bars created on 8 nm $FeGe_2$ thin films revealed that the longitudinal resistivity increases at low temperature following a behavior reminiscent of extrinsic semiconductors. An estimation of the band gap of $FeGe_2$, however, indicates that it is extremely small ((1.08 ± 0.01) meV). This observation clarified why the spin valve measurements do not behave as expected from assuming the emergence of Schottky barriers at the $Fe_3Si/FeGe_2$ interface (spin injection via tunneling should decrease in amplitude with increasing barrier thickness). Low-temperature planar Hall measurement showed hysteresis loops consequent with the presence of magnetism in the thin films, also confirmed by SQUID magnetometry.

6.3 Future investigations and devices

At this point of our project, a fully-functioning SS-SBTT could not be implemented. However, the experiments performed throughout this endeavor have brought us closer than ever to fulfill our goal. The SPE method was used produce trilayer stacks of unprecedented quality, with which functioning vertical spin valve devices could be fabricated. The developments and results obtained to reach this milestone are numerous and can hopefully be used to solve broader problems in materials science.

The following steps along our path towards the realization of a SS-SBTT would be to electrically contact the $FeGe_2$ barrier separating the two FM films. As stated in the description of the device, modulating the barrier height that arises at the $FeGe_2$ interfaces would, ideally, result in a significant change in the magnetoresistance measured across the vertical spin valves. If we refer to the Hall measurements conducted on the 'bare' films, the *p*-type nature of $FeGe_2$ would not necessarily be problematic considering the original band engineering idea behind the Schottky-barrier transistor, as K. Wu also introduces the so-called p-channel SBTT in his original patent.[21] The main challenge here rather concerns the fabrication of the SS-SBTT, which would require an intricate sequence of lithography, etching and thin film deposition,

in order to establish a contact with the 6 nm $FeGe_2$ buffer layer without touching the adjacent FM films. Although delicate, this process could be designed and optimized, with a fair dose of work.

Bibliography

[1] G. E. Moore, *Cramming more components onto integrated circuits*, Electronics **38**, 4p (1965).

[2] G. E. Moore, *Progress in Digital Integrated Electronics*, Technical report, International Electron Devices Meeting, IEEE (1975).

[3] *Our Stories - Gordon Moore about Moore's Law*, ASML, online interview (2014).

[4] J. Koomey, S. Berard, M. Sanchez, and H. Wong, *Implications of Historical Trends in the Electrical Efficiency of Computing*, IEEE Annals of the History of Computing **33**, 46–54 (2011).

[5] D. Clark, *Intel Rechisels the Tablet on Moore's Law*, Wall Street Journal (2015), online access July 2019 .

[6] *Intel's 10 nm Technology: Delivering the Highest Logic Transistor Density in the Industry Through the Use of Hyper Scaling*, Technical report, Intel (2017).

[7] *Beyond CMOS*, Technical report, International Technology Roadmap for Semiconductors 2.0 (2015).

[8] I. Žutić, J. Fabian, and S. Das Sarma, *Spintronics: Fundamentals and applications*, Rev. Mod. Phys. **76**, 323–410 (2004).

[9] N. F. Mott, *The electrical conductivity of transition metals*, Proc. R. Soc. London **A 153**, 699–717 (1936).

[10] N. F. Mott, *The resistance and thermoelectric properties of the transition metals*, Proc. R. Soc. London **A 156**, 368–382 (1936).

[11] J. S. Moodera and G. Mathon, *Spin polarized tunneling in ferromagnetic junctions*, J. Magn. Magn. Mater. **200**, 248 – 273 (1999).

[12] E. I. Rashba, *Theory of electrical spin injection: Tunnel contacts as a solution of the conductivity mismatch problem*, Phys. Rev. B **62**, R16267–R16270 (2000).

[13] J. G. Simmons, *Generalized Formula for the Electric Tunnel Effect between Similar Electrodes Separated by a Thin Insulating Film*, J. Appl. Phys. **34**, 1793–1803 (1963).

[14] J.-G. Zhu and C. Park, *Magnetic tunnel junctions*, Mater. Today **9**, 36–45 (2006).

[15] J. Bardeen, *Surface States and Rectification at a Metal Semi-Conductor Contact*, Phys. Rev. **71**, 717–727 (1947).

[16] T. Nishimura, K. Kita, and A. Toriumi, *Evidence for strong Fermi-level pinning due to metal-induced gap states at metal/germanium interface*, Appl. Phys. Lett. **91**, 123123 (2007).

[17] K. Kasahara, S. Yamada, K. Sawano, M. Miyao, and K. Hamaya, *Mechanism of Fermi level pinning at metal/germanium interfaces*, Phys. Rev. B **84**, 205301 (2011).

[18] R. Nouchi, *Extraction of the Schottky parameters in metal-semiconductor-metal diodes from a single current-voltage measurement*, J. Appl. Phys. **116**, 184505 (2014).

[19] R. T. Tung, *Schottky barrier height-do we really understand what we measure?*, J. Vac. Sci. Technol. B **11**, 1546–1552 (1993).

[20] A. Zekry and G. Eldallal, *Effect of MS contact on the electrical behaviour of solar cells*, Solid State Electron. **31**, 91–97 (1988).

[21] K. Wu, *Schottky-barrier tunneling transistor*, US6744111B1 (2004).

[22] L. Zhang, H. Dong, N. Deng, M. Ren, J.-N. Hu, and P.-Y. Chen, *Spin-polarized thermionic emission at the interface of ferromagnetic metal and organic semiconductor*, In *2007 7th IEEE Conference on Nanotechnology (IEEE NANO)*, pages 220–223 (2007).

[23] M. Jullière, *Tunneling between ferromagnetic films*, Phys. Lett. A **54**, 225 – 226 (1975).

[24] J. Mathon and A. Umerski, *Theory of tunneling magnetoresistance of an epitaxial Fe/MgO/Fe(001) junction*, Phys. Rev. B **63**, 220403 (2001).

[25] S. S. P. Parkin, C. Kaiser, A. Panchula, P. M. Rice, B. Hughes, M. Samant, and S.-H. Yang, *Giant tunnelling magnetoresistance at room temperature with MgO (100) tunnel barriers*, Nat. Mater. **3**, 862–867 (2004).

[26] S. Ikeda, J. Hayakawa, Y. Ashizawa, Y. M. Lee, K. Miura, H. Hasegawa, M. Tsunoda, F. Matsukura, and H. Ohno, *Tunnel magnetoresistance of 604% at 300K by suppression of Ta diffusion in CoFeB/MgO/CoFeB pseudo-spin-valves annealed at high temperature*, Appl. Phys. Lett. **93**, 082508 (2008).

[27] H. xi Liu, T. Kawami, K. Moges, T. Uemura, M. Yamamoto, F. Shi, and P. M. Voyles, *Influence of film composition in quaternary Heusler alloy Co_2(Mn,Fe)Si thin films on tunnelling magnetoresistance of Co_2(Mn,Fe)Si/MgO-based magnetic tunnel junctions*, J. Phys. D **48**, 164001 (2015).

[28] W. H. Butler, X. . Zhang, S. Vutukuri, M. Chshiev, and T. C. Schulthess, *Theory of tunneling magnetoresistance for epitaxial systems*, IEEE T. Magn. **41**, 2645–2648 (2005).

[29] W. H. Butler, *Tunneling magnetoresistance from a symmetry filtering effect*, Sci. Technol. Adv. Mater. **9**, 014106 (2008).

[30] D. Monsma, R. Vlutters, and J. Lodder, *Room temperature-operating Spin-Valve Transistor formed by vacuum bonding*, Science **281**, 407–409 (1998), Imported from SMI Reference manager.

[31] A. T. Hanbicki, B. T. Jonker, G. Itskos, G. Kioseoglou, and A. Petrou, *Efficient electrical spin injection from a magnetic metal/tunnel barrier contact into a semiconductor*, Appl. Phys. Lett. **80**, 1240 (2002).

[32] J. Herfort, H.-P. Schönherr, and K. H. Ploog, *Epitaxial growth of Fe_3Si/GaAs(001) hybrid structures*, Appl. Phys. Lett. **83**, 3912 (2003).

[33] B. D. Schultz, N. Marom, D. Naveh, X. Lou, C. Adelmann, J. Strand, P. A. Crowell, L. Kronik, and C. J. Palmstrøm, *Spin injection across the Fe/GaAs interface: Role of interfacial ordering*, Phys. Rev. B **80**, 201309 (2009).

[34] G. Schmidt, D. Ferrand, L. W. Molenkamp, A. T. Filip, and B. J. van Wees, *Fundamental obstacle for electrical spin injection from a ferromagnetic metal into a diffusive semiconductor*, Phys. Rev. B **62**, R4790 (2000).

[35] A. T. Hanbicki, O. M. J. van't Erve, R. Magno, G. Kioseoglou, C. H. Li, B. T. Jonker, G. Itskos, R. Mallory, M. Yasar, and A. Petrou, *Analysis of the transport process providing spin injection through an Fe/AlGaAs Schottky barrier*, Appl. Phys. Lett. **82**, 4092 (2003).

[36] D. O. Demchenko and A. Y. Liu, *Influence of interface structure on electronic properties and Schottky barriers in Fe/GaAs magnetic junctions*, Phys. Rev. B **73**, 115332 (2006).

[37] Q. O. Hu, E. S. Garlid, P. A. Crowell, and C. J. Palmstrøm, *Spin accumulation near Fe/GaAs (001) interfaces: The role of semiconductor band structure*, Phys. Rev. B **84**, 085306 (2011).

[38] T. J. Zega, A. T. Hanbicki, S. C. Erwin, I. Žutić, G. Kioseoglou, C. H. Li, B. T. Jonker, and R. M. Stroud, *Determination of Interface Atomic Structure and Its Impact on Spin Transport Using Z-Contrast Microscopy and Density-Functional Theory*, Phys. Rev. Lett. **96**, 196101 (2006).

[39] S. Fujii, S. Sugimura, Ishida, and S. Asano, *Hyperfine fields and electronic structures of the Heusler alloys Co_2MnX (X=Al, Ga, Si, Ge, Sn)*, J. Phys. Condens. Matter **2**, 8583–8589 (1990).

[40] I. Galanakis, P. H. Dederichs, and N. Papanikolaou, *Slater-Pauling behavior and origin of the half-metallicity of the full-Heusler alloys*, Phys. Rev. B **66**, 174429 (2002).

[41] B. Balke, S. Wurmehl, G. H. Fecher, C. Felser, and J. Kübler, *Rational design of new materials for spintronics: Co_2FeZ (Z=Al, Ga, Si, Ge)*, Sci. Technol. Adv. Mater. **9**, 014102 (2008).

[42] I. Galanakis, P. H. Dederichs, and N. Papanikolaou, *Origin and properties of the gap in the half-ferromagnetic Heusler alloys*, Phys. Rev. B **66**, 134428 (2002).

[43] F. Heusler, *Über magnetische Manganlegierungen*, Verh. Dtsch. Phys. Ges. **5**, 219 (1903).

[44] C. J. Palmstrøm, *Heusler compounds and spintronics*, Prog. Cryst. Growth Charact. Mater. **62**, 371 (2016).

[45] R. Farshchi and M. Ramsteiner, *Spin injection from Heusler alloys into semiconductors: A materials perspective*, J. Appl. Phys. **113**, 191101 (2013).

[46] C. J. Palmstrøm, *Epitaxial Heusler Alloys: New Materials for Semiconductor Spintronics*, MRS Bulletin **28**, 725 (2003).

[47] L. Makinistian, M. M. Faiz, R. P. Panguluri, B. Balke, S. Wurmehl, C. Felser, E. A. Albanesi, A. G. Petukhov, and B. Nadgorny, *On the half-metallicity of Co_2FeSi Heusler alloy: Point-contact Andreev reflection spectroscopy and ab initio study*, Phys. Rev. B **87**, 220402 (2013).

[48] M. Hashimoto, J. Herfort, H.-P. Schönherr, and K. H. Ploog, *Epitaxial Heusler alloy Co_2FeSi/GaAs(001) hybrid structures*, Appl. Phys. Lett. **87**, 102506 (2005).

[49] P. J. Webster and K. R. A. Ziebeck, *Magnetic Properties of Metals*, page 101, Landolt-Börnstein, New Series III/19c, Berlin (1988).

[50] J. Kalt, M. Sternik, I. Sergueev, J. Herfort, B. Jenichen, H.-C. Wille, O. Sikora, P. Piekarz, K. Parlinski, T. Baumbach, and S. Stankov, *Lattice dynamics of epitaxial strain-free interfaces*, Phys. Rev. B **98**, 121409 (2018).

[51] A. Ionescu, C. A. F. Vaz, T. Trypiniotis, C. M. Gürtler, H. García-Miquel, J. A. C. Bland, M. E. Vickers, R. M. Dalgliesh, S. Langridge, Y. Bugoslavsky, Y. Miyoshi, L. F. Cohen, and K. R. A. Ziebeck, *Structural, magnetic, electronic, and spin transport properties of epitaxial* $Fe_3Si/GaAs(001)$, Phys. Rev. B **71**, 094401 (2005).

[52] C. Palmstrøm, *Epitaxial Heusler Alloys: New Materials for Semiconductor Spintronics*, MRS Bulletin **28**, 725–728 (2003).

[53] U. Starke, J. Schardt, W. Weiss, W. Meier, C. Polop, P. L. de Andres, and K. Heinz, *Structural and compositional reversible phase transitions on low-index Fe_3Si surfaces*, EPL **56**, 822 (2001).

[54] B. Jenichen, V. M. Kaganer, J. Herfort, D. K. Satapathy, H. P. Schönherr, W. Braun, and K. H. Ploog, *Long-range order in thin epitaxial Fe_3Si films grown on GaAs(001)*, Phys. Rev. B **72**, 075329 (2005).

[55] T. Hentschel, B. Jenichen, A. Trampert, and J. Herfort, *Ferromagnetic Heusler alloy Co_2FeSi films on GaAs(110) grown by molecular beam epitaxy*, J. Phys. D **45**, 055002 (2012).

[56] B. Jenichen, T. Hentschel, J. Herfort, X. Kong, A. Trampert, and I. Zizak, *Characterization of $L2_1$ order in Co_2FeSi thin films on GaAs*, J. Phys. Conf. Ser. **471**, 012022 (2013).

[57] B. Jenichen, J. Herfort, K. Kumakura, and A. Trampert, *Long-range order and thermal stability of thin Co_2FeSi films on GaAs(1 1 1)B*, **43**, 285404 (2010).

[58] K. Kasahara, K. Yamamoto, S. Yamada, T. Murakami, K. Hamaya, K. Mibu, and M. Miyao, *Highly ordered Co_2FeSi Heusler alloys grown on Ge(111) by low-temperature molecular beam epitaxy*, J. Appl. Phys. **107**, 09B105 (2010).

[59] S. Yamada, K. Hamaya, K. Yamamoto, T. Murakami, K. Mibu, and M. Miyao, *Significant growth-temperature dependence of ferromagnetic properties for Co_2FeSi/Si(111) prepared by low-temperature molecular beam epitaxy*, Appl. Phys. Lett. **96**, 082511 (2010).

[60] K. Hamaya, K. Ueda, Y. Kishi, Y. Ando, T. Sadoh, and M. Miyao, *Epitaxial ferromagnetic Fe_3Si/Si(111) structures with high-quality heterointerfaces*, Appl. Phys. Lett. **93**, 132117 (2008).

[61] Y. Ando, K. Hamaya, K. Kasahara, K. Ueda, Y. Nozaki, T. Sadoh, Y. Maeda, K. Matsuyama, and M. Miyao, *Magnetic properties of epitaxially grown Fe_3Si/Ge(111) layers with atomically flat heterointerfaces*, J. Appl. Phys **105**, 07B102 (2009).

[62] K. Hamaya, T. Murakami, S. Yamada, K. Mibu, and M. Miyao, *Local structural ordering in low-temperature-grown epitaxial $Fe_{3+x}Si_{1-x}$ films on Ge(111)*, Phys. Rev. B **83**, 144411 (2011).

[63] S. Yamada, J. Sagar, S. Honda, L. Lari, G. Takemoto, H. Itoh, A. Hirohata, K. Mibu, M. Miyao, and K. Hamaya, *Room-temperature structural ordering of a Heusler compound Fe_3Si*, Phys. Rev. B **86**, 174406 (2012).

[64] J. Herfort, H.-P. Schönherr, K.-J. Friedland, and K. H. Ploog, *Structural and magnetic properties of epitaxial Fe_3Si/GaAs(001) hybrid structures*, J. Vac. Sci. Technol. B **22**, 2073 (2004).

[65] M. Ikawa, M. Kawano, S. Sakai, S. Yamada, T. Kanashima, and K. Hamaya, *Influence of the Ge diffusion on the magnetic and structural properties in Fe_3Si and CoFe epilayers grown on Ge*, J. Cryst. Growth **468**, 676–679 (2017).

[66] M. Miyao, K. Hamaya, K. Sadoh, H. Itoh, and Y. Maeda, *Molecular beam epitaxial growth of ferromagnetic Heusler alloys for group-IV semiconductor spintronic devices*, Thin Solid Films **518**, S273 (2010).

[67] K. Yamane, K. Hamaya, Y. Ando, Y. Enomoto, K. Yamamoto, T. Sadoh, and M. Miyao, *Effect of atomically controlled interfaces on Fermi-level pinning at metal/Ge interfaces*, Appl. Phys. Lett. **96**, 162104 (2010).

[68] M. Kawano, K. Santo, M. Ikawa, S. Yamada, T. Kanashima, and K. Hamaya, *Spin transport in p-Ge through a vertically stacked Ge/Fe_3Si junction*, Appl. Phys. Lett. **109**, 022406 (2016).

[69] K. Hamaya, Y. Fujita, M. Yamada, M. Kawano, S. Yamada, and K. Sawano, *Spin transport and relaxation in germanium*, J. Phys. D: Appl. Phys. **51**, 393001 (2018).

[70] B. Jenichen, U. Jahn, A. Nikulin, J. Herfort, and H. Kirmse, *Structure of Fe_3Si/Al/Fe_3Si thin film stacks on GaAs(001)*, Semicond. Sci. Technol. **30**, 114005 (2015).

[71] S. Yamada, K. Tanikawa, M. Miyao, and K. Hamaya, *Atomically Controlled Epitaxial Growth of Single-Crystalline Germanium Films on a Metallic Silicide*, Cryst. Growth Des. **12**, 4703 (2012).

[72] M. Kawano, S. Yamada, K. Tanikawa, K. Sawano, M. Miyao, and K. Hamaya, *An ultrathin buffer layer for Ge epitaxial layers on Si*, Appl. Phys. Lett. **102**, 121908 (2013).

[73] K. Hamaya, M. Kawano, Y. Fujita, S. Oki, and S. Yamada, *Finely Controlled Approaches to Formation of Heusler-Alloy/Semiconductor Heterostructures for Spintronics*, Mater. Trans **57**, 760–766 (2016).

[74] I. Maafa, S. Hajjar-Garreau, R. Jaafar, D. Berling, C. Pirri, A. Mehdaoui, E. Denys, A. Florentin, and G. Garreau, *Room-temperature ferromagnetism of all-epitaxial β-Fe–Ge/diamond–Ge/β-Fe–Ge trilayers*, J. Phys. Condens. Matter **25**, 256007 (2013).

[75] M. Kawano, M. Ikawa, K. Arima, S. Yamada, T. Kanashima, and K. Hamaya, *All-epitaxial Co_2FeSi/Ge/Co_2FeSi trilayers fabricated by Sn-induced low-temperature epitaxy*, J. Appl. Phys **119**, 045302 (2016).

[76] K. Ueda, Y. Ando, M. Kumano, T. Sadoh, Y. Maeda, and M. Miyao, *Formation of Fe_3Si/Ge/Fe_3Si Multi-layer by Double Heteroepitaxy on High Quality Fe_3Si/Ge Substrate for Spintronic Application*, ECS Transactions **11**, 487–491 (2007).

[77] B. Jenichen, J. Herfort, U. Jahn, A. Trampert, and H. Riechert, *Epitaxial Fe_3Si/Ge/Fe_3Si thin film multilayers grown on GaAs(001)*, Thin Solid Films **556**, 120 (2014).

[78] I. Harald and H. Lüth, editors, *Solid-State Physics: An Introduction to Principles of Materials Science*, Springer-Verlag Berlin Heidelberg, 4$^{\text{th}}$ edition (2009).

[79] K. Lenz, E. Kosubek, K. Baberschke, H. Wende, J. Herfort, H.-P. Schönherr, and K. H. Ploog, *Magnetic properties of* $Fe_3Si/GaAs(001)$ *hybrid structures*, Phys. Rev. B **72**, 144411 (2005).

[80] S. Blundell, *Magnetism in Condensed Matter*, Oxford University Press (2001).

[81] R. L. Puurunen, *A Short History of Atomic Layer Deposition: Tuomo Suntola's Atomic Layer Epitaxy*, Chem. Vap. Depos. **20**, 332–344 (2014).

[82] S. Noor, *Structural and magnetic properties of ultrathin Fe_3Si layers epitaxially grown on GaAs(001) and GaAs(110)*, PhD thesis, Ruhr-Universität Bochum (2013).

[83] W. H. Bragg and W. L. Bragg, *The Reflexion of X-rays by Crystals*, Proc. R. Soc. Lond. A **88**, 428 (1913).

[84] H. Fitouri, M. M. Habchi, and A. Rebey, High-Resolution X-Ray Diffraction of III-V Semiconductor Thin Films, In A. E. Ares, editor, *X-ray Scattering*, chapter 7, IntechOpen, Rijeka (2017).

[85] *Magnetic Property Measurement System Hardware Reference Manual*, Quantum Design (1996).

[86] L. Van der Pauw, *A method of measuring specific resistivity and Hall effect of discs of arbitrary shape*, Philips Research Reports **13**, 1–9 (1958).

[87] S. Kasap, Hall Effect in Semiconductors, Accessed: 02-03-2020.

[88] R. Karplus and J. M. Luttinger, *Hall Effect in Ferromagnetics*, Phys. Rev. **95**, 1154–1160 (1954).

[89] N. Nagaosa, J. Sinova, S. Onoda, A. H. MacDonald, and N. P. Ong, *Anomalous Hall effect*, Rev. Mod. Phys. **82**, 1539–1592 (2010).

[90] K. Okamoto, *A new method for analysis of magnetic anisotropy in films using the spontaneous hall effect*, J. Magn. **35**, 353 – 355 (1983).

[91] S. Gaucher, B. Jenichen, J. Kalt, U. Jahn, A. Trampert, and J. Herfort, *Growth of Fe_3Si/Ge/Fe_3Si trilayers on GaAs(001) using solid-phase epitaxy*, Appl. Phys. Lett. **110**, 102103 (2017).

[92] S. Gaucher, B. Jenichen, and J. Herfort, *Ferromagnet/semiconductor/ferromagnet hybrid trilayers grown using solid-phase epitaxy*, Semicond. Sci. Technol. **33**, 104005 (2018).

[93] E. Luna, R. Hey, and A. Trampert, *Interface properties of (In,Ga)As/GaAs quantum wells grown by solid-phase epitaxy*, J. Vac. Sci. Technol. B **30**, 02B108 (2012).

[94] R. Hey, P. Santos, E. Luna, T. Flissikowski, and U. Jahn, *Crystallization of amorphous InAs/GaAs films on GaAs*, J. Cryst. Growth **323**, 5–8 (2011).

[95] J. McNatt, R. Raffaelle, A. Pal, D. Forbes, and W. Maurer, *Recrystallization of Ge for III-V photovoltaic substrates*, In *2009 34th IEEE Photovoltaic Specialists Conference (PVSC)*, pages 000214–000218 (2009).

[96] M. Posselt and A. Gabriel, *Atomistic simulation of amorphous germanium and its solid phase epitaxial recrystallization*, Phys. Rev. B **80**, 045202 (2009).

[97] A. Claverie, S. Koffel, N. Cherkashin, G. Benassayag, and P. Scheiblin, *Amorphization, recrystallization and end of range defects in germanium*, Thin Solid Films **512**, 2307–2313 (2010).

[98] M. Radek, H. Bracht, B. C. Johnson, J. C. McCallum, M. Posselt, and B. Liedke, *Atomic transport during solid-phase epitaxial recrystallization of amorphous germanium*, Appl. Phys. Lett. **107**, 082112 (2015).

[99] J. Kalt, *Wachstum und Charakterisierung epitaktischer Germanium/Fe_3Si-Hetero-strukturen auf GaAs(001)-Subtraten*, Master's thesis, Humboldt-Universität zu Berlin (2015).

[100] B. Jenichen, M. Hanke, S. Gaucher, A. Trampert, J. Herfort, H. Kirmse, B. Haas, E. Willinger, X. Huang, and S. C. Erwin, *Ordered structure of $FeGe_2$ formed during solid-phase epitaxy*, Phys. Rev. Materials **2**, 051402 (2018).

[101] S. H. Liou, S. S. Malhotra, J. X. Shen, M. Hong, J. Kwo, H. S. Chen, and J. P. Mannaerts, *Magnetic properties of epitaxial single crystal ultrathin Fe_3Si films on GaAs (001)*, J. Appl. Phys. **73**, 6766–6768 (1993).

[102] D. Czubak, S. Gaucher, J. Herfort, K. Zollner, J. Fabian, and M. Ramsteiner, *Electronic and magnetic properties of α-$FeGe_2$ films embedded in vertical spin valve devices* (2020), preprint.

[103] C. Kloc, E. Arushanov, M. Wendl, H. Hohl, U. Malang, and E. Bucher, *Preparation and properties of FeSi, α-$FeSi_2$ and β-$FeSi_2$ single crystals*, J. Alloy Compd **219**, 93 – 96 (1995), Eleventh international conference on solid compounds of transition elements.

[104] G. Cao, D. J. Singh, X.-G. Zhang, G. Samolyuk, L. Qiao, C. Parish, K. Jin, Y. Zhang, H. Guo, S. Tang, W. Wang, J. Yi, C. Cantoni, W. Siemons, E. A. Payzant, M. Biegalski, T. Z. Ward, D. Mandrus, G. M. Stocks, and Z. Gai, *Ferromagnetism and Nonmetallic Transport of Thin-Film $\alpha-FeSi_2$: A Stabilized Metastable Material*, Phys. Rev. Lett. **114**, 147202 (2015).

[105] N. S. Murthy, R. Begum, C. Somanathan, and M. Murthy, *Magnetic structures in the iron-germanium system*, Solid State Commun. **3**, 113 – 116 (1965).

[106] P. D. Babu, P. K. Mishra, V. Dube, R. Mishra, P. U. Sastry, and G. Ravikumar, *Magnetic structure at low temperatures in $FeGe_2$*, AIP Conference Proceedings **1591**, 1586–1588 (2014).

[107] S. Tang, I. Kravchenko, T. Z. Ward, Q. Zou, J. Yi, C. Ma, M. Chi, G. Cao, A.-P. Li, D. Mandrus, and Z. Gai, *Dimensionality Effects in $FeGe_2$ Nanowires: Enhanced Anisotropic Magnetization and Anomalous Electrical Transport*, Sci. Rep. **7**, 7126 (2017).

[108] S. D. Sarma, E. H. Hwang, and A. Kaminski, *How to make semiconductors ferromagnetic: a first course on spintronics*, Solid State Commun. **127**, 99–107 (2003).

[109] H. Chen, P. Han, X. D. Huang, L. Q. Hu, Y. Shi, and Y. D. Zheng, *Semiconducting Ge-Si-Fe alloy grown on Si(100) substrate by reactive deposition epitaxy*, Appl. Phys. Lett. **69**, 1912–1914 (1996).

[110] S. Dutta, K. Sankaran, K. Moors, G. Pourtois, S. Van Elshocht, J. Bömmels, W. Vandervorst, Z. Tőkei, and C. Adelmann, *Thickness dependence of the resistivity of platinum-group metal thin films*, J. Appl. Phys. **122**, 025107 (2017).

[111] S. Sangiao, L. Morellon, G. Simon, J. M. De Teresa, J. A. Pardo, J. Arbiol, and M. R. Ibarra, *Anomalous Hall effect in Fe (001) epitaxial thin films over a wide range in conductivity*, Phys. Rev. B **79**, 014431 (2009).

[112] S. Tiwari, R. Master, R. J. Choudhary, D. M. Phase, and B. L. Ahuja, *Effect of oxygen partial pressure and Fe doping on growth and properties of metallic and insulating molybdenum oxide thin films*, J. Appl. Phys. **111**, 083905 (2012).

[113] S. Datta, *Electronic transport in mesoscopic systems*, Cambridge ; New York : Cambridge University Press, 1st paperback edition (1995).

[114] S. Parasuraman, *Lecture notes: Electronic Materials, Devices, and Fabrication*, Department of Metallurgical and Materials Engineering, IIT Madras (2014).

[115] E. Simoen, K. Opsomer, C. Claeys, K. Maex, C. Detavernier, R. L. Van Meirhaeghe, and P. Clauws, *Study of metal-related deep-level defects in germanide Schottky barriers on n-type germanium*, J. Appl. Phys. **104**, 023705 (2008).

[116] D. Leadley, *Semiconductors | Electrical Characterisation | Determining the Energy Gap* (2010), online.

[117] B. van Zeghbroeck, *Principles of Semiconductor Devices* (2006), online.

[118] N. W. Ashcroft and N. D. Mermin, *Solid State Physics*, Harcourt College Publishers (1976).

List of Figures

Acknowledgements

This thesis would not have been possible without the collaboration of a number of scientists with whom I have worked directly and indirectly. The guidance and support I have received throughout the past few years has been enormous. Along this project, I have learned and progressed both as a researcher and a person. For that, I am grateful to all those who were involved in my life at the institute, both in the office and in the lab, and contributed to improve my skills, while providing an exceptionally stimulating working environment. I will carry those experiences along the following steps of my career.

First and foremost, I wish to thank my academic supervisor, Prof. Dr. Henning Riechert, for giving me the opportunity to work at the Paul-Drude-Institut. His leadership and charisma never failed to trigger excitement for scientific research, and the guidance he provided has been valuable from day one until the end. Corresponding recognition goes to Dr. Lutz Geelhaar, for his attentive supervision of my work as part of the Epitaxy department, helpful career discussions and encouragement. I then wish to thank immensely my scientific supervisor, Dr. Jens Herfort. His expertise, just advice, motivation, and understanding, were incredibly precious in all aspects of my work. He has helped me go through each and every challenge, from the technical details of the MBE system to the quirks of the SQUID magnetometer, the interpretation of my results, while reviewing all written and oral scientific communications I have produced over the last four years. I have been given enough freedom to explore new avenues, while always being supportively guided.

I express sincere gratitude to the collaborators who have enriched this thesis with their work. I wish to thank Dr. Bernd Jenichen, for the innumerable hours spent preparing and imaging TEM specimens, and the work he has done to clarify key aspects of the samples I have grown; Dr. Manfred Ramsteiner, for providing guidance regarding spintronics and electrical measurements of the devices; Dr. Achim Trampert and Dr. Uwe Jahn for their contribution to our publications. I extend significant appreciation to fellow students Jochen Kalt, for his seminal work on the solid-phase epitaxy approach; Dietmar Czubak, for his help with the spin valve measurements; and Lars Oppermann, for his contribution to the investigation of the magnetic properties of the samples.

My day-to-day work in the labs could not have proceeded without the help of several technicians, who truly know everything there is to know about the MBE systems and various experimental apparatus available at the institute. Thank you especially Hans-Peter Schönherr and Claudia Hermann. Without you, I could not have spent as much time focusing on the scientific details of my research. I also wish to thank Walid Anders and Angela Riedel for

the nanostructures patterned, etched, cut and bonded using my samples, which played an essential role in the development of this thesis.

Last, but not the least, I thank my family and friends. Catherina, for the patience and all-round support. The new friends I have made in Berlin, who were always at least a bit interested in hearing the latest outcome of my scientific work. The old friends I have left in Canada, who accepted to see me go abroad to pursue my studies. My parents and sisters, who gave me courage and never failed to remind me that no matter where I am, there is always be a place for me to return 'home'.

Declaration of independent work

I declare that I have completed the thesis independently using only the aids and tools specified. I have not applied for a doctor's degree in the doctoral subject elsewhere and do not hold a corresponding doctor's degree. I have taken due note of the Faculty of Mathematics and Natural Sciences PhD Regulations, published in the Official Gazette of Humboldt-Universität zu Berlin no. 42/2018 on 11/07/2018.

Berlin, 12.10.2020